Analysis of impervious surfaces and surface temperature over Tshwane metropolitan using in-situ and remotely sensed data

Adeyemi Adeniyi Adedayo (13387546)

A dissertation submitted in partial fulfilment of the requirement for the degree of

Masters of Science in Geoinformatics

MSc. Dissertation

Department of Geography, Geoinformatics and Meteorology

University of Pretoria

January 2015

Declaration of originality

This is to certify that the work is entirely my own and not of any other person, unless explicitly acknowledged (including citation of published sources). The work has not previously been submitted in form to the University of Pretoria or to any other institution for assessment or for any other purpose.

Signed: _____

Date: _____

Dissertation Supervisors

Main supervisor:

- Dr. Joel Ondego Botai, Department of Geography, Geo informatics and Meteorology, University of Pretoria

Co-supervisor:

- Dr. Abel Ramoelo, Council for Scientific and Industrial Research (CSIR), Natural Resources and the Environment (NRE), Pretoria, South Africa; also at University of Limpopo, Risk and Vulnerability Assessment Centre (RVAC), Sovenga, South Africa.

Acknowledgements

I would like to express my indebtedness to GOD ALMIGHTY who was by my side through the years, months, days and nights; to my Lord JESUS CHRIST, for his mercy and kindness and to the HOLY SPIRIT, my source of inspiration. My deep and sincere appreciation goes to my parents Mr. and Mrs. A.O Adeyemi and my siblings Adebola and Adenike for their constant prayers and support to see this program come to a success.

Special thanks to the Applied Centre for Climate and Earth System Science (ACCESS) for their support with the research funding needed for the execution of the study. This research was implemented at the Department of Geography, Geoinformatics and Meteorology, University of Pretoria, and Council for Scientific and Industrial Research (CSIR), South Africa.

I am very grateful to Dr. Joel Botai and Dr. Abel Ramoelo for their incredible support, encouragement and advice all the way throughout this research work. It is with a deep sense of appreciation that I acknowledge the helpful cooperation and kind assistance of Oupa Malahlela, Adeola Abiodun, Philemon Tsela, Lisa Nyadzua, Ingrid Boyesen, Precious Mahlangu and Samy Kabangu towards the successful implementation and completion of the project. May the Almighty God continue to be with them all.

Finally, I also wish to recognize the support and affections of Opeyemi Esther Ojo whom has been there for me throughout my stay in South Africa.

Abstract

Tshwane is one of the major metropolitan in Gauteng Province. This metropolitan continues to experience rapid urbanization as a result of population growth, leading to the conversion of natural lands into impervious surface area (ISA) i.e., constructed surfaces – sidewalks, roads rooftops, parkinglots covered by impenetrable materials such as asphalt, concrete and stones which prevent water from infiltrating into the soil. Such landscapes influence the climate of the Metropolitan as evidenced by the recent heat wave characterized by high temperature. Therefore, the consistent information about these changes will play an important role in city planning and environmental management. In this study, seven land use/cover types were delineated from the cloud free Landsat images using maximum likelihood (ML) and random forest (RF) classifiers to map the Tshwane metropolis. The overall accuracies for classifying the seven land cover types were 88.63% and 80.13% (Landsat 7 ETM+, 2003) and 88.82% and 82.03% (Landsat 8 LCDM) for both ML and RF, respectively. In addition, based on the pairwise comparison of error matrix the two algorithms were found to produce approximately identical classification errors. Furthermore, the remote sensing data was also used to assess the relationship between LULC changes and LST estimation. Mean near surface temperature from the weather stations was used as a point of reference to verify the accuracy of the final retrieved LST images. From Landsat 7 ETM+ (2003), the mean pixel temperature for Pretoria Eendracht and Irene Wo weather station when compared the mean near surface temperature produced a LST retrieval error of 3.3^{O}C and 1^{O}C respectively. Similarly, Landsat 8 LCDM data (2013) mean pixel temperature for Pretoria UNISA weather station and Pretoria National Botanical Institute when compared the mean near surface temperature produced a LST retrieval error of 0.38^{O}C and 1.3^{O}C for the two stations. Finally, the remote sensing data showed the quantitative effect of impervious surface area changes on mean LSTs, through the distribution of urban heat island within Tshwane metropolitan.

Keywords: Land use or cover (LULC),

Land surface temperature(LST),

Impervious surface area (ISA),

Tshwane Metropolitan

List of Acronyms

ASD	:	Analytical Spectrometry Device.
ASTER	:	Advance Space borne Thermal Emission And Reflection Radiometer.
CART	:	Classification and Regression Tree.
CBD	:	Central Business District.
DMSP	:	Defence Meteorological Satellite Program.
ETM+	:	Enhanced Thematic Mapper Plus.
FASC	:	Full Aperture Solar Calibration.
GCP	:	Ground Control Point.
GIS	:	Geographical Information System.
GOES	:	Geodynamic Experimental Ocean Satellite.
GTI	:	Geoterraimage.
GPS	:	Global Positioning System.
ISA	:	Impervious Surface Area.
ISAT	:	Impervious Surface Analysis Tool.
IPCC	:	International Panel on Climate Change.
LDCM	:	Landsat Data Continuity Mission.
LIDAR	:	Light Detection and Ranging.
LSMA	:	Linear Spectral Mixture Analysis.
LST	:	Land Surface Temperature.
LULC	:	Land use / land cover.
MODIS	:	Moderate Resolution Imaging Spectroradiometer.

MIR	:	Middle Infrared.
MESMA	:	Multiple End Member Spectral Mixture Analysis.
ML	:	Maximum Likelihood.
NSMA	:	Normalized Spectral Mixture Analysis.
NASA	:	National Aeronautic and Space Administration.
NRCS	:	Natural Resource Conservation Services.
NIR	:	Near Infrared.
NOAA	:	National Oceanic And Atmospheric Administration.
NDVI	:	Normalized Difference Vegetation Index.
OLS	:	Operation Line Scan Imaging System.
OLI	:	Operation Land Imager.
OOB	:	Out of Bag.
PA	:	Producer Advanced.
PASO	:	Partial Aperture Solar Calibrator.
PNMESMA	:	Pre-screen And Normalized Multiple End Member Spectral Mixture.
QUAC	:	Quick Atmosphere Correction.
RADAR	:	Radio Detecting And Ranging.
RF	:	Random Forest.
RMSE	:	Root Mean Square Error.
ROI	:	Region of Interest.
SAWS	:	South African Weather Station.
SEVIRI	:	Spinning Enhanced Visible And Infrared Imager.

SWIR	:	Shortwave Infrared Red.
SONAR	:	Sound Navigation And Ranging.
SPOT	:	Satellite Pro batoire d‘Observation de la Tarre.
TIR	:	Thermal Infrared.
TM	:	Thematic Mapper.
TNDVI	:	Transformed Normalized Difference Vegetation Index.
TOA	:	Top of Atmosphere.
UA	:	User Accuracy.
UHI	:	Urban Heat Island.
USGS	:	United States Geological Survey.
UTM	:	Universal Transverse Mercator.
VIS	:	Visible Bands.

TABLE OF CONTENTS

LIST OF FIGURES

LIST OF TABLES

1 CHAPTER ONE: INTRODUCTION

1.1 General introduction

Globally, there has been an unprecedented increase in population concentration in cities which have led to rapid urban landscape changes. Recent studies have demonstrated that 50% of the global population lives in urban areas (Herold et al., 2003). As proposed by Montgomery and Hewett (2005) the highest rate of urbanization and associated land use or cover changes have been observed in the developing countries. Likewise a recent projection by the United Nations as reported by Civco et al. (2005) shows that the urban population of the developing nations is now growing at the annual rate of 2.3% and is predicted to double in 30 years, i.e., a rise from 1.94 billion in the year 2000 to 3.88 billion in 2030. Based on these predictions, it implies that cities in the developing countries will have to double their built up or impervious surface areas (ISA) to accommodate the increasing present population.

Changes in land use or cover of the earth's surface emphasis on biophysical processes that result in global environmental change (Turner, 2006). Lambin and Geist (2008) defined land cover as an attribute of the earth's land surface and the immediate subsurface (e.g. soil, topography, surface and ground water and built up), on the other hand, land use is the purpose for which land is used. Cassman et al. (2005) pointed out that land cover change is as a result of human activities that directly manipulates the earth's surface for individual or societal need (e.g., agricultural, built-up, etc.). For instance, Ferreira et al. (1999) reported that South Africa's population grows with constant land use changes in urban areas (such as Pretoria, Johannesburg, Cape Town etc). Some of these land use practices, for instance, in the rural areas can be seen as static i.e., changes in land cover character without changes in overall classification (Lambin et al., 2003). However, urban settlement where structures, population density and activity pattern are constantly changing, there is constant land cover conversion i.e., replacement of one cover type by another (Lambin and Geist, 2008). As with many developing countries, South Africa has experienced rapid development – urbanization and industrialization, which have given rise 'to increase in impervious surface cover in major cities. Impervious surfaces are man-made features or surfaces that cannot allow the permeation of water from land surfaces into the underlying soil (Okeke, 2006). ISA are mainly associated with human activities such as constructed transportation infrastructure like

roads, sidewalk and parking lots all covered by impenetrable materials such as asphalt, concrete, brick and stones and building like rooftops (Slonecker et al., 2001). Arnold and Gibbons (1996) earlier reported that ISA could be seen as an indicator of the degree of urbanization and environmental quality. Understanding changes in ISAs is important for a wide range of environmental applications such as watershed impact assessment (Jennings and Jarnagin, 2000), rainfall run-off volume, duration and intensity (Lohani et al., 2002), ground water recharge and base flowstorm analysis, stormflow and flood frequency (Brun and Band, 2000), urban land use or cover classification (Lu and Weng, 2006, Phinn et al., 2002) urban planning (Brabec et al., 2002). Therefore, timely and accurate mapping of the impervious surface distribution is of importance to a range of issues and themes associated to global environmental change.

In spite of the significance of ISAs studies, the methods for estimating, mapping and applications of ISA data have not been sufficiently explored in Africa. Ground measurement and remote sensing data have been techniques applied in characterizing and quantifying impervious surface area (Weng, 2012). Previously, field survey with global positioning system (GPS) have been used to provide reliable information on ISA but have also been seen to be time consuming and expensive. Manual digitizing from hard copy maps or aerial photographs were the earliest approaches for mapping impervious surface area. For example in North Africa, Noin (1970) determined the housing units in the rural areas by deriving rural population estimates of Morocco using aerial photographs and then applied household-size multiplier to dwellings to estimate the population.

Slonecker et al. (2001) revealed that in the 1970's and 1980's, the use of remote sensing data started gaining recognition both in environmental and natural resources studies. It was used in the interpretive, spectral and modelling applications on impervious surfaces. Four different previous approaches were also acknowledged by Brabec et al. (2002) which were:

- Using planimeter to measure ISA on aerial photographs.
- Counting the number of intersections on the overlain grid on aerial photographs.
- Conducting image classification.
- Estimating coverage through the percentage of urbanization.

Weng (2012), reported that remote sensing of ISAs gained more interest in the remote sensing community with the invention of high resolution images and more sophisticated software and capable techniques in recent years. These remote sensing data have been widely used to analyse ISAs because of their advantage in converting a large geographical area and temporal frequency. These different types of satellite sensor data that has been used to map ISA both in the past and current study are categorized into two based on spatial resolution, namely: moderate or medium spatial resolution Landsat TM/ETM+, SPOT and ASTER imagery (Zha et al., 2003) and higher spatial resolution IKONOS and Quick Bird images (Lu and Weng, 2009).

During the past few decades, commonly used modelling techniques for impervious surface detection includes multivariate regression (Bauer et al., 2005), spectral mixture analysis (De Voorde et al., 2007), contextual classification (Yuan et al., 2005), object based analysis (Jacquin et al., 2008) and machine learning based methods e.g. decision tree and neutral networks (Hu and Weng, 2009). Lee and Lathrop (2006) identified that many of these previous studies extracted impervious surfaces at the pixel level and percentage imperviousness at the sub-pixel level. Some of the few works in Africa that examined impervious surface areas at pixel level include;

a) Okeke (2006) mapped impervious surface changes in watersheds in the south eastern region of Nigeria using Landsat imagery. He computed percentage imperviousness using the impervious surface analysis tool (ISAT) which is an extension of Arcview 3.3 developed by the National Oceanic and atmospheric Administration (NOAA) Coastal Service Center and the university of Connecticut non-point Education for Municipal official (Nemo) Program.

b) Mertens and Lambin (2000) previously carried out land cover change trajectories (Urban sprawl) in the southern Cameroon making use of Landsat MSS, SPOT XS, and topographical maps (for geometrical registration and further resampling the spatial resolution of the two Landsat images using nearest neighbor technique) spanning two decades for validation and projection of future deforestation.

c) Weng (2007) also summarized other research related to the delineation of impervious cover and these studies highlighted what has been accomplishments and limitations in achieving accurate imperviousness estimation from remote sensing imagery.

Subsequently, the conversion of natural land to impervious surfaces has been reported by various studies as the main contributor to climate change and variability in different parts of the world (Brunsell, 2006). Zhang et al. (2009) also pointed out that urbanization and industrialization can result in alteration of the land surface and near surface atmospheric conditions which in turn could cause changes in the thermal properties of urban areas, making them more warmer than the surrounding rural areas (i.e. Urban heat island).

d) Dousset and Gourmelon (2003) explained that urban heat island phenomenon is mainly caused by replacement of vegetated areas by impervious materials which influence the radiative fluxes near surface flow leading to higher levels of sensible heat fluxes in urban areas. Weng (2009) showed that urban surface physical properties such as colour, sky view factor, street geometry, traffic loads and various other anthropogenic activities are important factors that determine land surface temperature (LST) in urban areas.

Many researchers have also correlated the land surface temperature of urban surfaces to land use or cover characteristics (Weng, 2009). In West Africa, Nigeria, Ifatimehin et al. (2009) evaluated the effect of land use or cover change in the surface temperature of Lokoja town. Previously, urban heat island phenomenon and physical processes have been monitored traditionally by conducting ground based observations from fixed thermometers at weather stations or by traversing an area with a thermometer attached to a vehicle (Voogt and Oke, 2003). Weng (2009) also reported that the study of urban surface temperature has been carried out using numerical and physical models such as an energy balance model (Oke et al., 1999), three-dimensional simulation (Saitoh et al., 1996), Gaussian models (Streutker, 2003) and laboratory models (Cendese and Monti, 2003). Bottyán and Unger (2003) revealed that among these models, statistical analysis has been the most used in associating surface characteristics to land surface temperature at geographical scale.

Reviews by various authors has linked land surface temperature to biophysical and meteorological factors, for example, urban and street geometry, built-up or impervious surface area and height, vegetation, population distribution, intensity of human activities and land use or cover change (Xiao et al., 2008). Weng (2009) stated that a comprehensive literature describing the relationship between land surface temperature and various vegetation indices have been documented. For example, in the southwest Cape of South Africa, Sandham and Zietsman (1997) carried out surface temperature measurement using Landsat

TM and Transformed Normalized difference Vegetation index (TNDVI) data to map summer surface temperature measurement. Most recently, in Nigeria, West Africa, Ifatimehin and Adeyemi (2008) also used normalized difference vegetation index (NDVI) when retrieving land surface temperature using Landsat TM images.

Overall, remote sensing data, especially thermal bands are seen as a unique source of information for defining surface heat island (Weng, 2009). In-situ data from meteorological stations, though, has a high temporal resolution and offers long term coverage but lacks spatial information. Remote sensing data on the other hand, through previous researches proved to be effective in providing continuous and simultaneous views of the large study area (ranging from municipal to provincial level) and detailed investigation of urban surface. Rao (1972) was the first to demonstrate that urban areas could be identified from the analysis of thermal infrared remote sensing data. Since then, Jensen (2007) revealed that there has been a wide range of thermal infrared sensors have been used to study land surface temperature and urban heat island as a result of the improvement in data over the years.

Streutker (2003) carried out studies for regional- scale urban temperature mapping using land surface temperature derived from NOAA-AVHRR data. Similarly, Pinheiro (2006) developed a daily long term record of NOAA-14 AVHRR land surface temperature over Africa. Several researchers around the world in recent years have also used both the Landsat TM and ETM+ on land surface temperature and urban heat island studies (Jeong, 2012). Additionally, the use of high resolution thermal infrared remote sensing and geographical information system by Lo et al. (1997) has been used to assess the urban heat island effect. Eventhough, there has been an increase in the availability of thermal remote sensing data (Table 1.1), studies on land surface temperature using thermal bands have been have been carried out more in the developed countries than in developing nations (e.g. South Africa).

Oke (1982) described that each component in the urban landscape (e.g. parking lot, building garden etc.) exhibits a unique radioactive, thermal, moisture and aerodynamic properties.

Table 1.1: Examples of thermal infrared sensor systems (adapted from Jensen (2007)).

Sensor	**Spatial resolution**	**Thermal band spectral resolution**
Television IR Operational (TIROS)	600 x 600m	10.5 - 12.6 µm
NOAA Geostationary Operational environmental Satellite (GOES)	8 x 8km	6.47 – 7.02 µm
NOAA Advanced Very High Resolution Radiomater (AVHRR)	1.1 x 1.1km	3.55 – 12.50 µm
Landsat Thematic Mapper 4&5	120 x 120m	10.4 – 12.5 µm
Landsat 7 Enhanced Thematic Mapper Plus	60 x 60m	10.4 – 12.5 µm
Landsat 8 Landsat Data Continuity Mission	100 x100m	10.6 – 11.19 µm 11.5 – 12.51 µm
Advanced Spaceborne Thermal Emission and Reflection Radiometer (ASTER)	90 x 90m	8.125 – 11.65 µm

However, the thermal response of individual land cover within a city is very useful in understanding as radiative transfer over an urban landscape due to diversity of land cover types and their physical properties (Renee et al., 2006). Finally, with increasing concern regarding global change, it will be of great importance to quantify ISA changes and analyse its relationship with surface temperature variability across Tshwane metropolitan.

1.2 Problem statement

Urban sprawl continues to increase based on the fact that urban population continues to surpass the rural population (Weng, 2009). According to the UN (2008) more than 50% of the world's population now lives in urban areas and this number will continue to rise, particularly in developing or third world countries (e.g. Africa). Binns et al. (2003) reported that the average annual urban growth rate within the sub-Saharan Africa was 4.8% between 1980 and 1993. This urban growth has now led to the introduction of megacities (>8million) around the globe (Bobrinskaya, 2012). Although 3% of the earth is occupied by urban areas, the impact of these anthropogenic activities on the natural environment has reached the

global concern (Griffiths et al., 2010). For example, land use or cover changes effect on various environmental processes (i.e., locally and regionally). These changes in land use or cover have also resulted in alterations in the radiative, thermal, moisture, roughness and emission properties of the earth's surface and the atmosphere above (Kalnay and Cai, 2003, Streutker, 2003).

Furthermore, urban sprawl which has been observed as a sign of growth and prosperity, has continuously brought about compacted infrastructure and expansion (i.e., industrialization and emergence of more residential areas that makes an impervious surface or built-up areas ideal for use). These changes have brought about series of adverse impact on the environment (ecological and hydrological disturbance) e.g., impact on watershed areas, water cycle, and water quality, erosion of construction sites, non-point source pollution, flooding, stream health, reduction in ground water and wetlands, urban heat island and reduced sequestration of carbon from atmosphere (Lu and Weng, 2006, Yuan and Bauer, 2007).

In recent years, Gauteng province has experienced tremendous increase both in population and land use or cover changes. This urban sprawl has resulted in temperature variation across the major municipalities within the province. Although several studies have been conducted demonstrating the impact of ISA chnages due to urbanization on land surface temperature using remote sensing data in different cities across the globe (e.g., Asia and America), few of these studies have been done in Africa in spite of the availability of satellite imagery. This has been proved by a recent search for online scientific papers using various search engines like Google and Journal citations which showed that limited studies focused on cities in Africa.

Although, the cost effectiveness of this research (i.e. land use or cover changes effect on surface temperature variability) has been a great challenge throughout the scientific world, filling the gap (performing this study in Africa) will be of an important contribution to the urban society and the world of science and technology. This study will further provide important impervious surface area changes information which will allow the dependable projection of future surface temperature modifications and support decision makers with information that will help in various sectors such as energy management, urban planning and environmental sustainability.

In this study, we will examine how the spatial and temporal pattern of impervious surface areas have affected urban land surface temperature across Tshwane metropolitan, Gauteng Province, South Africa using remote sensing data and other in-situ measurements.

1.3 Research aims and objectives

1.3.1 Aims

The main aim of this study is to investigate the relationship of impervious surface area (urban land use, land cover) changes and land surface temperature using Landsat ETM+ and Landsat 8 LDCM and other ancillary data (e.g.,temperature data from weather stations) obtained from Tshwane metropolitan, Gauteng Province, South Africa.

1.3.2 Objectives

- To detect LULC types within the Tshwane metropolitan using ML and RF classifier.
- To examine the change pattern of the LULC categories between 2003 and 2013.
- To derive LST from Landsat thermal images.
- To analyse the effect ISA changes on land surface temperature across Tshwane metropolitan, South Africa.

1.4 Research hypothesis

- Changes in impervious surface areas have decreased natural vegetated land cover types between 2003 and 2013 within Tshwane metropolitan.
- Surface temperature changes may be related to changes in impervious surface areas.

2 CHAPTER TWO: LITERATURE REVIEW

2.1 The urban microclimate

According to IPCC (2001), climate is defined as the regular weather or the description of temperature, precipitation, and wind, over a period of time. Several levels of regional climates which are macroclimate and microclimate have also been desccribed. Macroclimate refers to the climate of broad area which ranges from tens to hundreds of kilometres and on a smaller scale its associated with mesoclimate (climate of a set of tens or hundreds of meters). Microclimate refers to a limited atmospheric zone where the climate varies from the surrounding area or climate of a specific environment in a small restricted space). Microclimate is also subdivided into different classes as reported by Geiger (1951);

- Urban microclimate which is affected by concrete or impervious surface areas, buildings, air pollution, compact inhabitation and so on.
- Vegetation microclimate which focus on the complex nature of the air space occupied by vegetation and its effects upon the vegetation.
- Microclimate of small spaces of houses, greenhouses, caves etc.

Urban heat island is also one of the resultant effects of these urban climate changes. It is defined as the phenomenon where an urban or metropolitan area is significantly warmer than its surrounding rural areas (Streutker, 2003). Oke and Emery (1989) previously asserted that urban climate can also be influenced by urban forests and anthropogenic surfaces (e.g. impervious surfaces) which creates a spatial unevenness in local heat transfer flux known as urban microclimate. The urban heat island which is also known as mesoclimate climate at the urban boundary layer are created as a result of the accumulation of microclimate on urban canopy layer (Schmid and Oke, 1990). Due to this reason, it is very important to investigate the main factors associated with the formation of heat island and the interaction between these factors (Shahmohamadi et al., 2010).

Urbanization can be greatly influenced by climatic parameters (i.e., temperature, precipitation, humidity, wind, sunlight) and the design of a city in terms of its general structure, orientation, building forms, materials, can be greatly influenced by climate (Shahmohamadi et al., 2010). For instance, cities in hot arid areas have buildings that are

dense and compact in order to avoid penetration of sunlight. According to Bridgman et al. (1995), urban centers with higher density of built-up or impervious surface materials, have more influence on climate. Some of these impacts are;

- The replacement of soil and vegetation by impervious surfaces such as concrete, glass and asphalt.
- Emission of artificial heat from buildings, air conditioners, industry and automobiles.
- Substituting the rounded, soft shapes of trees and bushes with blocky, angular buildings and towers; thereby changing the radiative fluxes e.g., glass buildings and windows reflect large amounts of solar radiation into the surrounding air.
- Efficiently disposing of precipitation in drains, sewers and gutters, preventing surface infiltration.
- Emitting contaminants from a wide range of sources, which, with resultant chemical reactions, can create an unpleasant urban atmosphere.

Similarly, the increased pollutant sources, both stationary (industry) and non-stationary (vehicles) due to urbanization result in worsening atmospheric conditions (Roth, 2002). Furthermore, solar radiation is seriously shortened because of increased scattering and absorption. In particular, many cities in the tropics experience weak winds and limited circulation of air and this contibutes to pollutants accumulation (Roth, 2002). Previous works of (Oke, 1987) pointed out three different types of UHI (Table 2.1) which can be classified as:

Table 2.1: Types of urban heat island.

Type of UHI	**Description**
Air	Which comprise of urban canopy layer heat island found in the air layer beneath the roof level and urban boundary layer heat island found in the air layer above roof-level.
Surface	This kind of UHI can be distinguished based on the temperatures of urban surfaces.
sub-surface	Found on the ground beneath the surface.

2.2 Factors influencing the formation of urban heat island

According to Givoni (1998) thermal differences between the urban and the rural are affected by meteorological factors such as cloud cover, humidity, and wind speed and types of the urban structure (i.e., the size of cities, the compactness of the built-up areas, and the ratio of building heights to the distances between them). These differences may also influence the magnitude of the urban heat island. Shahmohamadi et al. (2010) pointed out that urban factors that contribute to heat island are generally population size, topography, wind speed, anthropogenic heat, water runoff and vegetation cover. Thus, urban heat island is mainly observed owing to physical factors described in the following;

2.2.1 Meteorological parameters

Meteorological parameters such as temperature, precipitation, humidity, wind and sunlight are associated with an urban heat island increase in cities. For instance, low wind speed leads to insufficient air exchange in street canyons which can decrease ground-level air quality and increase the rate of UHI formation over the city (WHO, 2004).

2.2.2 Urbanization

Urban sprawl and development of various industries has led to a degradation in the quality of urban environment (Shahmohamadi et al., 2010). Asimakopoulos et al. (2001) identified that increased numbers of buildings led to removal of vegetation which affect the urban climate i.e., through increased urban heat island intensity. Table 2.2 below gives a description of how urbanization can directly affect climatic parameters such as temperature, humidity, precipitation, wind and solar radiation.

Table 2.2: Effect of urbanization on climatic parameters (adapted from Emmanuel, 2005).

Climatic parameter	**Effect of urban sprawl**
Temperature	Rise in daily minimum temperature: Some change in maximum temperature.
Precipitation	Large increases in summer (up to 21%) and smaller increases in winter (5-8%). In the tropics, the increase are attributed more to air pollution than heat emission.
Humidity	Reduction in daytime humidity, but increase in night-time values.
Wind	Increases in the number of calm periods observed. Up to 20 percent reduction in wind speeds are known. The effect is greater upon weaker winds.

Shahmohamadi et al. (2010) reported that places with high density of built-up can lead to higher temperature, precipitation, sunlight and decrease in wind speed and humidity which can give rise to the formation of urban heat island over the city. Furthermore, the effect of urban structures on the microclimatology is affected by several influences such as; city locality, city extents and population, density of built-up area, urban geometry, thermal properties of materials, surface waterproofing, anthropogenic heat, air pollution, land use and wind speed. The migration of population from the suburbs to the urban areas are the main cause of rapid growth of cities. This growth are associated with vehicular traffic, intensity of heating in the winter and air conditioning and industrial plants which contributes to the formation of UHIs (Shahmohamadi et al., 2010).

Building density at different areas in a city can affect the local climate in each of the discrete urban areas. For instance, in Tshwane, accelerating urban sprawl has resulted in an increase in the built-up areas which are characterized by marked UHI and high temperature variability. Shahmohamadi et al. (2010) pointed out that buildings alters wind speed, radiant balance and temperature conditions near the ground level. As a result, the portion of land covered by buildings in a given area and distances between buildings along the axis upsetting the solar exposure of the buildings can affect urban climate. According to Emmanuel (2005), geometry of a city is described by a component called the urban canyon. Temperature distribution and air movement within urban canyons are important in various related studies such as; energy consumption of buildings, pollutant dispersion studies, heat and mass exchange between the buildings and the canyon air (Asimakopoulos et al., 2001). Emmanuel (2005) described the urban canyon as the three-dimensional space bounded by a street and the buildings that border the street. Urban canyons limit the view of the sky dome (characterized by the sky view factor SVF), cause multiple reflection of solar radiation and limit the free air movement (Shahmohamadi et al., 2010). The sky view factors (SFV), according to Oke (1981) is a geometrical theory that describes the fraction of the overlying hemisphere occupied by the sky. As the view of the sky is critical for long-wave radiation (as well as short-wave energy gain), it goes without saying that SVF is important in understanding increase in UHI intensity. For example, Tshwane metropolis, has complex urban geometry, particularly in Pretoria Central which increases friction created by a rough urban surface.

Oke (1982) and Quattrochi et al. (2004) pointed out that materials such as stone, concrete, and asphalt tend to trap heat at the surface. These impervious surface materials absorb and

hold solar radiation and heat which are released slowly at night. The albedo of a surface is responsible for the amount of solar radiation it absorbs. Taha (1997) identified that high albedo building surfaces (white surfaces) have been proven to cool down urban temperatures. In the Tshwane metropolis, most of urban materials are concrete and asphalt with low albedo and non-reflective surfaces which absorb solar energy which contibutes to formation of UHI. The creation of evaporation deficiency due to the absence of materials that are porous in urban surface, a high percentage of non-reflective, water-resistant surfaces and a low percentage of vegetated and moisture trapping surface within the city causes increase in the intensity of urban heat island. Vegetation, especially in the presence of high moisture levels, is very important in the control of surface temperatures according to earlier work of Goward et al. (1985). Within Tshwane metropolis, newly constructed buildings has lead to the removal of vegetation resulting to reduced evapotraspiration and increased temperature.

Taha (1997) pointed out that the heat from anthropogenic activities that goes into urban atmosphere contributes to the intensity of the UHI effect. Urban hubs tend to have higher energy demands than surrounding rural areas as a result of their high population density (Shahmohamadi et al., 2010). Nevertheless, Landsberg (1981) previously indicated that the heat island effect lessens the need for heating in the winter and this is compensated by the increased demand for air-conditioning during the summer months. The pollution created by emissions from air conditioning and power generation increases absorption of radiation in the boundary layer (Oke, 1982). For example the Tshwane metropolis has increased in number of buildings due to population increase, these have caused all the energy consumed by air conditioning to be released to the environment, thereby increasing the urban temperature.

Recent trends in the loss of prime agricultural land to urban area is as a result of many cities emerging near major agricultural or farmland areas. Although, this land use or cover change is not pronounced yet on a global scale, but very evident at local level in many countries. For example, Seto et al. (2002) pointed out that China has lost nearly 1million ha of its cultivated land both in the rural and urban areas to expansion of infrastructure between 1988-1995. For developing countries including Africa, rough estimate indicates that 1 to 3 million ha of cropland may have been replaced by paved areas every year to meet the land demands for urban sprawl (Döös and Shaw, 1999). Due to this reason, this research focus impervious surface area changes and impact on the climate of Tshwane metropolis which will further provide important information on projections of future changes. This information will also

support decision makers with information that could facilitate energy management, urban planning and environmental sustainability.

2.3 Change detection

According to Singh (1989) can be defined as the process of identifying difference in the state of an object or phenomenon by observing it at different epochs. These changes detected on earth surface gives a better understanding of the impacts of the relationship between man-made and natural activities which could provide basis for resource management (Lu et al., 2011). According to Coppin et al. (2004) and Lunetta et al. (2006), land cover changes can be distinguished into two types, namely land conversion (conversion from one land cover class into another due to human activities such as deforestation or urban sprawl), and land cover modification (shows landscape adjustments within one class due to natural processes such as climate changes). Hirata et al. (2001) indicated that conventional methods such as field survey for collecting environmental data such as field survey are time consuming and ineffective in providing the required information in a cost and time effective manner. Hence, remote sensing data gives an advantage of large area coverage and repetitive data acquisition for change detection analysis. For example, remote sensing data such as Landsat TM and ETM+, SPOT, AVHRR, IKONOS with digital format appropriate for computer processing have become the major data sources for different change detection applications during the past decades (Lu et al., 2004). Given in Table 2.3 is a summary of recent publication on change detection types.

Deer (1995) suggested three ways change detection analysis techniques can be done namely: pixel based, feature based and object based. Furthermore, Coppin et al. (2004) categorized the different change detection techniques based on the temporal characteristics into two classes which are bi-temporal change detection method (i.e., examines the changes between two fixed dates) and temporal trajectory analysis (i.e., a progressive change over a period). Lu et al. (2004) described seven types of change detection methods with fine spatial resolution such as Landsat, SPOT, or radar are: algebra, transformation, classification, advanced models, Geographical Information System (GIS) approaches and visual analysis. Lu et al. (2004) concluded from their review that principal component analysis, image differencing and post classification comparison are the most commonly used methods and that spectral mixture analysis, artificial neural network, Geographical information systems (GIS) and remote sensing data are now important methods for change detection applications.

Table 2.3: Some change detection applications using a remote sensing data.

Change Detection	**References**
Land-use or cover (LULC) change	Al-Gaadi et al. (2011), Odindi et al. (2012)
Environmental change	Armour et al. (1998)
Deforestation, regeneration and selective logging	Alves (2002)
Detection of landslide areas	Kimura and Yamaguchi (2000)
Flood monitoring	Liu et al. (2002)
Vegetation change	Muzein (2006)
Urban change	Okeke (2006)
Drought monitoring	Peters et al. (2002)
Desertification	Singh et al. (1990)
Landscape change	Taylor et al. (2000)
Forest fire and fire affected area detection	Tsela et al. (2014)

Berberoglu and Akin (2009) used change detection algorithms based on suitable threshold to determine the land use or cover change in the Mediterranean areas i.e. image differencing, image rationing, and image regression. Recently, from Northern Africa, El-kawy et al. (2011) concluded that the integrated visual interpretation and a supervised classification of satellite imagery is an effective technique to identify land use or cover changes in Egypt. Additionally, Coppin et al. (2004) earlier pointed out that time series analysis can resolve issues that can affect change detection results. Leverman (2013) observed that little attention is being paid to time series analysis (temporal trajectory analysis) especially on land cover monitoring on a continuous basis due lack of high temporal high resolution images. Although moderate resolution images such as MODIS are available to create a time series analysis, the low spatial details makes auto-classification difficult according to (Coppin et al., 2004, Jianya et al., 2008).

Furthermore, Lu et al. (2011) revealed the two classes change detection techniques which are:

- Binary change or non-change detection which involves select appropriate thresholds in both tails of the histogram representing the changed areas (Yool et al., 1997). These selection of threshold is carried out either by manual trial-and-error method (i.e., modifying the thresholds and assessing the resulting image until satisfied) or statistical measures. Some examples of non-change detection technique are image differencing, image rationing, vegetation index differencing, and PCA. Also, Lu et al. (2004) pointed out the disadvantage of threshold method which includes, sensitivity to external influence and its subjective nature and scene dependent.

- From-to change detection are mainly rely on the classification accuracy for each date being analysed i.e., the final change detection accuracy depends on classification errors from the analysed separately dated images (Jensen, 2005). Some examples are post classification comparison and hybrid change detection methods (Lu et al., 2004).

Although many changes detection studies have been done using remote sensing data, there is still no conclusion on the most effective techniques to use, according to Jianya et al. (2008). Therefore, choosing a perfect change detection algorithm is therefore of great importance and needs careful consideration (Coppin et al., 2004).

2.4 Remote sensing of impervious surfaces

Impervious surfaces are man-made features that do not allow water to infiltrate through. Examples of these impervious surfaces include roads, driveways, sidewalks, parking lots, rooftops, concrete, asphalt, stone etc. (Okeke, 2006, Weng, 2012). Impervious surfaces have a wide range of environmental implications (human-environmental interactions and environmental change or global warming) and therefore it has become necessary to map and estimate changes in impervious surface areas (Weng, 2012). Literature reveals that various techniques has been used in the past to characterize and quantify impervious surfaces. These method are can be grouped into two, namely: Ground measurements or field survey and use of manual digitizing from hard-copy maps or remote sensing data .Ground measurements or field survey with GPS are very costly and time consuming but provides a reliable information on impervious surfaces. The use of manual digitizing from hard-copy maps or remote sensing data (especially aerial photographs) have also been used for mapping imperviousness. Due to technological advancement over the years, automated methods such as scanning,

machine learning and feature extraction algorithms have also been used for extraction of impervious surface areas (Weng, 2012). The development of satellite imagery in the 1970s - 1980s also gained popularity in natural resources and environmental studies. Furthermore, (Brabec et al., 2002) reported on the four different methods which involved; Using a plainmeter to measure impervious surface on aerial photography, counting the number of intersections on the overlain grid on an aerial photograph, conducting image classification and assessing impervious surface coverage through the percentage of urbanization in a region. Brabec et al. (2002) and Slonecker et al. (2001) studies revealed that in the 1970s and 1980s, aerial photography was the main source of remote sensing data for assessing and mapping impervious surfaces. Literature via Scopus, also revealed that the number of publications produced were limited in the 1990s due to the lack of remote sensing data suitable for identifying and assessing impervious surface types, limited digital image processing methods and computing power (Weng, 2012).

During the 21st century, remote sensing of impervious surfaces speedily gained interest amongst the remote sensing community judging from the annual publications and citations. The average number of citations per article per year on remote sensing of impervious surfaces was 0.82 between 2001 and 2010, while the number of citations per year for the entire field of remote sensing was 0.55 for the same time frame (Figure 2.1). The evaluation showed that remote sensing of impervious surfaces has become one of the most dynamic fields in remote sensing (Weng, 2012). Furthermore, the advent of high-resolution imagery (less than 5 m resolution) together with more sophisticated image processing techniques improved the remote sensing of impervious surfaces. Parece and Campbell (2013) showed that many researchers admitted that high-resolution imagery also has the problem of heterogeneity (mixed pixel) i.e., different spectral values of various end members within the pixel size. In spite of the spatial resolution of Landsat imagery (30m pixel size) for urban analysis, it still has an advantage of affordability, accessibility, multispectral coverage, sequential acquisition and spatial coverage of urban studies (Parece and Campbell, 2013).

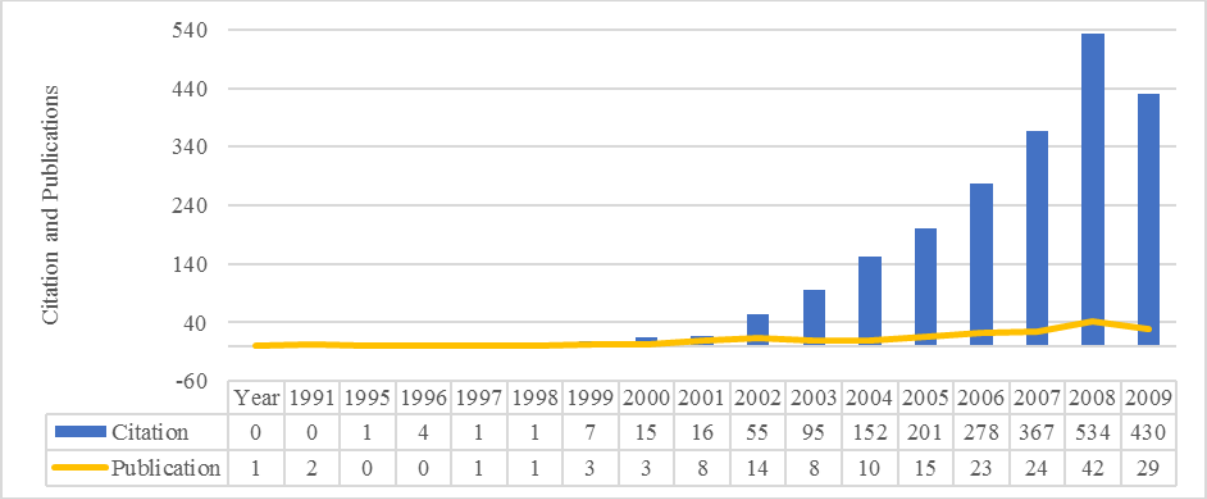

Year	1991	1995	1996	1997	1998	1999	2000	2001	2002	2003	2004	2005	2006	2007	2008	2009
Citation	0	0	1	4	1	1	7	15	16	55	95	152	201	278	367	534	430
Publication	1	2	0	0	1	1	3	3	8	14	8	10	15	23	24	42	29

Figure 2.1: Yearly publications and citations from 1991 to 2010 indexed by Scopus (adapted from Weng (2012)).

Recently, tabular representation showing selected literature on a variety of techniques in urban impervious surface areas in various places around the globe has been reported in Weng (2012) and Parece and Campbell (2013). Recently many government agencies and non-government organizations have started to gather and map impervious surface data for various uses. Earlier researchers such as Radeloff et al. (2005) showed that housing density has been used as an indicator for urban expansion in the past. This housing density parameter is often derived from census data but its application in urban sprawl studies has limitations. For instance, census blocks were often too coarse and not timely for monitoring purposes. This is because the census block is up-dated at decadal intervals which might complicate studies on urban expansion by introducing spatial mismatch between boundaries of different datasets (Hammer et al., 2004). According to Sutton (2003), the nonlinear differences of the total population are due to different scale of measurements. This complicates the identification of urban expansion in a uniform spatial context. In addition, many studies have shown that impervious surfaces are an indicator of urban expansion (Powell et al., 2008). Nevertheless it has also been revealed that impervious surface is man-made landscapes that can be identified and quantified using remote sensing technology. Many factors ought to be taken into consideration when using remote sensing technology according to Lu and Weng (2007). Some of which are user's requirement, research objectives, remotely sensed data available, compatibility with previous work, availability of image processing algorithms and computer software, and time constraints. Since remote sensing data differ in spatial, geometric,

radiometric, spectral, and temporal resolutions,Weng (2012) indicated that the understanding of the strength and weakness of various remote sensing data is significant in selection of the type of image processing methods to be used.

Bauer et al. (2007) used the inverse correlation between impervious surface and vegetation covers in urban as a potential approach for impervious surface extraction, i.e., through information on vegetation abundance. Likewise, Carlson and Ripley (1997) showed that the Normalized Difference Vegetation Index (NDVI) or greenness derived from tasselled cap transformation or principal component analysis can be used to represent vegetation. Impervious surfaces were then assessed by the complement of vegetation fraction or by regression models with vegetation indices. Most of these studies employed used coarse- and medium-resolution satellite imagery e.g., AVHRR imagery, MODIS, Landsat MSS and TM imagery which were taken in different seasons (e.g. Leaf-on and leaf-off season) facilitating the underestimation of vegetation leading to the overestimation of impervious surface coverage (Weng, 2012). Furthermore, Bauer et al. (2007) established a regression modelling method correlating impervious surface area extracted from panchromatic digital orthophoto quadrangles to Landsat tasselled cap derived greenness. The aim of work reported in Bauer et al. (2007) was to assess and map the impervious surface in the state Minnesota. Chabaeva et al. (2004) established a land use estimation model. Regression technique was extended by Yang et al. (2003) developing a classification and regression tree (CART) algorithm. The CART algorithm employed the classification result of high resolution imagery and use them as a training dataset to create a rule-based modelling for estimating of sub-pixel percent imperviousness for a study area. According to Weng (2012), the regression trees are created using a partitioning algorithm to build a tree by repetitive splitting of the training sample into smaller subsets to reduce the model's combined residual error for the subset. Xian (2007) stated that the advantage of the regression tree algorithm was to simplify complex non-linear relationship between predictive and target variables into a multivariate linear relation and to accommodate both continuous and discrete variables as input data for continuous variable prediction. Additionally, the application of regression method used for medium resolution imagery data has also been applied to coarse resolution image, e.g. MODIS derived NDVI (Lu et al., 2008) and DMSP/OLS (Elvidge et al., 2007). Similar approach, involving the use of finer resolution data was used for calibrating, authenticating, and projecting impervious surface area. The estimation of impervious surfaces using regression methods (multivariate

regression or CART) as reported by Weng (2012) also had limitations associated with model calibration, validation, and extrapolation of the models in other study areas.

Linear spectral mixture analysis (LSMA) had been used for ISA extraction (i.e., quantitative sub-pixel information) due to its performance in handling the problem of spectral mixture (Roberts et al., 1998). The LSMA methodology has been widely employed in the assessment of impervious surfaces in recent years (Powell et al., 2007). Various algorithms have also been developed for extracting impervious surface areas based on the LSMA model. Phinn et al. (2002) extracted impervious surfaces as one of the endmembers in the standard SMA model. The use of high-albedo and low-albedo fraction images together can also be used to evaluate impervious surface areas (Weng et al., 2009). Nevertheless, some of the limitations associated with LSMA technique reported in Weng (2012) are; (a) overestimation of ISA in the areas with small amounts of impervious surfaces (b) underestimation in the areas with large amounts of impervious surfaces and (c) spectral properties of non-photosynthetic vegetation, soil, and several impervious surface materials makes it difficult to separate impervious from pervious materials. He also pointed out that, shadows caused by tall buildings and tree canopies in the urban landscape may lead to underestimation of impervious surface area with high-resolution imagery.

Most urban landscapes consist of numerous impervious surfaces in terms of type, abundance and geometry. As a result, identifying one suitable end member to be a representative of all the impervious surfaces is often difficult. Lu and Weng (2004) recommended that three possible methods could be used to solve these problems: Stratification, multiple end members, and hyper spectral imagery. The creation of multiple end member SMA (MESMA) method reported in Powell et al. (2007) and Franke et al. (2009) uses a series of candidate two-end member models. Each model is then assessed based on the measures of fractional values, root mean square error, residual threshold and finally produces the fraction images with the lowest error according to the previous works of Roberts et al. (1998). Another limitation of LSMA previously described in Foody et al. (1997) was the selection of end-members related with within-class spectral variability. This was overcome by Wu (2004) who improved his technique of impervious surface assessment by normalizing spectral data (i.e., Normalized spectral mixture analysis, NSMA) before using LSMA. Also, Yang et al. (2010) point to that the pre-screened and normalized multiple end member spectral mixture analysis (PNMESMA) method was better than previous methods (LSMA, NSMA, LSMA-LST, and

MESMA). This was because the estimated error or overall root mean square error was reduced to 5.2% and that there was no noticeable underestimation or overestimation of impervious surface areas.

Even though image classification has been the most extensively used methods of extraction of ISA, results are often not adequate (Okeke, 2006). This is because heterogeneity of urban settlements are difficult to estimate in a medium resolution imagery. For example, inconsistent selection of representative training areas due to the 30m resolution could affect the accuracy of image classification (Weng, 2012). Civco et al. (2002) reported that extraction and quantification of ISA could be done at the sub-pixel level together with ground truthing. Furthermore, Carlson and Arthur (2000) calculated the percent of impervious surface per pixel using fractional vegetation derived from scaled normalized difference vegetation index (NDVI). Yang et al. (2003) recommended the general classification and Regression Tree (CART) method using Landsat satellite data derived Tasselled Cap transformed data. Although, Ridd (1995) proposed the vegetation–impervious surface–soil (V–I–S) model to identify the biophysical composition of the urban landscape, but was improved by Lu and Weng (2006) using four end-members i.e., High-albedo, low-albedo, together with soil and vegetation extracted from the image. Lu and Weng (2006) assumption was that land covers in urban landscapes are in a linear combination of three components, namely, vegetation, impervious surface, and soil. Nevertheless, the limitations of these methods were the confusion among classification of dry soils that are mixed with water, building shadows, vegetation shadows, and dark impervious surface materials which over-estimated the magnitude of impervious surface (Lu and Weng, 2006). This was solved using expert rules developed from sample plots using high spatial resolution aerial photos. Weng and Lu (2009) recently adopted the new concept of merging the benefits of Vegetation-Impervious Surface-Soil (VIS) and Linear Spectral Mixture Analysis (LSMA) to better describe and estimate the spatial-temporal changes of the urban area.

With the availability of fine spatial resolution data (<5 m) such as IKONOS and QuickBird, the mapping of ISA has improved due to the reduced mixed pixel problem, providing a greater improvement of extracting more detailed information on land cover types (Weng, 2012). According to Lu and Weng (2009), high-resolution imagery has been used to separate dark impervious surface areas and shadowed from water and shaded areas created by tree crowns. Lu and Weng (2009) further established that a combination of techniques involving

decision tree classifier and unsupervised ISODATA classifier to extract impervious surfaces from IKONOS images. Maximum likelihood classifier, ISODATA, and a rule-based classification algorithm applied to digitized aerial photos and LIDAR data in Richland County, South Carolina were also compared by Hodgson et al. (2003). They found that maximum likelihood classifier produced the highest accuracy while the ISODATA the had the lowest.

Even though large-scale impervious surface mapping have been executed using various methods, the techniques used for mapping are complex due to varying image quality and scales together with mixed pixel problems when assessing of a large geographical area. Thus, in this research, a both ML and RF classifiers were employed to extract the impervious surface areas over Tshwane metropolitan, Gauteng Province, South Africa.

2.5 Land surface temperature responses to land use or cover changes

The most significant environmental impact resulting from the modification of the physical properties of the land surface due to land conversion (i.e., transformation of land cover from one class to a completely different class) is the changes in land surface temperature (LST) and atmospheric temperature (Deng and Wu, 2013). Surface temperature are affected surface energy change, anthropogenic heat discharge, building energy consumption and atmospheric pollution. They can be detected at a large geographical scale (urban–rural surface temperature difference) which is known as urban heat island (Lu and Weng, 2006). Deng and Wu (2013) appraised that the earlier method of assessing surface temperature variability involved the simulation of UHI phenomenon and its spatial pattern using governing equations for fluid mechanics such as an energy balance equation, etc.) together with in-situ measurements or laboratory experimental data. The main simulation models they pointed out were: energy balance models (Tong et al., 2005) and dynamic numerical simulation methods (Yuan et al., 2008). Sun (2008) also mentioned the use of sheltered thermometer above a flat grassy and well ventilated surface to estimating surface-air temperature.

Rao (1972) reported the earliest urban surface temperature observations from satellite-based sensors. Since then, sensors at various platform (i.e., satellite, aircraft and ground based) have been used to observe of the surface temperature. Voogt and Oke (2003) also reviewed some studies that have applied thermal remote sensing to study urban climates in the past. Since remote sensing offers the chance to detect electromagnetic radiation (EMR), see Figure 2.2

by sensors on a remote sensing platform, it has been beneficial in the analysis of spectral response of different objects (Tomlinson et al., 2011). According to (Lillesand et al., 2004), LST measurements are mainly carried out using the thermal infrared (TIR) region. Tomlinson et al. (2011) further explained that electromagnetic radiation (EMR) received at satellite thermal infrared sensors is measured as Top Of Atmosphere (TOA) radiances i.e. upwelling radiance (emitted from the ground and atmosphere), and the downwelling radiance (emitted by the atmosphere and reflected from the ground). He further described that during the day there is both emission and reflection of EMR while at night sensed EMR is limited to only emission.

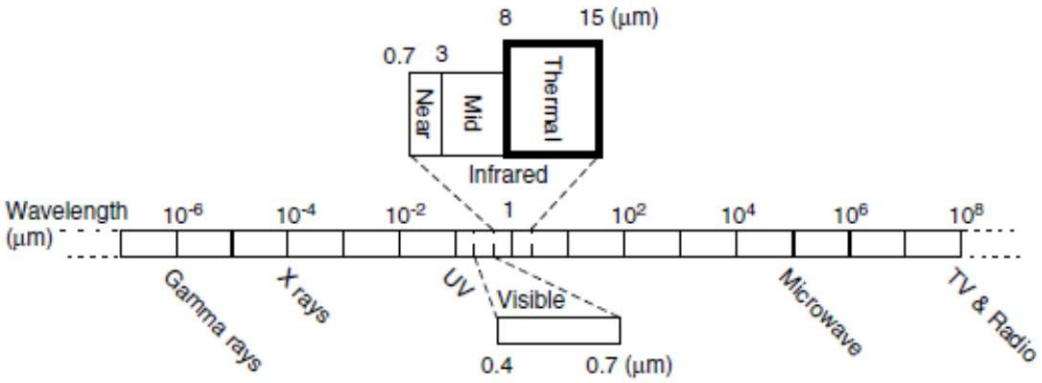

Figure 2.2: The electromagnetic spectrum arranged by wavelength. Adapted from Lillesand et al. (2004).

Additionally, Tomlinson et al. (2011) pointed out that LST is derived from TOA radiance by modifying three main effects which are absorption, reflection and scattering due to water vapour and aerosols. These effect changes the EMR as it passes through the atmosphere resulting in variations in viewing angles and wavelength shifting which must be compensated for when estimating radiances and spectral emissivity values at the surface (Dash et al., 2002). In addition, emissivity is done by considering the ratio of energy emitted by a surface with respect to the energy emitted by a black body at the same temperature. Since most surfaces don't behave like blackbody there is need for correction of calculated emissivity values as reported by Tomlinson et al. (2011). They further indicated that the correction is done using complex algorithms together with extensive validation and verification to produce a product applied to the meteorologist.

Dominguez et al. (2011) also reported on some algorithm which has been used for LST retrieval from thermal bands such as split-window techniques and the radiative transfer equation (RTE) which have been described in Dash et al. (2001) and (Weng, 2009). Tomlinson et al. (2011) applied split window technique on the thermal bands of AVHRR, MODIS and SEVIRI products and also used adjacent channels with different properties to calculate atmospheric attenuation. Yu et al. (2008) reviewed nine different split window algorithms and concluded that accuracies are dependent on emissivity data acquired earlier. Tomlinson et al. (2011) also reported that it is difficult to assess large areas using remote sensing data except with the assumptions of average emissivity across a heterogeneous area. In addition, studies by Deng and Wu (2013) demonstrated that certain models have been used to examine the relationships between land surface temperature and spectral indicators created from remotely sensed data. Linear regression models have been widely used to explore the relationships between LST and biophysical and socio economic factors. Some of these biophysical and socio economic factors are; land use and land cover (LULC) type and change (Amiri et al., 2009), intensity of human activity (Elvidge et al., 1997), geometry of street canyon (Bottyán and Unger, 2003), population density and distribution (Xiao et al., 2008), and impervious surface area (Imhoff et al., 2010) etc. Although many spectral indices have been developed for analysing UHI by extracting LST from remotely sensed data, Weng et al. (2004) earlier showed that they are still insufficient to fully characterize urban landscape thermal characteristics and patterns. Deng and Wu (2013) also reported that non-linear statistical models have also been employed to describe the intensity and magnitude of urban microclimate and UHI. Some of these examples are; association rule mining technique (Rajasekar and Weng, 2009), Gaussian model (Streutker, 2003) etc. Furthermore, vegetation cover pixels show significant differences in LSTs due to different background substrates (i.e., moist or dry soil have different thermal properties). Earlier works of Ridd (1995) also showed that though spectral metrics can be used in describing urban LST characteristics, it omit impacts of soil, which is observed as one of the most essential land compositions. Hence, it is necessary to consider thermal properties of different urban land cover during LST estimation (Friedl, 2002).

Aderoju et al. (2013) recently assessed the urban heat island in Akure, Nigeria, West Africa, using Radiative Transfer Method as an effective way of estimating LST using Landsat 7 ETM+. They concluded that the most extensive UHI was distributed in the central part of

the Central Business District. Jiménez-Muñoz et al. (2009) used the Landsat thermal-infrared (Band 6) to retrieve LST over Catalonia (north-east of the Iberian Peninsula, Spain) using an extension of the generalized single-channel (SC) algorithm developed by Jime´nez-Munˇ oz and Sobrino (2003) which depends on concept of atmospheric functions which relies on atmospheric transmissivity and upwelling and downwelling atmospheric radiances. They tested the accuracy of their result using a land surface temperature map obtained from one Landsat-5 image acquired over an agricultural area using inversion of the radiative transfer equation and the atmospheric profile measured in situ at the sensor overpass time. The comparison with this "ground-truth" map provided a root mean square error of 1.5 K. Tomlinson et al. (2011) based on review on remote sensing LST in Birmingham, UK also specified the limitation of single channel algorithm on Landsat TM/ETM+ products and considered them less accurate because of the influence of atmospheric attenuation at the time of overpass. Similarly, Qin et al. (2001) detailed the mono window algorithm based on the thermal radiance transfer equation, putting into consideration three parameters (emissivity, transmittance and effective mean atmospheric temperature) to retrieve LST for the sand dunes across the Israel- Egypt border using Landsat TM data. They concluded that the mono window algorithm is able to provide an accurate land surface temperature retrieval from Landsat imagery. Ifatimehin et al. (2009) also evaluated the effect of land use/cover change on the surface temperature of Lokoja town, Nigeria using Landsat TM and ETM+ employing the mono window algorithm. They reveal that there is a direct relationship between the land use/cover changes and the variations in the surface temperatures. Alipour et al. (2011) estimated the LST of Alashtar city, Iran from thermal bands of Landsat sensors using both the mono window algorithm developed by Qin et al. (2001) and the single channel algorithm developed by Jime´nez-Munˇ oz and Sobrino (2003). They finally compared the LST measured in situ with the retrieved ones from the algorithm and the result revealed that mono window R^2= 0.85 while the single channel algorithm R^2= 0.79. Subsequent studies on LST retrieval include comparing LST and air temperatures over large areas and multiple ecosystems in Africa (Vancutsem et al., 2010) using MODIS LST data to estimate the air temperature in China (Yan et al., 2009), using SURFRAD to Verify the NOAA Single-Channel Land Surface Temperature Algorithm (Heidinger et al., 2014) and so on.

Although, differences between satellite derived LST and ground measured air temperature at various land extent (town, city, municipality, province and continental) is still subject to

ongoing work at various countries around the globe, very little is being carried out in major cities in Africa despite the availability of thermal satellite data. The next section presents the data and methodology employed in carrying out this research.

3 CHAPTER THREE: DATA AND METHODOLOGY

3.1 Study area

Tshwane Metropolitan is located between S25°19'17.78" E27°53'05.52" (top left) and S25°56'49.95" E28°26'45.7" (bottom right) northeast of Johannesburg city, Gauteng Province, South Africa (Figure 3.1). It is situated in a transitional belt between the plateau of the Highveld to the South and the lower-lying Bushveld to the North in South Africa. The city has a land area of 2,198 km^2 and altitude of about 1,350 m (4,500 ft) above sea level, in a warm, sheltered, fertile valley, surrounded by the hills of the Magaliesberg range. It is one of South Africa's three capital cities representing the administration and de facto national capital alongside others which are Cape Town, (Legislative capital) and Bloemfontein (Judicial capital). The Tshwane Metropolitan is divided into three sections which are Pretoria West, Pretoria East and Pretoria North (StatisticsSouthAfrica, 2011). Pretoria is located within the City of Tshwane Metropolitan Municipality (6,298 km^2) as one of several constituent former administrations along with Centurion and Soshanguve. The geographical distributions of the major languages in Pretoria are Afrikaans, English, Ndebele, Zulu, Nothern Sotho, Tswana and Tsonga.

Tshwane Metropolitan has various cultural influences and this is reflected in the architectural styles that can be found in the city e.g. British Colonial Architecture and other uniquely South African styles. Some of the notable structures in Pretoria include the Voortrekker Monument, Mahlamba Ndlopfu, Union Buildings, Reserve Bank of South Africa, the Telkom Lukas Rand Transmission Tower, Loftus Versfeld Stadium, The South African State Theatre, University of Pretoria, CSIR, Pretoria National Botanical Garden, the National Zoological Gardens of South Africa, Groenkloof Nature Reserve, Rietvlei Nature Reserve, Moreletaspruit Nature Reserve, Wonderboom Nature Reserve, Church Square, Menlyn Park, Hatfield Square and so on. Furthermore, the CBD (Central business district) of Pretoria is the traditional centre of government and commerce, with many corporate offices, small businesses, shops and government departments located in Pretoria's sprawling suburbs rather than the CBD. National Departments with their Head Office in the CBD include: Department of Health, Basic Education, Transport, Higher Education and Training, Sport and Recreation, Justice and Constitutional Development, the National Treasury and Water and Environmental Affairs.

Transportation within the city are of different types namely: railways such as Metrorail with routes originating from the city centre, extending south to Germiston and Johannesburg, west to Atteridgeville, northwest to Ga-Rankuwa, north to Soshanguve and east to Mamelodi, the Gautrain which is a high speed railway line that runs from the eastern suburbs of Hatfield to Pretoria Station, Centurion, Sandton, and Oliver Tambo International Airport and Johannesburg, Rovos rail which operates from the colonial-style railway station at Capital Park (Capital Park, 2008). Buses from companies both governmental and private companies are also a source of transportation e.g. Tshwane municipality buses, private taxis and so on.

Tshwane has a high altitude of about 1350 metres coupled with a moderately dry, humid subtropical climate (i.e., hot and rainy summers and short cool and dry winters) with an average annual temperature of 18.7°C (Hansen et al., 2010). This climatic condition might be due to the sheltered valley position, which traps the heat and cuts it off from cool southerly and southeasterly air masses for much of the year. Rain is predominantly in the summer months with an average 715 mm of precipitation annually and the driest month is June (6 mm) while the wettest month is January (122 mm). Drought conditions usually occur during the winter months, when frosts may be sharp, but snowfall is an extremely rare event. Snowflakes were spotted in 1959, 1968 and 2012 in the city, but the city has never experienced an accumulation in its history (WeatherNetwork, 2012). During a nationwide heat wave in November 2011, it was observed that Tshwane Metropolitan temperatures rose up to 39°C, extremely unusual for that time of the year. Likewise extreme heat events also transpired in January 2013, when SAWS (2013) reported that Pretoria experienced temperatures above 37°C for several days which eventually resulted in all-time highest recorded temperature of 42°C on 25 January 2013.

During the past decades, Tshwane metropolitan experienced a constant growth in population and expansion. The estimated population range according to the population census of 2001 was 500,000 and after the 2011 annexation of the Metsweding District Municipality is now 2.950 million (StatisticsSouthAfrica, 2011). This sprawl has generated various urban land use types that continuously necessitate the construction of new ISA replacing agricultural lands in the city.

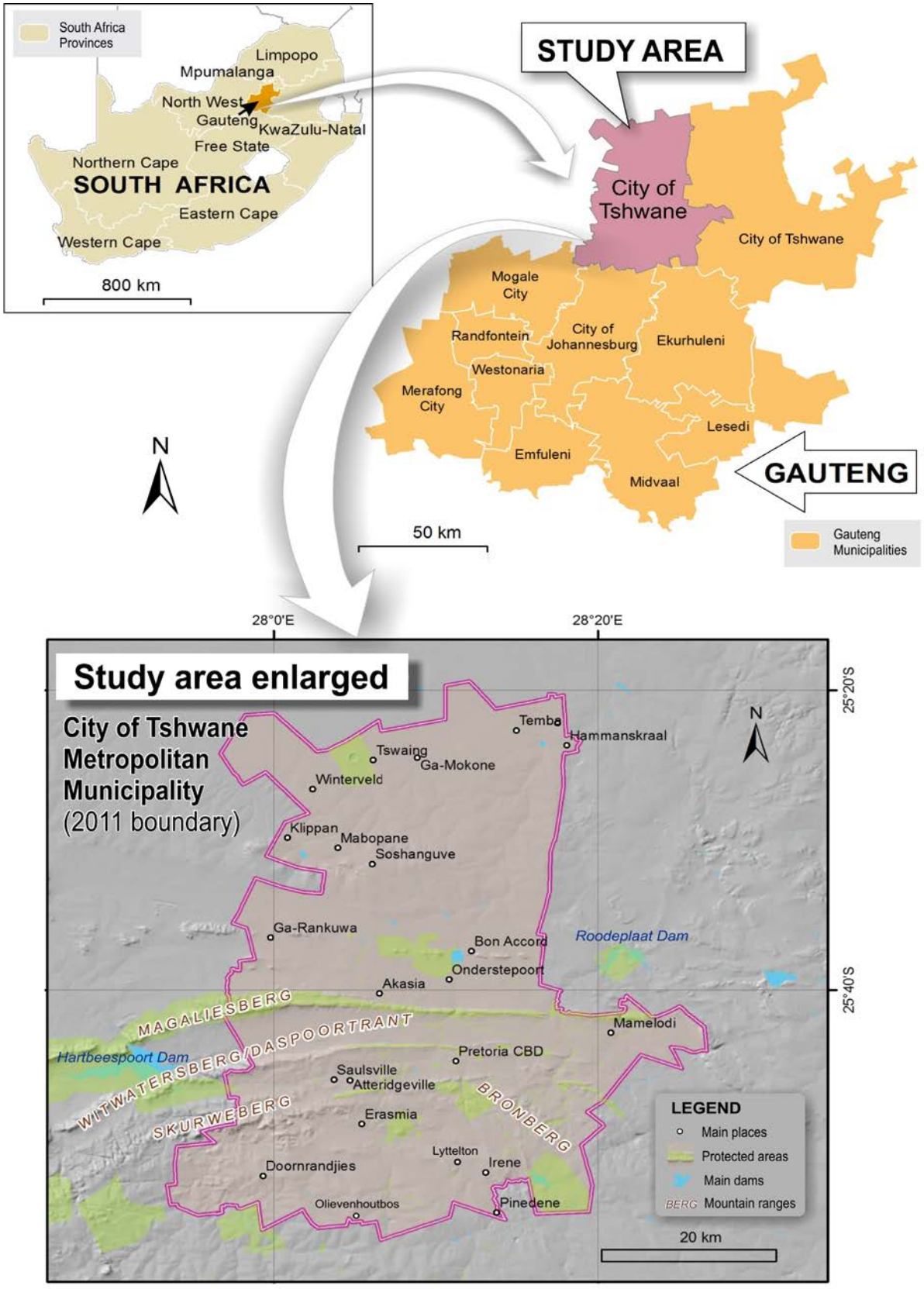

Figure 3.1: Map showing the location of Tshwane Metropolitan, within the Gauteng Province in South Africa.

Due to the adverse effect of urban complex landscape (i.e., urban heat island), it has become necessary to have an up-to-date assessment of impervious surface area changes and investigate its contributions to land surface temperature variations across Tshwane Metropolitan.

3.2 Data and methods

3.2.1 Introduction

This section gives a brief introduction of the data and methodology used in the study. In particular, both primary and secondary data sources were used. The primary datasets includes field observations and information acquired with the aid of a handheld GPS. (Geographical positioning system) and the Analytical Spectral Device (ASD) on a 30m × 30m plot with a homogenous area of the land use or cover class across the City of Tshwane. The secondary data for the study includes a series of cloud free Landsat images of the study area acquired from years 2003 and 2013. The primary goal of the research study is to use moderate resolution Landsat ETM+ and Landsat 8 LCDM to investigate the changes in impervious surface area and land surface temperature of Tshwane metropolis, Gauteng province, South Africa. Figure 3.2 illustrates the schematic flowchart of the methodology adopted.

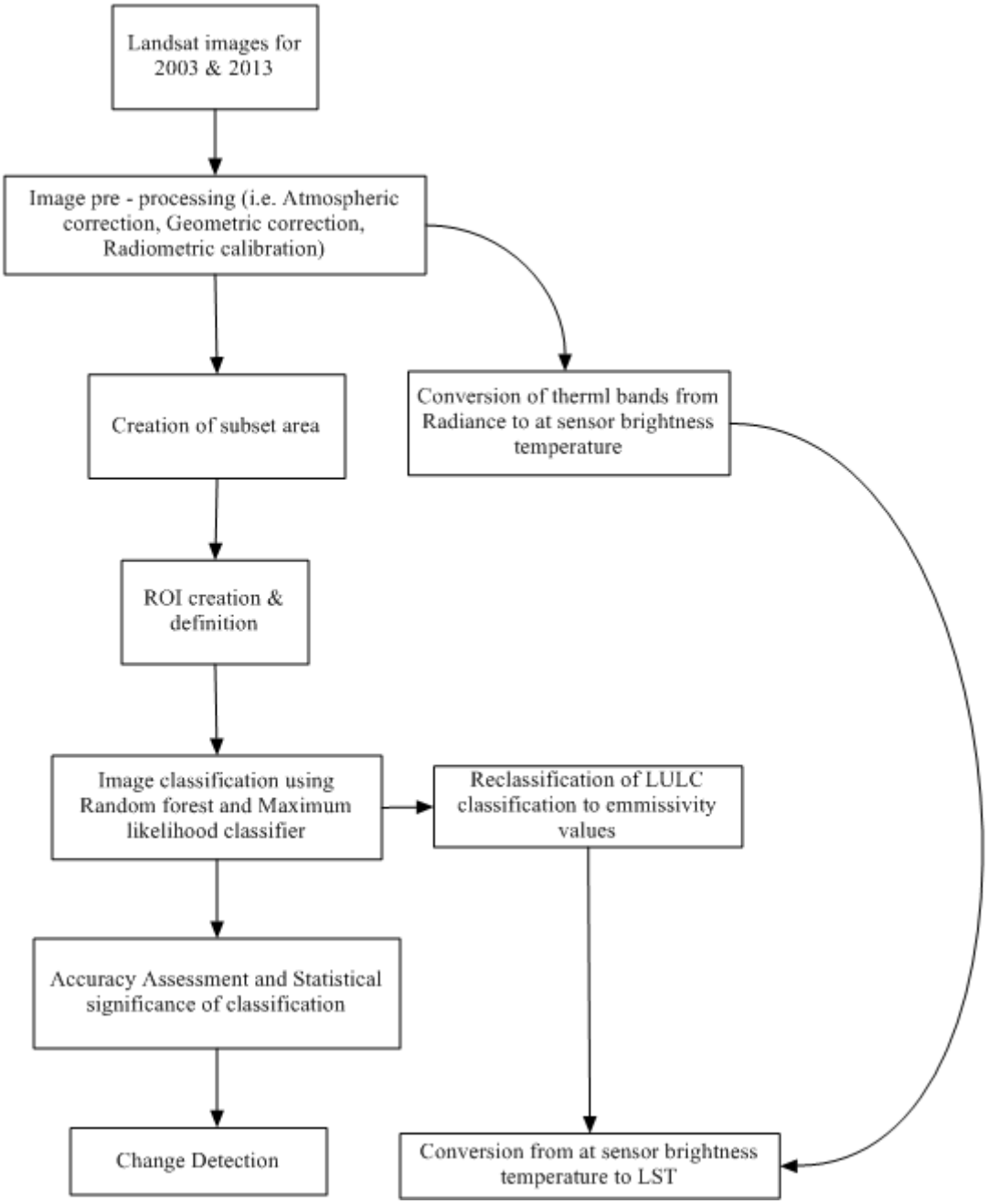

Figure 3.2: Methodological framework showing the important phases used in this research.

3.3 Data type and sources

3.3.1 Landsat 7 ETM+

Landsat 7 ETM+ was launched on April 15, 1999 from Vandenburg Air Force Base, CA, into a sun-synchronous orbit. This is a three- axis stabilized platform carrying a single nadir-pointing instrument with a revisit interval of 16 days (Jensen, 2007). Landsat 7 ETM+ is a

derivative of Landsat 4 and 5 TM sensors and it's based on a scanning technology even though there has been linear array push broom technology, which has been made available since the launch of SPOT 1 in 1986 (Jensen, 2007). The ETM+ sensor is a multispectral scanner that has three on-board calibration devices for the reflective bands which are; the Full Aperture Solar Calibrator (FASC) which is a white painted diffuser panel, Partial Aperture Solar Calibrator (PASO) which is a set of optics that allows the ETM+ to image the Sun through small holes and IC which consists of two lamps, a black body, a shutter, and optics to transfer the energy from the calibration sources to the focal plane (Chander et al., 2009). The sensor was calibrated using Earth targets (e.g. Railroad Valley) according to (Thome et al., 2004) and cross-calibrated with multiple sensors according to Chander et al. (2008).

Table 3.1 shows the spectral and spatial characteristics of the Landsat 7 ETM+ with band 1 through 5 and 7 being identical to those found on Landsat 4 and 5 with a spatial resolution of 30 m, thermal infrared band 6 has 60m and 15m panchromatic band (Chander et al. 2009). As reported by Jensen (2007), Landsat 7 ETM+ sensor at an altitude of 705km above the earth's surface and collects data in a swath width 185 km wide and cannot view off-nadir. The Landsat 7 ETM+ scene considered in the present study is path 170 and row 078 and defined by World Reference System-2 (WRS-2). The WRS-2 allows efficient search and retrieval of the requested imagery for fractional surface of the earth (http://landsat.usgs.gov). The Landsat 7 ETM+ data set used was acquired 31st of March, 2003 covering 95% of Gauteng province but with focus on City of Tshwane South Africa. The multispectral imagery was provided by Glovis.usgs.gov in tiff format processed to a level 1T (terrain and precision corrected).

3.3.2 Landsat 8 LCDM

The Landsat Data Continuity Mission known as Landsat 8 after on-orbit initialization and verification was launched from Vandenberg Air Force Base in California on February 11, 2013 at the top of an Atlas V rocket. The U.S. Geological Survey (USGS) and National Aeronautics and Space Administration (NASA) continued mission to acquire high-quality data met both USGS and NASA scientific and operational requirements for earth observations e.g. Land use and land cover change (http://ldcm.nasa.gov/). The Landsat 8 spacecraft was built by Orbital Sciences Corporation with a 5-year mission design life; it shows enough fuel for 10 years of operation. The LCDM centrepiece of the observatory is the Operational Land Imager (OLI), which was designed and assembled by the Ball Aerospace

and Technologies Corporation (http://ldcm.nasa.gov/). By collecting land-surface data with spatial resolution and spectral band specifications consistent with historical Landsat data, the OLI instrument advances future measurement capabilities while ensuring compatibility with historical data (U.S. Geological Survey, 2013).

Table 3.1: Spectral and spatial characteristics of the Landsat 7 ETM + multispectral scanner (adapted from http://landsat.usgs.gov).

Landsat 7 ETM + Sensor				
Band Name	**Bandwidth (µm)**	**Resolution (m)**	**Combinations**	**Bands**
Band 1 Blue	0.45 – 0.52	30	Colour infrared	4,3,2
Band 2 Green	0.52 – 0.60	30	Natural colour	3,2,1
Band 3 Red	0.63 – 0.69	30	False colour	5,4,3
Band 4 NIR	0.77 – 0.90	30	False colour	7,5,3
Band 5 SWIR 1	1.55 – 1.75	30	False colour	7,4,2
Band 7 SWIR 2	2.09 – 2.35	30		
Band 8 Pan	0.52 – 0.90	15		
Band 6 TIR	10.40 – 12.50	30/60		

Landsat 8 LCDM uses as a push-broom sensor with a four-mirror telescope, higher signal-to-noise performance and 12-bit quantization. The OLI collects data (Table 3.2) in the visible (Band 2, 3, 4), near infrared (band 5), and shortwave infrared wavelength regions (band 6 SWIR 1 and band 6 SWIR 2), thermal infrared band (band 10 TIRS 1 and 11 TIRS 2) as well as a panchromatic band (band 8). In comparison to Landsat 7 ETM+, two new spectral bands have been added: a deep-blue band of coastal water and aerosol studies (band 1), and a band for cirrus cloud detection (band 9) (Figure 3.3), together with an assurance band to indicate the presence of terrain shadowing, data artefacts, and clouds. Furthermore, the Thermal Infrared Sensor (TIRS) which are band 10 TIRS 1 and 11 TIRS 2, made by NASA Goddard Space Flight Center were to continue thermal imaging. This was to support evolving applications such as modelling evapotranspiration for monitoring water use consumption over irrigated lands, land surface temperature in climate change studies and so on. The TIRS

collects data has 100-meter spatial resolution registered for the OLI data to create radiometrically and geometrically calibrated, terrain-corrected 16-bit Level 1 data products (http://landsat.usgs.gov).

The Landsat 8 LCDM data are processed using parameters consistent with all standard Landsat data products that are available in various open source websites, for example Earth Explorer (http://earthexplorer.usgs.gov), Glovis (http://glovis.usgs.gov), or the Landsat Look (http://landsatlook.usgs.gov). For this research, the Landsat 8 LCDM was identified using path 170 and row 078 and defined by World Reference System-2 (WRS-2). The Landsat 8 data set used was acquired November, 13, 2013 covering 95% of Gauteng province, but with focus on City of Tshwane, South Africa and was provided by http://glovis.usgs.gov in tiff format processed to a level 1T (terrain and precision corrected).

Table 3.2: Spectral and spatial characteristics of the Landsat 8 LCDM (adapted from http://landsatlook.usgs.gov).

Landsat 8 LCDM sensor				
Band Name	**Bandwidth (µm)**	**Resolution (m)**	**Combinations**	**Bands**
Band 1 Coastal	0.43 – 0.45	30	Colour infrared	5,4,3
Band 2 Blue	0.45 – 0.51	30	Natural colour	4,3,2
Band 3 Green	0.53 – 0.59	30	False colour	6,5,4
Band 4 Red	0.64 – 0.67	30	False colour	7,6,4
Band 5 NIR	0.85 – 0.88	30	False colour	7,5,3
Band 6 SWIR 1	1.57 – 1.65	30		
Band 7 SWIR 2	2.11 – 2.29	30		
Band 8 Pan	0.50 – 0.68	15		
Band 9 Cirrus	1.36 – 1.38	30		
Band 10 TIRS 1	10.6 – 11.19	100		
Band 11 TIRS 2	11.5 – 12.51	100		

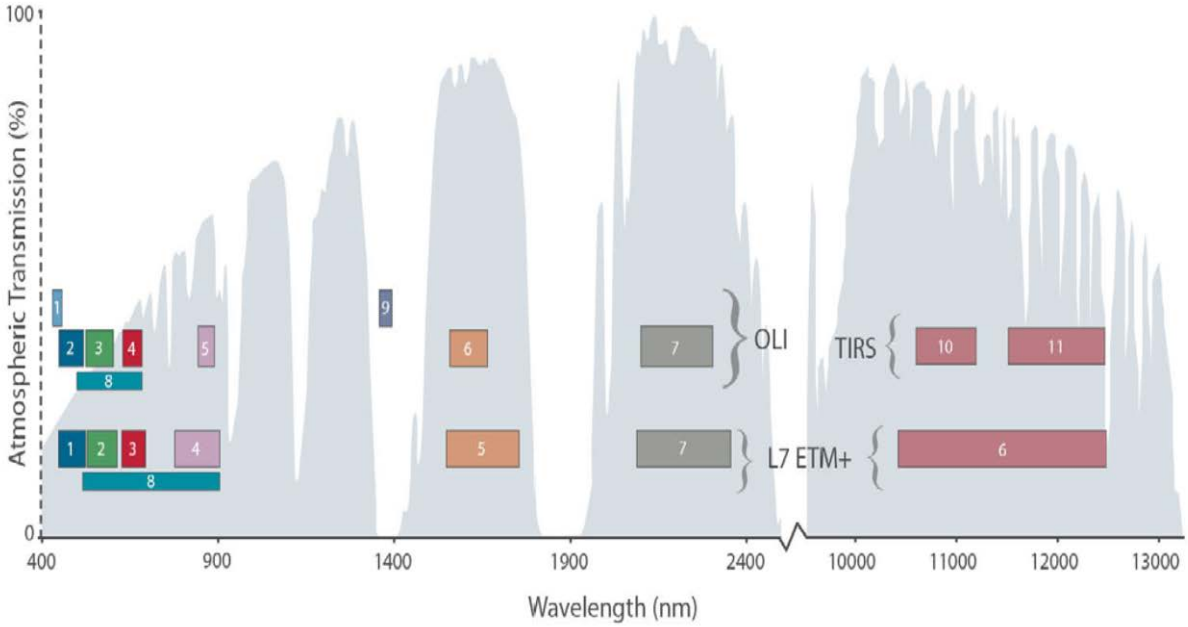

Figure 3.3: Comparison between Landsat 7 ETM + and Landsat 8 LCDM bands (adapted from http://ldcm.nasa.gov/).

3.4 Instrumentation and software

To store, analyse and display the collected remote sensing data and maps, software for Machine Learning (Random Forest), ESRI (ArcGIS 10.1) and EXELIS (ENVI 5.0) were employed to extract urban land cover types (with much focus on impervious surface), land surface temperature. Furthermore, the Analytical Spectral Devices (ASD) FieldSpec was then used for spectral data acquisition i.e., used for the measurement of reflectance. The instrument has a spectral range of 350 nm to 2500 nm. Other essential software employed in this study includes, RS3, ViewSpec Pro Version 6.0 (apart from being used to receive and store the spectral data transmitted from ASD Spectroradiometer, it was also used for conversion process of spectra data and save them in .asd format which is later converted to ASCII files of .txt format). Microsoft Excel 2010 was used to interpret the output data achieved by a conversion process into a graph which were used to present, describe and analyse the outcomes of the study and write up of the research report.

3.5 Reference data collection

In this study, it was necessary to employ ancillary data such as image spectrometry for field data acquisition such as various land cover type spectral signatures based on random point selection generated from Google earth images. These points were then uploaded into a global

positioning system (GPS) and used to navigate to the field sites. Once the sample point was located in the field, a 30m × 30m plot was created to cover a homogenous area of the land use or cover class. The GPS reading and spectral signatures (using the ASD field spec) of these LULC (Figure 3.5 and Figure 3.5) was then taken.

Figure 3.4: Photos showing the use of the ASD-field spec to collect spectral signatures of various LULC across Tshwane Metropolitan.

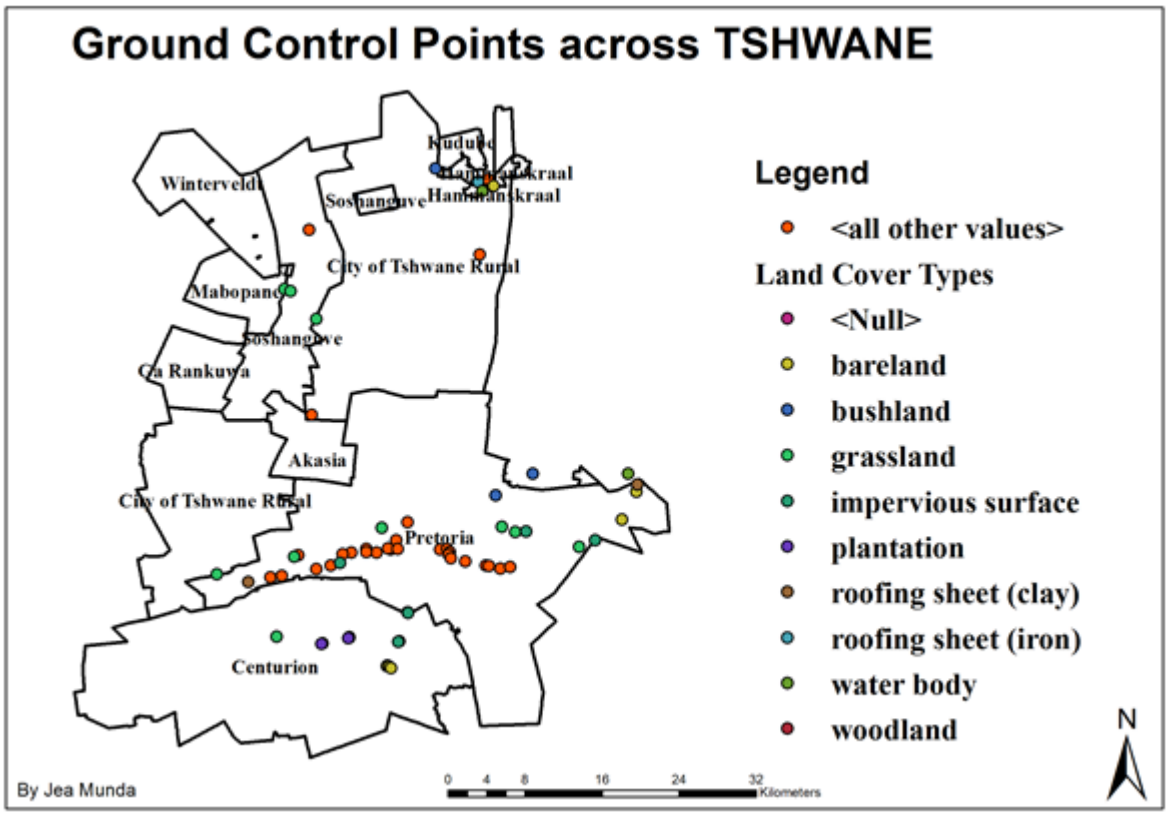

Figure 3.5: Map showing places the analytical spectral device-field spec and GPS were used across Tshwane Metropolitan.

Before taking recordings, the ASD was first used to acquire two types of radiant spectrum, which are dark current and white reference. Thereafter, the spectral signature for each LULC were acquired. Temperature data for the same date as the two Landsat images used, were also acquired from the South African weather stations and Pretoria Botanical Institute. Landuse map with a scale of 1:10,000 and shape file (Projection: WGS_1984_UTM_ZONE_35S) of the Tshwane Metropolitan was also employed. The Land use map and shapefiles were produced by the City of Tshwane Municipality but acquired from the Unit for Geoinformation and Mapping (UGM), Department of Geography, Geoinformatics and Meteorology, University of Pretoria, South Africa. Google Earth was also used to verify the urban landscape pattern of Tshwane Metropolitan. In conclusion, these were the reference data used to clip out the study area in the Landsat raster imagery for training site selection and preparing the urban map.

3.6 Data pre-processing

Data pre-processing is an important phase of satellite image processing and analysis, which has an impact on all other subsequent procedures and results. From the Figure 3.2 above the first step was to open the bands for Landsat 7ETM+ and Landsat 8 LDCM in ENVI Classic 5.0 ranging from visible bands (VIS) to short wave infrared (SWIR) and perform layer stacking of the bands before sub-setting via ROI using ENVI Classic 5.0. The ROI used in this case was the Tshwane Metropolitan vector file using the mask pixel outside of the ROI, selecting 'YES' and entering ZERO as mask background value. This was followed by assigning band centre wavelength to the stacked subset Landsat images. The quantitative analysis of surface reflectance is a critical satellite image pre-processing step so as to remove atmospheric effects such as the amount of water vapor, distribution of aerosols, and scene visibility must be known (Lillesand and Kiefer, 1999). According to Chander et al. (2009), radiometric calibration is also an important part of data pre-processing because it has the ability to provides precise (calibrated) and consistent measurements of the earth's surface features through time. During radiometric calibration, pixel values (Q) from raw, unprocessed thermal bands for the Landsat images used were converted to spectral radiance using 32-bit floating-point calculations. The absolute radiance values in the Landsat data employed for this research are scaled to 8-bit for Landsat 7 ETM+, Q_{calmax} = 255, and 16-bit for Landsat 8 LCDM, Qc_{almax} = 65535 numbers which represent Qcal before output to distribution media (http://landsat.usgs.gov). The conversion from Qcal back to at-sensor spectral radiance (L_λ) requires the following equations below:

For Landsat 7 ETM +:

$$L_\lambda = \left(\frac{LMAX_\lambda - LMIN_\lambda}{Q_{calmax} - Q_{calmin}}\right)(Q_{cal} - Q_{calmin}) + LMIN_\lambda \qquad [1]$$

Or

$$L_\lambda = G_{rescale} * Q_{cal} + B_{rescale} \qquad [2]$$

Where:

$$G_{rescale} = \left(\frac{LMAX_{\lambda} - LMIN_{\lambda}}{Q_{calmax} - Q_{calmin}}\right) \quad [3]$$

$$B_{rescale} = LMIN_{\lambda} - \left(\frac{LMAX_{\lambda} - LMIN_{\lambda}}{Q_{calmax} - Q_{calmin}}\right)Q_{calmin} \quad [4]$$

Where:

Q_{cal} = Quantized calibrated pixel value [DN]

Q_{calmin} = Minimum quantized calibrated pixel value corresponding to $LMIN_{\lambda}$ [DN]

Q_{calmax} = Maximum quantized calibrated pixel value corresponding to $LMAX_{\lambda}$ [DN]

L_{λ} = Spectral radiance at the sensor's aperture [W/ (m^2srµm)]

$LMIN_{\lambda}$ = Spectral at-sensor radiance that is scaled to Q_{calmin} [W/ (m^2srµm)]

$LMAX_{\lambda}$ = Spectral at-sensor radiance that is scaled to Q_{calmax} [W/ (m^2srµm)]

$G_{rescale}$ = Band-specific rescaling gain factor [W/ (m^2srµm))/DN]

$B_{rescale}$ = Band-specific rescaling bias factor [W/ (m^2srµm)].

For Landsat 8 LDCM:

$$L_{\lambda} = M_L Q_{cal} + A_L \quad [5]$$

Where:

L_{λ} = Spectral radiance at the sensor's aperture [W/ (m2srµm)]

M_L = Band-specific multiplicative rescaling factor RADIANCE_MULT_BAND_x, where x is the band number.

A_L = Band-specific additive rescaling factor RADIANCE_MULT_BAND_x, where x is the band number.

Q_{cal} = Quantized calibrated pixel value [DN]

The conversion from L_λ back to at-sensor spectral reflectance ($L\lambda$) requires the following equation:

For Landsat 7 ETM +:

$$\rho_\lambda = \frac{\pi . L_\lambda . d^2}{ESUN_\lambda . \cos\theta} \quad [6]$$

Where:

ρ_λ = Planetary TOA reflectance [unitless]

π = Mathematical constant approximately equal to 3.14159 [unitless]

L_λ = Spectral radiance at the sensor's aperture [W/ (m^2srµm)]

d = Earth-Sun distance [astronomical units]

$ESUN_\lambda$ = Mean exo-atmospheric solar irradiance [W/ (m^2srµm)]

For Landsat 8 LDCM:

$$\rho_\lambda = M_\rho Q_{cal} + A_\rho \quad [7]$$

Where

ρ_λ = Planetary TOA reflectance [unitless]

M_ρ = Band-specific multiplicative rescaling factor REFLECTANCE_MULT_BAND_x, where x is the band number.

A_ρ = Band-specific additive rescaling factor REFLECTANCE_MULT_BAND_x, where x is the band number.

Q_{cal} = Quantized calibrated pixel value [DN]

TOA reflectance with a correction for the sun angle is then:

$$\rho_\lambda = \frac{\rho_\lambda '}{\cos(\theta_{SZ})} = \frac{\rho_\lambda '}{\sin(\theta_{SE})} \quad [8]$$

Where:

ρ_λ = Planetary TOA reflectance

θ_{SE} = Local sun elevation angle.

θ_{SZ} = Local solar zenith angle i.e. $\theta_{SZ} = 90^0 - \theta_{SE}$

Note: Most of the above parameters are found in the metadata file that accompanies each complete Landsat data. Hence, the radiometric calibration is an essential step for generating a high quality and consistent remote sensing data.

The Atmospheric Correction Module (which ensures accurate estimation of atmospheric effects) in ENVI classic offers two atmospheric correction modelling tools for retrieving spectral reflectance from multispectral radiance images e.g. Quick Atmospheric Correction (QUAC) and FLAASH. For the purpose of this analysis, the Quick Atmospheric Correction (QUAC) using ENVI 5.1 classic was carried out on the Landsat images creating a surface reflectance image, scaled into two-byte signed integers using a reflectance scale factor of 10,000. The procedure was also based on the condition that there are at least 10 diverse materials in a scene and also the presence of sufficient dark pixels in a scene to allow for a good estimation of the baseline spectrum (www.exelis.com/docs/quac.html).

Geometric correction involves the removal of geometric distortions or re-projection of the satellite image to its proper projection and coordinate system. The two Landsat images acquired for this project have been geometrically corrected using an image to image registration to ensure perfect co-registration between the Landsat 7 ETM+, 2003 and Landsat 8 LCDM, 2013 (Tsela et al., 2014). This procedure ensures identical coordinate system and minimizes spurious reflectance changes (Roy et al., 2002). At least 20 ground control points (GCPs) (Figure 3.6 and Figure 3.7) were selected uniformly throughout both Landsat 7 ETM+ and Landsat 8 LDCM images. Salient and distinctive features that remain unchanged over a period of time for example a lake, road crossing, water stream and a building edge were selected. Image-to-image registration was carried out using ENVI 5.0 Classic by selecting 20 ground control points (GCPs) using the most recent image (Landsat 8) as the base image due to its level of correction (L1T) and the previous (Landsat ETM+) as the warp image. Using the first order polynomial transformation technique, a total room mean square (RMS) error of 0.46 pixel associated with the GCPs was adopted. The RMSE obtained from

the geo-rectification process was considered sufficient as classes of interest from both images overlapped properly.

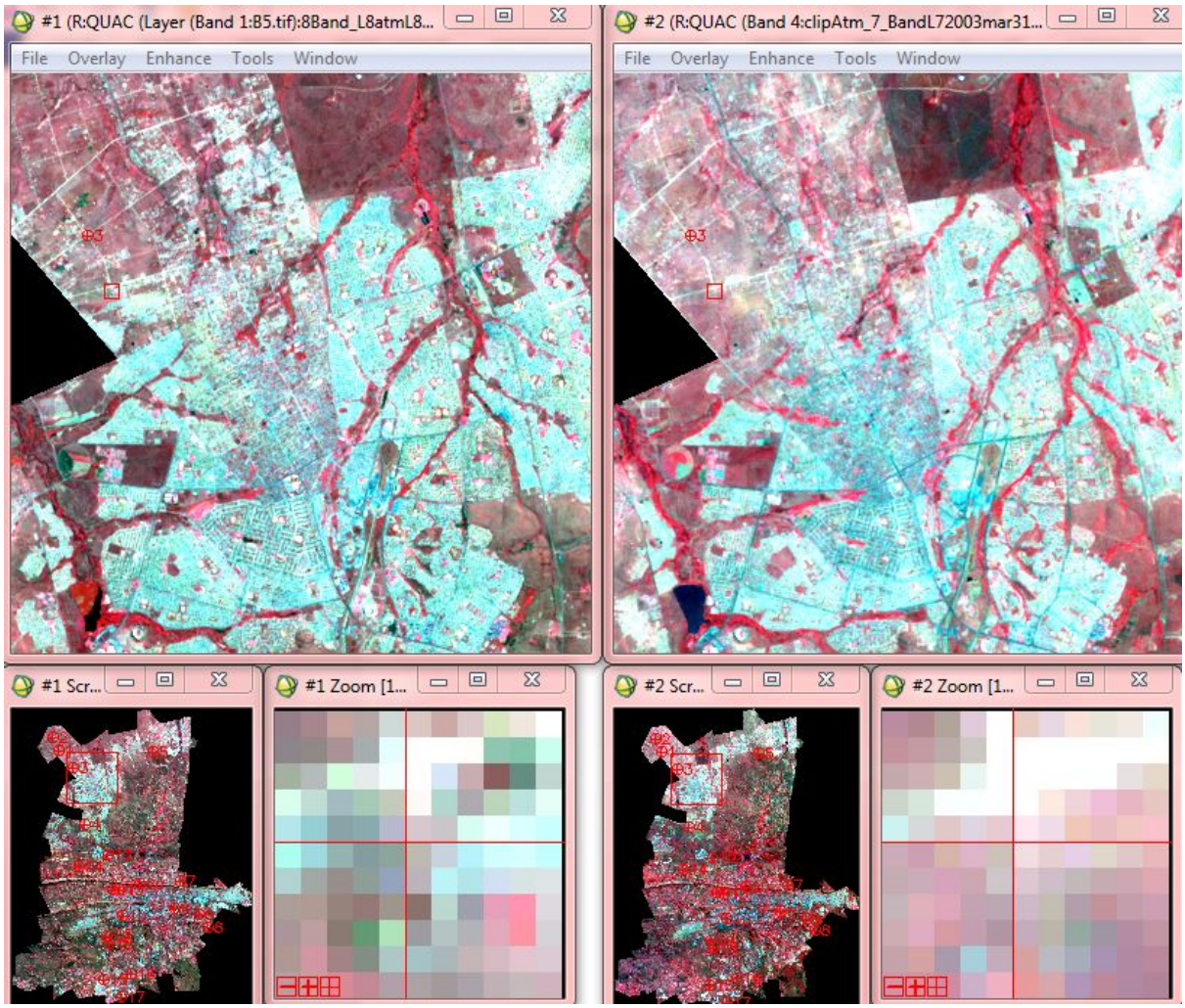

Figure 3.6: Dual display using Landsat 7 ETM + (31 March 2003) and Landsat 8 (13 November 2013) false colour images of Tshwane Metropolitan in ENVI software version 5.0 which simplified GCP collection for image to image registration.

Various studies on change detection as reported by Tsela et al. (2014), have proposed varying threshold values of acceptable root mean square (RMS) error for co-registration accuracy e.g. <0.5pixels (Jensen, 2005), <0.70 pixels (Wedderburn – Bishop, 2002), <0.5 pixels (Tsela et al., 2014) and so on. Generally, the total RMS error that is acceptable is <.0 pixel for all GCPs.

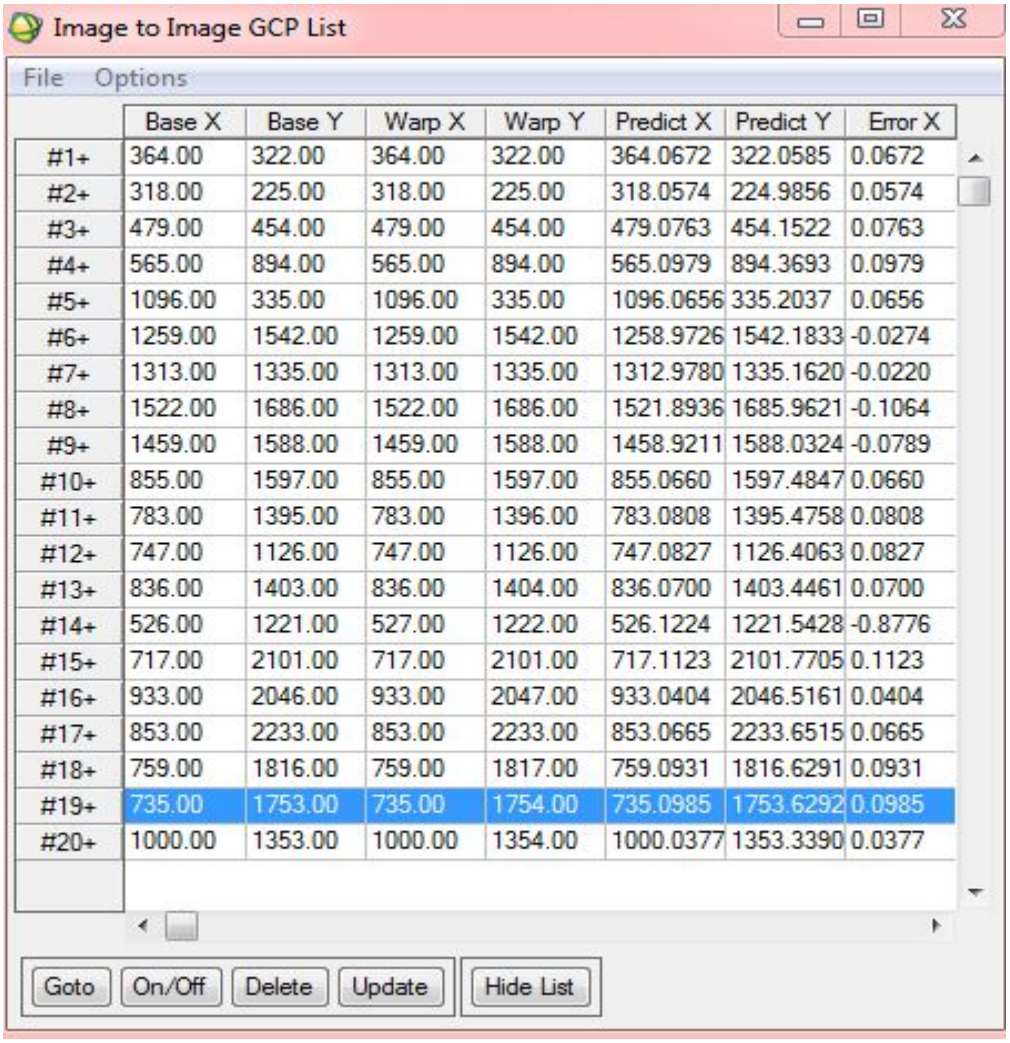

	Base X	Base Y	Warp X	Warp Y	Predict X	Predict Y	Error X
#1+	364.00	322.00	364.00	322.00	364.0672	322.0585	0.0672
#2+	318.00	225.00	318.00	225.00	318.0574	224.9856	0.0574
#3+	479.00	454.00	479.00	454.00	479.0763	454.1522	0.0763
#4+	565.00	894.00	565.00	894.00	565.0979	894.3693	0.0979
#5+	1096.00	335.00	1096.00	335.00	1096.0656	335.2037	0.0656
#6+	1259.00	1542.00	1259.00	1542.00	1258.9726	1542.1833	-0.0274
#7+	1313.00	1335.00	1313.00	1335.00	1312.9780	1335.1620	-0.0220
#8+	1522.00	1686.00	1522.00	1686.00	1521.8936	1685.9621	-0.1064
#9+	1459.00	1588.00	1459.00	1588.00	1458.9211	1588.0324	-0.0789
#10+	855.00	1597.00	855.00	1597.00	855.0660	1597.4847	0.0660
#11+	783.00	1395.00	783.00	1396.00	783.0808	1395.4758	0.0808
#12+	747.00	1126.00	747.00	1126.00	747.0827	1126.4063	0.0827
#13+	836.00	1403.00	836.00	1404.00	836.0700	1403.4461	0.0700
#14+	526.00	1221.00	527.00	1222.00	526.1224	1221.5428	-0.8776
#15+	717.00	2101.00	717.00	2101.00	717.1123	2101.7705	0.1123
#16+	933.00	2046.00	933.00	2047.00	933.0404	2046.5161	0.0404
#17+	853.00	2233.00	853.00	2233.00	853.0665	2233.6515	0.0665
#18+	759.00	1816.00	759.00	1817.00	759.0931	1816.6291	0.0931
#19+	735.00	1753.00	735.00	1754.00	735.0985	1753.6292	0.0985
#20+	1000.00	1353.00	1000.00	1354.00	1000.0377	1353.3390	0.0377

Figure 3.7: Illustration of the computed statistics in ENVI Classic for the 20 collected GCPs.

3.7 Image classification

Image classification involves assigning a land use or cover class to each pixel of the continuous raster image based on its spectral characteristics according to (Lu and Weng, 2007). This method is among the most useful methods of remote sensing image analysis, used for land use/cover mapping used for environmental and socio-economic applications. The main steps in image classification include: selection of an appropriate classification technique, finding proper training samples, selection of a class structure suitable for the current region and classification theme, post-classification together with accuracy assessment (Lu et al., 2011). There are two categories of classifiers namely the non-parametric and parametric classifiers. As a parametric classifier (e.g. maximum likelihood) it assumes that the statistical parameters generated from the training samples are representative samples as pointed out by Weng (2012). Nevertheless, the assumption of the normal spectral distribution is often violated, especially with complex urban landscapes. Lu and Weng (2007) also reported that non-representative or multimode distributed training data sets or regions of interest can further introduce uncertainty in the image classification process.

Earlier researchers have been able to show that this method provides a better result than parametric classifiers in complex urban landscapes (Paola and Schowengerdt, 1995). Some of the most frequently used non parametric classifiers are artificial neural network, decision tree classifier, support vector machine and classification and regression tree (CART) (Weng, 2012). Random Forests (RF) classifier is an ensemble algorithm developed in the field of machine learning that uses a similar but enhanced method of bagging (Walton, 2008). According to Loosvelt et al. (2012), RF classifier operates by creating a multiple classification and regression trees, each trained on a bootstrapped sample of the original training data. In this technique, the diversity of tree is increased by making them develop from different training data subsets created through bagging (Breiman, 1996). Ndyamboti (2013) also reported that each tree created, contributes a unit class vote, with the final classification determined among the tree range. For each of the new training sets that are created, two thirds (2/3) are part of the calibration subset, while a third (1/3) of the samples are randomly left out are known as the out-of-bag (OOB) samples (Chan and Paelinckx, 2008). Breiman (2001) pointed out that the proportion between the total number of OOB features and misclassifications contribute to unbiased assessment of generalization error (i.e., error converges as the number of trials increases). Compared to other non-parametric

classifiers, RF has a number of advantages which are: insensitive to noise as reported by Watts and Lawrence (2008), does not suffer from over-fitting or a long training time (Loosvelt et al., 2012), faster computation and ability to determine variable importance (Rodriguez-Galiano et al., 2012) and can handle unbalanced data sets (Watts et al., 2009).

RF classification involve creating a class image from regions of interest (ROI) selected from the two Landsat images in ENVI 5.0 Classic. This is followed by the parameterization to build a RF model which was used to classify the Landsat images. The parameterization involved the number of trees to be grown (*ntree*) which was selected up to 9-fold cross validation. This is followed by defining the number of randomly selected feature (*mtry*) which were used as default and a user defined value based on the number of bands to compute the best result. Likewise, the impurity in a node is determined using Gini Index and defining the minimum number of samples (i.e. Default = 1) and minimum impurity (i.e. Default = 0) in a node (Breiman, 2001). Based on the Landsat image number of bands, the value of *ntree* (i.e., number of trees) used ranged between 500 and 4500 while *mtry* was tested from 2 to 3 (i.e., number of features to create the RF parameters). In this study, we employed, ML classifier as a reference point for the RF classifiers.

3.8 Accuracy assessment and statistical significance of the classification results

Accuracy assessment is considered as an integral part of any image classification (Lillesand et al., 2008). It is a procedure used to indicate the quality of land use or cover (LULC) maps and their suitability for a particular purpose (Foody and Mathur, 2004). To determine the accuracy of the classification maps, a confusion matrix as designed by Congalton (1991) was built for each map and the Overall Accuracy (OA), User's Accuracy (UA), Producer's Accuracy (PA) and kappa coefficient were computed. Petropoulos et al. (2012) described OA as the number of pixels from the validation data set that have been correctly classified over the total number of pixels used for the accurate assessment expressed as a percentage. User's accuracy (UA) refers to the probability that a pixel belongs to a certain LULC class and the algorithm has labelled the pixel correctly into the same LULC class, while Producer's Accuracy (PA) shows the probability that the algorithm has properly allocated an image pixel (Petropoulos et al., 2012). The kappa variance as pointed out by Foody (2010) is the most commonly used measure of assessing the degree of agreement between the reference and validation data sets. Fan et al. (2007) asserted that kappa is a discrete multivariate technique

used in the accuracy assessment. The Kappa coefficient is calculated using the formula given by (Congalton, 1991):

$$K = \frac{N\sum_{i=1}^{r} X_{ii} - \sum_{i=1}^{r} X_{i+} \times X_{+i}}{N^2 - \sum_{i=1}^{r} (X_{i+} \times X_{+i})} \quad [9]$$

Where,

r = the number of rows in the error matrix

X_{ii} = the number of observations in row i column i(along the diagonal)

X_{i+} = is the marginal total of rowi(right of the matrix)

X_{+i} = the marginal total of column i (bottom of the matrix)

N = the total number of observations included in the matrix.

Kappa or KHAT values have also been categorized into three possible ranges (Congalton and Green, 2009):

Values greater than 0.80 (i.e., >80%) signifies strong agreement;

Values between 0.40 and 0.80 (i.e., 40-80) signifies moderate agreement;

Values below 0.40 (i.e., <40%) signifies poor agreement.

The sample variance of the kappa is computed using Delta method (Congalton and Green, 2009):

$$Var(\sigma^2) = \frac{1}{n}\left\{\frac{\theta_1(1-\theta_1)}{(1-\theta_2)^2} + \frac{2(1-\theta_1)(2\theta_1\theta_2-\theta_3)}{(1-\theta_2)^3} + \frac{(1-\theta_1)^2(\theta_4-4\theta_2^2)}{(1-\theta_2)^4}\right\} \quad [10]$$

Where,

Var (σ^2) = estimated variance

The test statistic for testing significance of a two error matrix is expressed by:

$$z = \frac{K_1 - K_2}{\sqrt{[\mathrm{Var}(\sigma^2)_1 - \mathrm{Var}(\sigma^2)_2]}} \quad [11]$$

Where,

K_1 = kappa statistics or coefficient for first error matrix

K_2 = kappa statistics or coefficient for second error matrix

Var $(\sigma^2)_1$ = estimated variance of the derived coefficient

Var $(\sigma^2)_2$ = estimated variance of the derived coefficient

Congalton and Green (2009) reported that if there is no difference between the two algorithms i.e., in a two-tail test, the null hypothesis Ho: (K_1 - K_2 = 0) is accepted, and the alternative H_1: (K_1 - $K_2 \neq 0$) is rejected, if Z < 1.96 at 5% level of significance. In this study, the ENVI 5.0 Classic software was used to create a region of interest and ground truth region of interest (reference ROIs) for land use or cover classification using RF classifier EnMAP-Box software and accuracy assessment. The software was also used to compute overall accuracy, producer accuracy, user's accuracy and kappa coefficient based on the error matrix for each classified image. The 2-sample z-test was used to show the statistical significance between the two kappa coefficients of the two classification algorithms.

3.9 Change detection analysis

Change detection is the process of identifying changes in the state of a feature or phenomenon by evaluating it at different periods (Singh, 1989). There are two groups of changes namely: Change between classes (i.e., conversion of land cover from one class to a completely different class) and change within classes (i.e., alteration of the condition of the landcover type within the same class) (Lu and Weng, 2004). Digital change detection procedures depends on image processing and change detection algorithms such as perpixel, subpixel and several other methods (Lu et al., 2011). However, in this study the post classification method which requires independently produced spectral classification results from each image of different years was used (Coppin et al., 2004, Ramoelo, 2007). The classified Landsat images of 2003 and 2013 were used for the post classification analysis. The class statistics algorithm in ENVI 5.1 Classic software was used to process the post classification. The proportion of each land cover change were derived and reported based on the percentage change of the study area (i.e., in percentage of all image pixels).

3.10 Deriving land surface temperature

3.10.1 Principles of Land Surface temperature extraction

Generally, materials naturally emit electromagnetic waves with a certain energy and spectral distribution, as long as the temperature is more than zero (273.15^0K). In addition, the intensity and spectral signature (radiant energy) of a particular feature depends on the material type and temperature. As reported by Maimaitiyiming et al. (2014), thermal infrared remote sensing employs space borne (orbital) or airborne (sub-orbital) sensors to gather and record the thermal infrared information of land surface features, which belongs to two atmospheric windows (3-5μm and 8-14μm). This allows the identification of land cover features and collection of surface parameters such as temperature, humidity, thermal inertia, etc. Thus, the thermal infrared radiation characteristics of the surface depend on the sun and earth (Levin, 2012).

Temperature variability across land features can be as a result of variations in their radiation energy budget. Therefore, we are allowed to use certain temperature to characterize and analyse the radiation energy of a particular type of land cover feature (Maimaitiyiming et al., 2014). The two basic thermal radiation law of land features or objects are; Stephen (Stefen)-Boltzmann and Kirchhoff's Law. Kirchhoff's law pointed that the ratio between the emitted energy (W) and the absorption rate (α) within per unit time and per unit area for numerous features at the same temperature is constant. The nature of the feature or object is independent of the ratio which is equal to the black body radiation energy W_B of the same area under the same temperature condition. Mathematical expression:

$$W/\alpha=W_B \quad [11]$$

$$\alpha = W/ W_B \quad [12]$$

$$\varepsilon=W/ W_{B,} \quad [13]$$

Therefore $\varepsilon=\alpha$ (i.e. absorption rate and emissivity of the feature or object is equal if it's doesn't absorb electromagnetic radiation). Stephen (Stefen)-Boltzmann law showed that the total radiant heat energy emitted from a surface is proportional to the fourth power of its absolute temperature. The law applies only to surfaces that absorb all incident heat radiation (blackbodies) and must be revised to be used for general objects. The thermal radiation

energy released by the feature or objects, according to Kirchhoff and Stephen (Stefen)-Boltzmann's law, equals to,

$$W=\alpha\sigma T^4 \quad [14]$$

Where α is the absorption rate

OR

$$W=\varepsilon\sigma T^4 \quad [15]$$

Where ε is the emission rate or emissivity.

From the above formula, the thermal radiation of features or objects generally are dependent on the fourth power of its absolute temperature and emission or absorption rate. A change in the feature or object temperature causes more change in its thermal radiation energy. Finally, the above explanation forms the theoretical basis for thermal infrared remote sensing.

3.10.2 Estimation of LST with Landsat Thermal Infrared Band

The thermal infrared (TIR) bands are generally useful for assessing the temperature difference between the city and its surrounding rural areas (i.e., UHI phenomenon). In previous works, there are several types of land surface temperature retrieval algorithms for Landsat TM/ETM+ images as summarized by Maimaitiyiming et al. (2014) i.e., these are radiation conduction equation method, mono-window algorithm and single-channel algorithm. The radiation, conduction equation method requires acquisition of data, such a real-time atmospheric profile which is rather difficult to acquire. On the other hand, parameters required for the mono-window algorithm are near surface temperature and atmospheric water content while atmospheric parameters required for single-channel algorithm is the moisture content of the atmosphere. For the purpose of this research, pre-determined land surface emissivity of the LULC types according to Mallick et al. (2008) were eventually used to derive the Land Surface Temperature (LST) image. This involves a number of steps in which some have been described in section 3.10.3 and 3.10.4 for converting the top of the atmosphere radiance of the thermal bands to brightness temperature and LST image.

3.10.3 Conversion to At-Satellite Brightness Temperature

For Landsat thermal bands, the conversion of DN to At-Satellite Brightness Temperature is given by (https://landsat.usgs.gov/Landsat8_Using_Product.php):

$$T_b = \frac{K_2}{\ln(K_1 / L_\lambda) + 1} \qquad [12]$$

Where,

K_1 = Band-specific thermal conversion constant (in watts/meter squared * ster * μm).

K_2 = Band-specific thermal conversion constant (in kelvin).

L_λ is the Spectral Radiance at the sensor's aperture, measured in watts/(meter squared * ster * μm).

Table 3.3: The K1 and K2 constant for Landsat sensors are provided in the image metadata file.

Constants	Landsat 7 ETM +	Landsat 8 LCDM
K_1 (watts/meter squared * ster * μm)	666.09	774.89
K2 (Kelvin)	1282.71	1321.08

3.10.4 Conversion from brightness temperature to Land Surface Temperature (LST)

After the image classification of the study area in Landsat 7 ETM+ and Landsat 8, the land surface emissivity values from literature of Mallick et al. (2008) were assigned to the land cover classes. Thereafter, the emissivity raster images for the two years were generated and used in the conversion of brightness temperature image to Land Surface Temperature (LST) using the equations below;

$$LST_{(\text{KELVIN})} = \frac{T_b}{1 + (\lambda + T_b / \rho) * \ln \varepsilon} \qquad [13]$$

To convert the LST image to Celsius image using the equation [14] below;

$$LST_{(CELSIUS)} = LST_{(KELVIN)} - 273.15 \quad [14]$$

Where,

λ is wavelength of radiance emitted in Landsat 7 ETM + (11.5μm) and Landsat 8 LCDM (10.8 μm). ρ= h.c/σ, σ = Stefan Boltzmann's constant (5.67x 10^{-8} Wm^{-2} k^{-4}), h = planks constant (6.626 X 10^{-34} Jsec), C = velocity of light, 2.998 x 10^{8}m/s) ε = spectral emissivity coefficient.

3.10.5 Surface Temperature Anomaly

Surface temperature anomaly can be defined as when the temperature conditions depart from long-term average conditions or reference value for a particular place at a given time of year. Positive anomaly indicates places with warmer temperature than the reference value e.g., urban and industrial hotspot. Negative anomaly indicates that the observed temperature was cooler than the reference value.

$$LST_{anomaly} = \frac{LST_{class}}{LST_{mean}} \quad [15]$$

Where,

LST_{class} = Individual mean LST for each land cover type.

LST_{mean} = Average of all the mean LST for all the land cover types.

4 CHAPTER FOUR: RESULT AND DISCUSSION

4.1 Introduction

This chapter presents spectral signatures of some urban land cover types (e.g., Grassland (GL), Bare land (BL), Plantation (PL), ISA such as concrete parking lot, road, Clay roofing and water (WA)) acquired from a wide-ranging and labour intensive field observation with the ASD and on screen selection of ROI. Also included are the results of image classification, classification accuracy assessment, statistical significance of classification, change detection, surface temperature retrieval and discussion.

4.2 Spectral signatures of some land cover types in Tshwane Metropolitan

Before the classification process, ground truthing using the ASD and GPS was carried out to ascertain the type of urban materials for roofing, buildings, roads, bare land or soil, water and vegetation (e.g., Tree plantation, grassland and cultivated lands) in the study area. The Figure 4.1(a-d) below shows the mean spectral reflectance of the land cover types collected at various places in the study area which can be broadly divided into impervious surfaces and non-impervious surface area. Note that the gaps in the graphs of each land cover type spectral signatures are noise such as shadow (SH) which were removed.

The spectral reflectance of non-impervious surface areas within the study area are displayed in Figure 4.1(a-d) which are primarily vegetation, bare land or soil and water bodies. The graph for grassland (e.g., parks and football fields) indicated its mean reflectance which increased from Red spectrum (743nm) to Near infrared (NIR) region (1001nm) while it starts to decrease in the (short wave infrared region) SWIR region due to the presence of ligno-cellulose bands. The grass spectrum also showed a noticeable chlorophyll absorption at 409 and 682nm with a green peak centre at 566nm and a vibrational water absorption was observed at 960, 1180, 1461 and 1972nm (Robert and Herold, 2004). The mean spectral signature of plantation (e.g., Eucaliptus trees) in the study area indicates a minimum reflectance experienced at green spectrum (563nm) and chlorophyll absorption at 416 and 677nm. The peak reflectance as expected was in the NIR region, which was at 894 and 1072nm together with vibrational water absorption detected in 976, 1217, 1467 and 1968nm (Nasarudin and Shafri, 2011). However, in the SWIR infrared region the reflectance decreased due to the presence of ligno-cellulose. The vegetation spectrum shows a similar

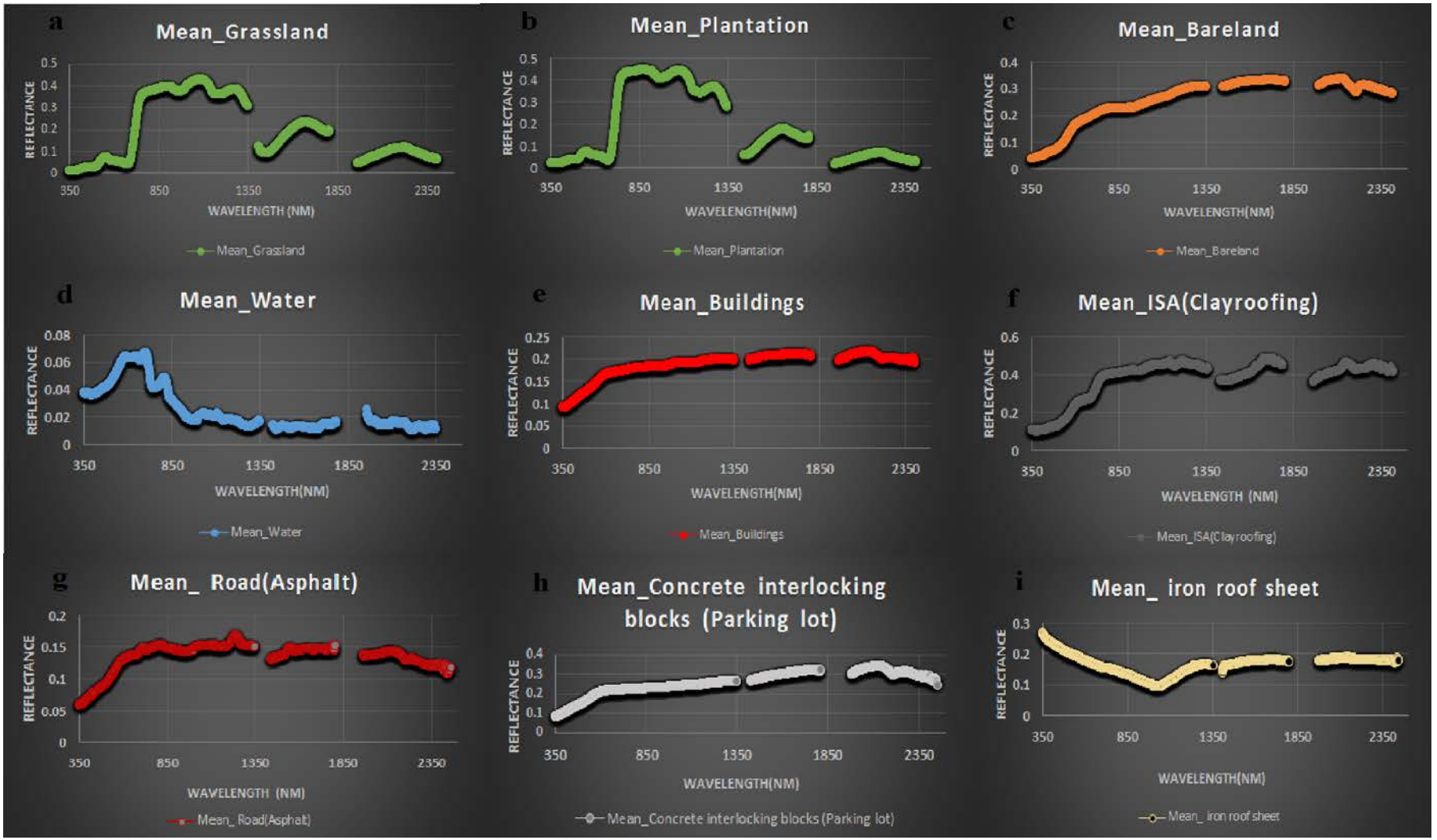

Figure 4.1: Field spectral signatures of LULC types considered for this study.

spectral feature when compared to the work of Robert and Herold (2004). According to the observations of Nasarudin and Shafri (2011), emittance and reflectance of bare land or soils is greatly influenced by their biochemical and physical components. Therefore the mean spectral reflectance of the bare lands or soil within the study area showed an increase in the reflectance from the visible regions of the SWIR spectrum (2073nm). Nasarudin and Shafri (2011) further indicated generally that slight absorptions due to features that appear to be contaminants, hence bareland or soil occurred at 2180nm.

The mean spectral characteristics of water bodies in the study area displays higher reflectance in the green spectrum (572nm) and a decrease at the SWIR region (1598nm) due to water absorption of light as reported by Xu (2006). The above can also be used to support the work of Xu (2006) who modified the water index (i.e., Modified Normalized water index) by using SWIR or MIR and Green region of the electromagnectic spectrum. This is because water experience a higher reflectance in the visible regions and absorption towards the SWIR regions and so he was able to suppress and remove built up, vegetation and soil nails. Furthermore, Figure 4.1(e-i) illustrates the representation of man-made or impervious surface areas observed within Tshwane Metropolitan which comprise of a building, road (asphalt and interlocking block areas) and roofing materials (clay and iron). The mean spectral reflectance of the buildings increased from the visible region in the SWIR region. Absorption at the visible bands may be due to the mixture of the original material and algae, but increase the reflectance at a longer wavelength with a reflectance peak in the SWIR region (2098nm). The mean reflectance of clay rooftops showed the lowest reflectance due to absorption in the visible region (378nm) as a result of liquid water and hydroxyl absorption (Heiden et al., 2001). The reflectance increases towards longer wavelengths with peak at SWIR (1663nm) due to loss of water in the production firing process according to the works of Nasarudin and Shafri (2011).

Asphaltic road has a mean spectral signature showing an increase in reflectance at the longest wavelength and reflectance peak in the Red region (1214nm) with absorption in SWIR region. Herold et al. (2004) also pointed out that the spectral signature of asphaltic roads is a result of crushed stones and various chemical components such as coal tar or oil and hydrocarbons. Similarly, concrete interlocking blocks has a reflectance peak in the SWIR region (2050nm) with a decrease in reflectance due to absorption at the visible regions near 550nm. According to the works of Robert and Herold (2004) the dust and dirt accumulating

on the concrete surfaces can decrease reflectance. The mean spectral signature of iron roofing exhibited a low reflectance at NIR (918nm) and higher reflectance at the visible bands attributing to the condition of the material used as surface colour for the iron roofing sheet.

4.3 Image classification

After the selection of regions of interest (ROI) from the Landsat images for the two years, the z-spectrum profile of the selected ROI was plotted in order to show how the land cover types mean spectral reflectance values are separable (i.e., to see the gaps between them). It was also used to know how representative they are for each land cover type (Figure 4.2 and Figure 4.3).

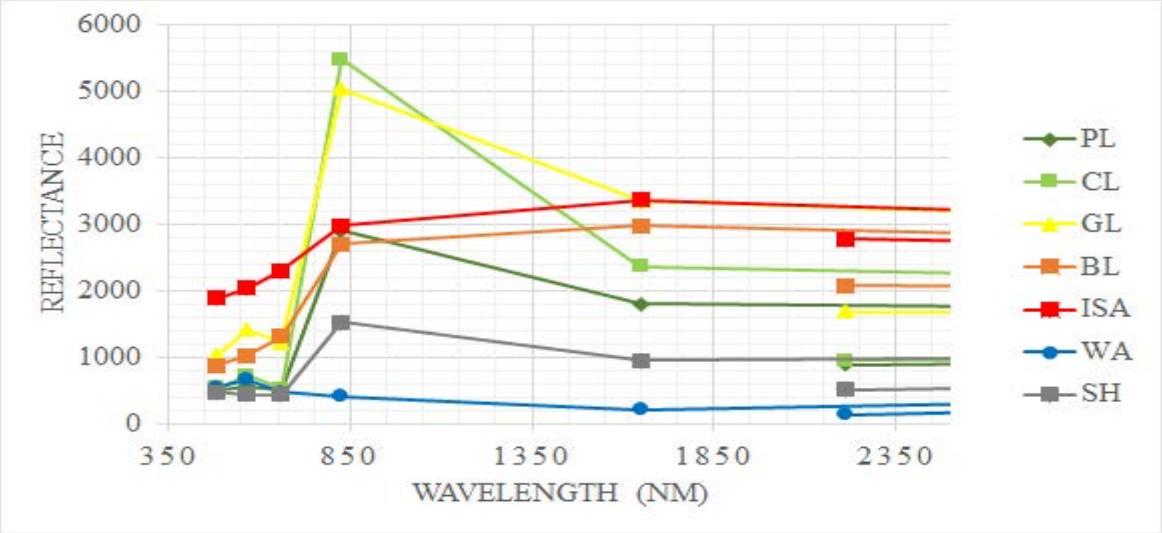

Figure 4.2: Landsat 7 ETM+ image spectrum of the study area.

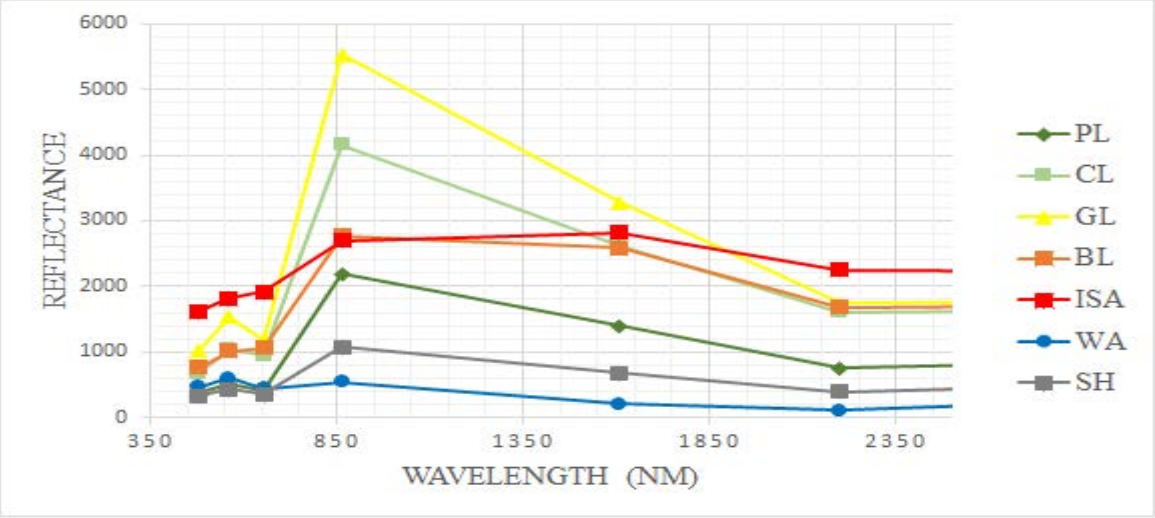

Figure 4.3: Landsat 8 LDCM image spectrum of the study area.

Figure 4.2 and Figure 4.3 shows the mean spectral profile for the ROIs selected from the two Landsat images. Vegetation (e.g. plantation, cultivated lands and grasslands) have reflectance peak in the NIR region (825nm), bare land or soil and impervious surfaces in the SWIR region (1650nm) and water at the green region (565nm) of the Z-spectra profile for the two Landsat data used for this study. When compared with the spectral signatures generated from the field, we can see that the regions of interest selected from the two Landsat images are representative enough to be utilized for the image land use or cover classification.

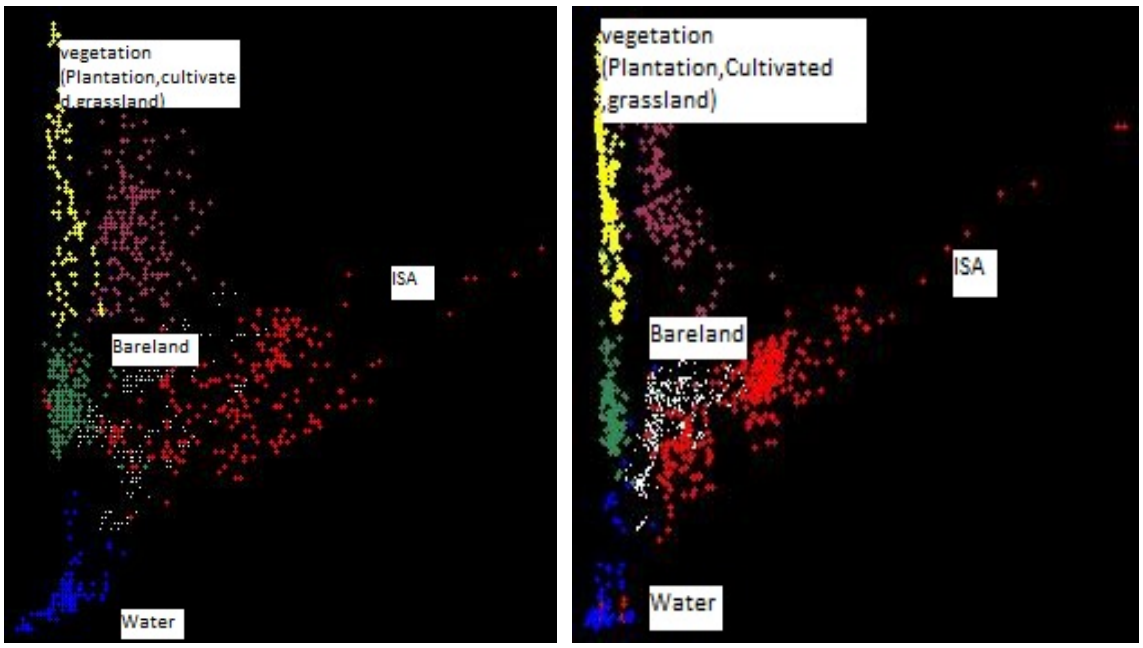

Figure 4.4: The 2-D Scatterplot of Red (x-axis) and NIR (y-axis) spectral space with the major LULC classes of Tshwane Metropolitan located at the three angle of the near-triangular space for Landsat 7 ETM + and Landsat 8 LCDM respectively.

The n-D Visualizer (i.e., feature space) was used to check the separability or degree of overlap of the land cover classes before using the region of interest (ROIs) as input into the supervised classification (Harmon, 2011). After the ROIs were exported to the n – D Visualizer together with the selected stacked Landsat images (VIS - SWIR), the Red and NIR bands were selected to observe the interaction of the classes in then D-space. After the above procedures, the Landsat 7 ETM + and Landsat 8 LDCM were classified using both the maximum likelihood (ML) classifiers and random forest (RF) classifiers with their map results shown in Figure 4.5 and Figure 4.6 respectively.

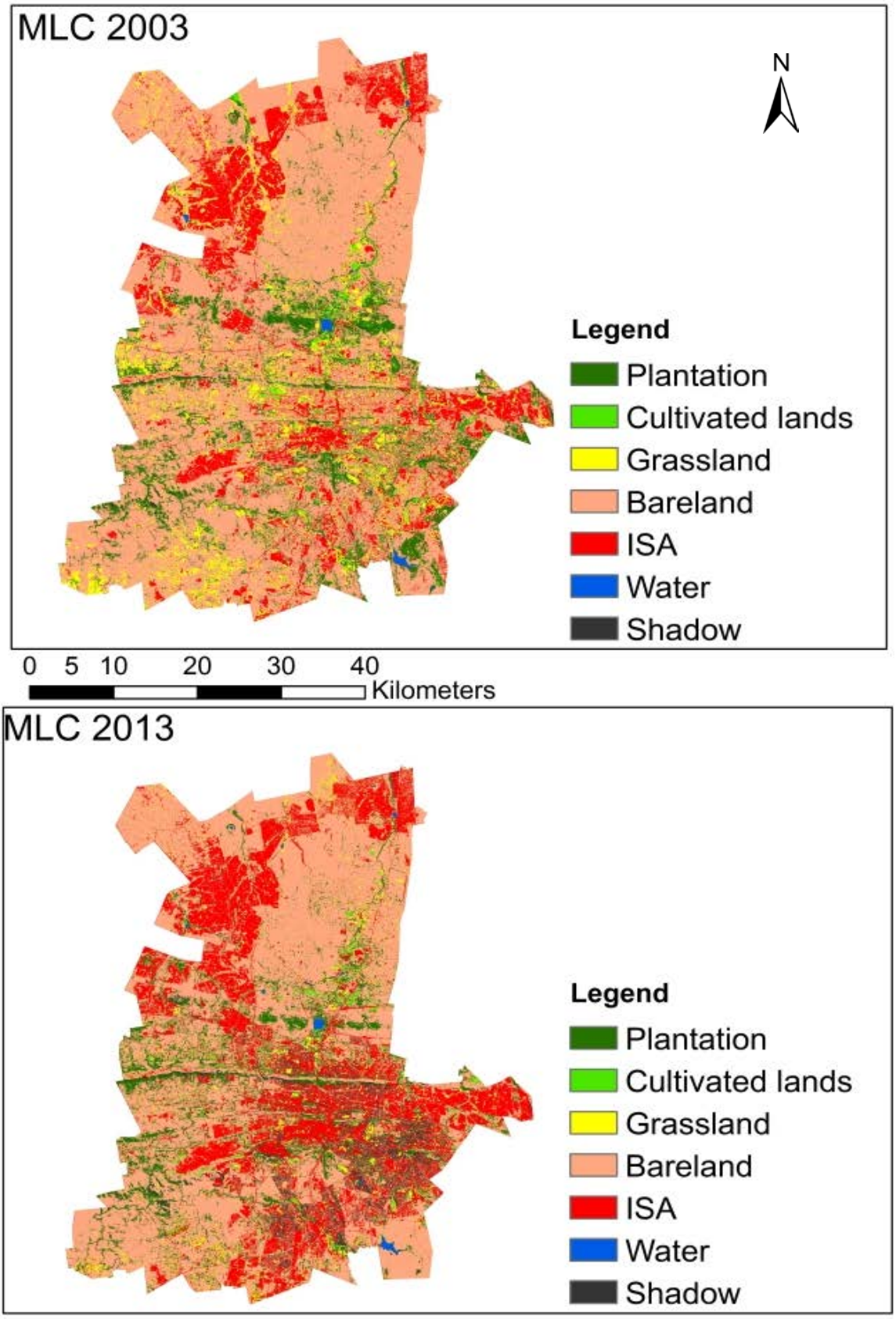

Figure 4.5: Classification maps generated by ML classifier using ENVI 5.0 image processing software of Landsat 7 ETM+ 2003-Mar-31 and Landsat 8 2013-Nov-13 respectively.

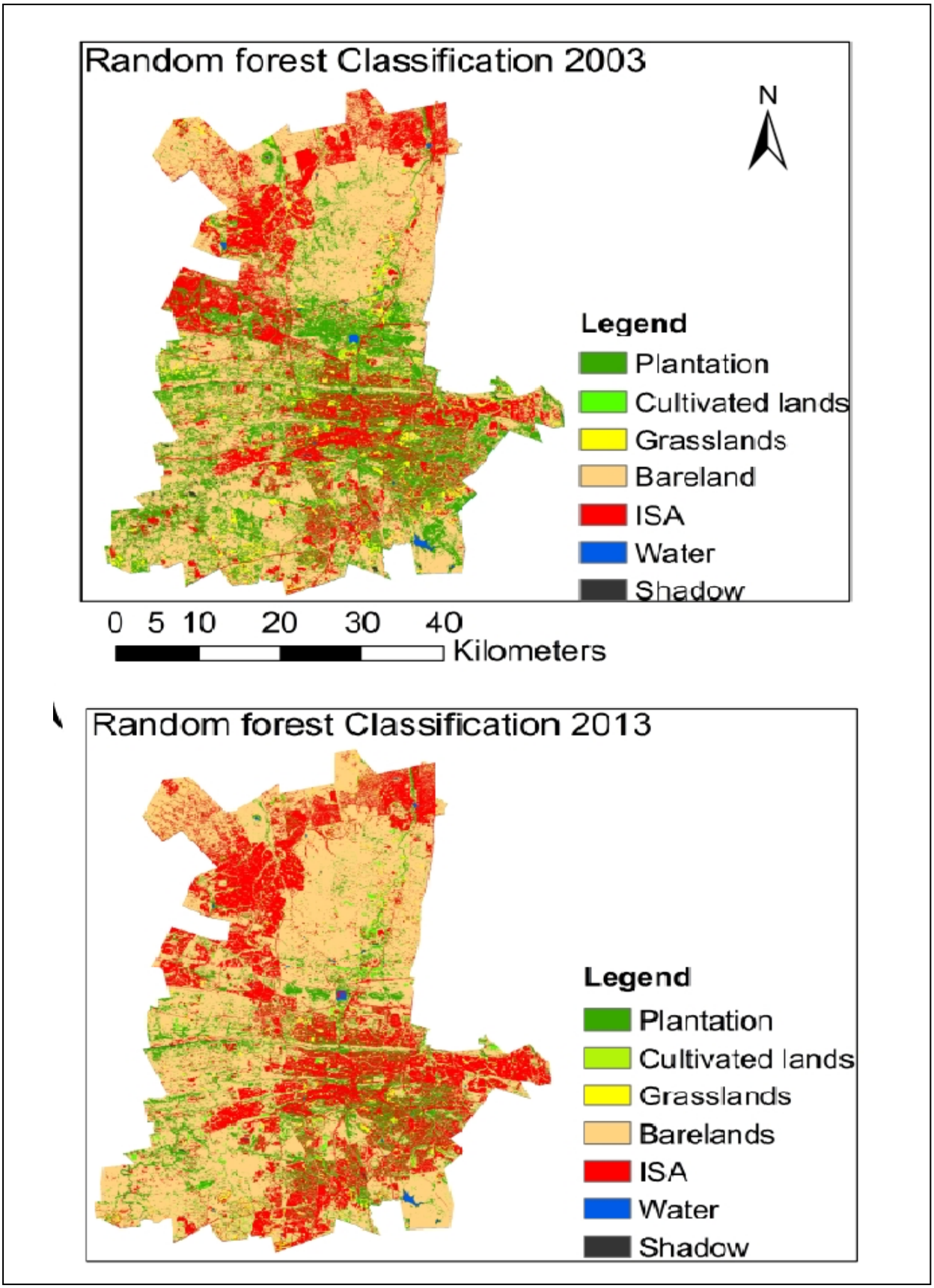

Figure 4.6: Classification maps generated by RF classifier using EnMap Box image RF software of Landsat 7 ETM+ 2003-Mar-31 and Landsat 8 2013-Nov-13 respectively.

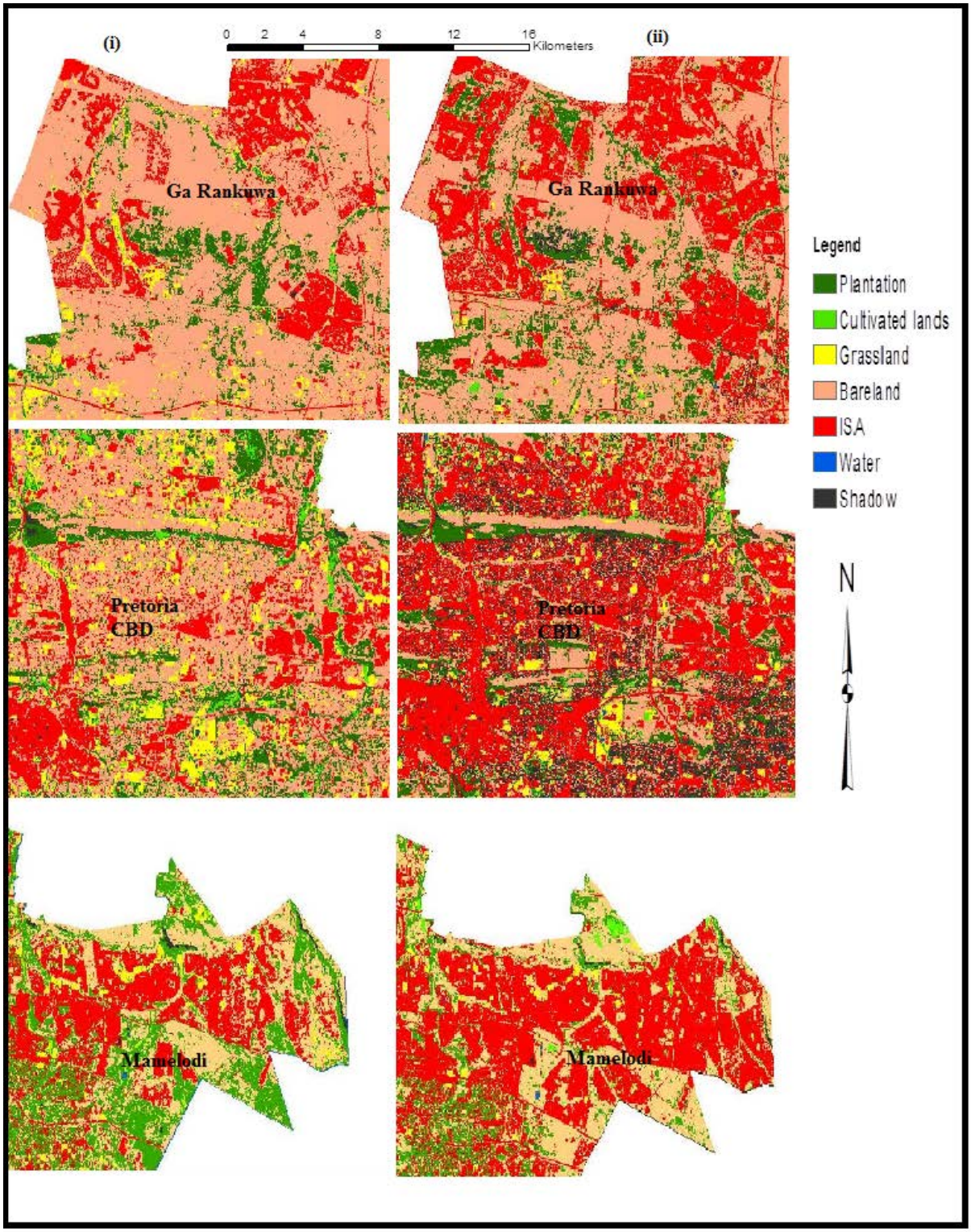

Figure 4.7: Maps showing some areas with changes in land use or cover for the study area between (i) 2003 and (ii) 2013.

4.4 Optimization of random forest parameters

The success of the RF classifier depends on the optimization of key parameters (ntree and mtry). The grid search method was used to optimize the RF classifier using a 9-fold cross validation. The concept behind the grid search technique is that different pairs of parameters are evaluated and the one yielding the highest level of accuracy is selected according to the works of Kavzoglu and Colkesen (2009). The OOB estimate of error was then used as a measure of assessing the prediction performance of the different parameter combinations. In terms of optimizing the RF parameters, the best model yielded an OOB error (11.18% and 17.97%) was produced by a combination of ntree and mtry values of 3500 and 2 respectively. The parameters were therefore selected to perform the final classification and generate the RF based classification map for 2003 and 2013 respectively.

4.5 Classification Accuracy Assessment Results

After the ground truth, ROIs were used to test MLC and RFC results from Landsat 7 ETM+ 2003 and they produced an overall accuracy of 88.63% and 88.82% respectively (Table 4.1 and Table 4.2).

Table 4.1: Confusion matrix of MLC parameters: Overall accuracy (OA), User accuracy (UA), Producer accuracy (PA) and Kappa Coefficient for Landsat 7 ETM + 2003-March-31.

Classes	**PL**	**CL**	**GL**	**BL**	**ISA**	**WA**	**SH**	**Row Total**	**UA (%)**
PL	163	0	0	7	0	0	0	170	**96**
CL	1	150	2	0	0	0	0	153	**98**
GL	0	3	189	0	0	0	0	192	**98**
BL	5	0	7	187	53	0	11	263	**71**
ISA	1	0	1	21	214	0	4	241	**88**
WA	0	0	0	0	0	93	4	97	**95**
SH	11	0	0	0	1	9	109	130	**83**
Column Total	**181**	**153**	**199**	**215**	**268**	**102**	**128**	**1246**	
PA (%)	**90**	**98**	**95**	**87**	**80**	**91**	**85**		
OA (%)	**88.63%**								
Kappa Coefficient	**0.8661**								

Table 4.2: Confusion matrix of RFC parameters: Overall accuracy (OA), User accuracy (UA), Producer accuracy (PA) and Kappa Coefficient for Landsat 7 ETM + 2003-March-31.

Classes	**PL**	**CL**	**GL**	**BL**	**ISA**	**WA**	**SH**	**Row Total**	**UA (%)**
PL	170	0	0	5	1	0	5	181	**82**
CL	1	152	0	0	0	0	0	153	**99**
GL	1	1	189	5	3	0	0	199	**100**
BL	23	0	0	148	43	0	1	215	**79**
ISA	2	0	0	25	239	0	0	266	**82**
WA	1	0	0	0	0	98	3	102	**98**
SH	9	0	0	3	5	2	108	127	**92**
Column Total	**207**	**153**	**189**	**186**	**291**	**100**	**117**	**1243**	
PA (%)	**93**	**99**	**94**	**68**	**89**	**96**	**85**		
OA (%)		**88.82**							
Kappa Coefficient		**0.87**							

Table 4.3: MLC and RFC parameters: User accuracy (UA),Commission error (CE), Producer accuracy (PA) and Omission error (OE) for Landsat 7 ETM + 2003-March-31.

	MLC_UA %	RF_UA %	MLC_CE %	RF_CE %	MLC_PA %	RF_PA %	MLC_OE %	RF_OE %
PL	96	82	4	18	90	93	10	7
CL	98	99	2	1	98	99	2	1
GL	98	100	2	0	95	94	5	6
BL	71	79	29	21	87	68	13	32
ISA	89	82	11	18	80	89	20	11
WA	96	98	4	2	91	96	9	4
SH	84	92	16	8	85	85	15	15

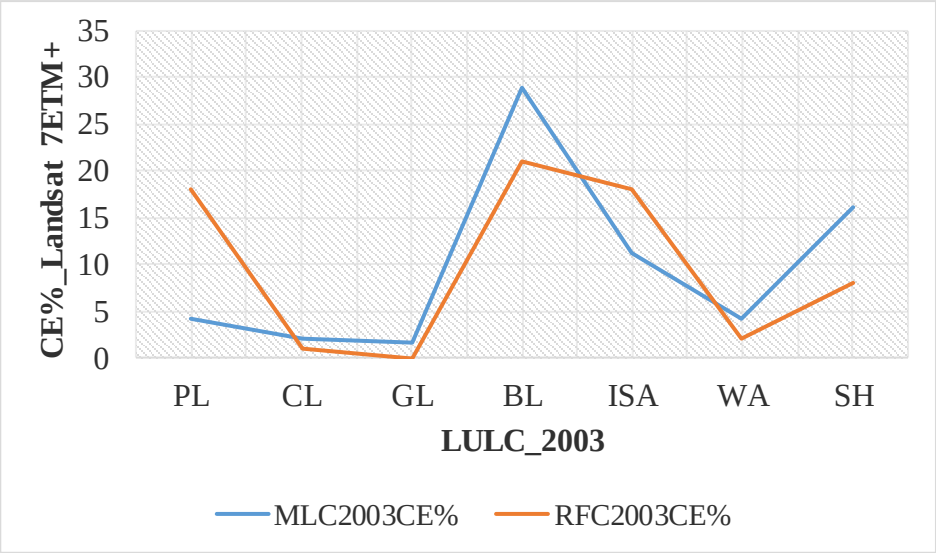

Figure 4.8: Comparison of CE in the MLC and RFC methods across the seven LULC classes derived for the 2003 Landsat 7 ETM+ data.

For the 2003 Landsat-derived LULC classes, both ML and RF classification exhibited the lowest CE (Table 4.3) i.e., below 5% in the CL, GL and WA relative to the other classes similar to the MLC method in the PL class (Figure 4.8). This suggests that the MLC showed good detection in the above mentioned classes in the 2003 data set. Also, both MLC and RFC had a highest CE particularly in the BL class (21-29%), ISA (12-18%) and SH (8-16%) whereas RFC showed a CE of 18% in PL. Overall results shows that both ML and RF classifiers produced minimal false classification in CL, GL and WA classes (Figure 4.8). Though both classifiers showed a high CE% in BL, ISA and SH classes, a disagreement between the two classifiers was obervered in PL class; the ML is the better classifier (CE <5%) compared to RF classifier. In addition, the ground truth ROIs were also used to test MLC and RFC results from Landsat 8 LCDM 2013 and they produced an overall accuracy of 80.13% and 82.03% respectively (Table 4.4 and Table 4.5).

Table 4.4:Confusion matrix of MLC parameters: Overall accuracy (OA), User accuracy (UA), Producer accuracy (PA) and Kappa Coefficient for Landsat 8 LCDM 2013-Nov-13.

Classes	**PL**	**CL**	**GL**	**BL**	**ISA**	**WA**	**SH**	**Row Total**	**UA (%)**
PL	156	10	1	2	0	0	9	178	**88**
CL	2	79	12	12	0	0	0	105	**75**
GL	0	43	149	1	0	0	1	194	**76**
BL	11	47	10	255	23	0	0	346	**74**
ISA	0	9	5	14	201	4	2	235	**86**
WA	0	0	0	0	0	178	16	194	**92**
SH	14	4	2	3	0	8	51	82	**62**
Column Total	183	192	179	287	224	190	79	1334	
PA (%)	**85**	**41**	**83**	**89**	**90**	**94**	**65**		
OA(%)		**80.13**							
Kappa Coefficient		**0.7638**							

Table 4.5: Confusion matrix of RFC parameters: Overall accuracy (OA), User accuracy (UA), Producer accuracy (PA) and Kappa Coefficient for Landsat 8 LCDM 2013-Nov-13.

Classes	PL	CL	GL	BL	ISA	WA	SH	Row Total	UA (%)
PL	175	0	0	5	0	0	3	183	**72**
CL	30	97	11	41	13	0	0	192	**70**
GL	3	1	158	13	4	0	0	179	**92**
BL	10	37	1	231	5	0	0	284	**75**
ISA	1	2	0	17	204	0	0	224	**88**
WA	6	0	0	1	4	170	9	190	**96**
SH	15	0	0	0	0	7	56	78	**82**
Column Total	**240**	**137**	**170**	**308**	**230**	**177**	**68**	**1330**	
PA (%)	**95**	**50**	**88**	**81**	**91**	**89**	**71**		
OA (%)		**82.03**							
Kappa Coefficient		**0.79**							

Table 4.6: MLC and RFC parameters: User accuracy (UA),Commission error (CE), Producer accuracy (PA) and Omission error (OE) for Landsat 8 LCDM 2013-Nov-13.

	MLC_UA %	RF_UA %	MLC_CE %	RF_CE %	MLC_PA %	RF_PA %	MLC_OE %	RF_OE %
PL	88	72	12	28	85	95	15	5
CL	75	70	25	30	41	50	59	50
GL	77	92	23	8	83	88	17	12
BL	74	75	26	25	89	81	11	19
ISA	86	88	14	12	90	91	10	9
WA	92	96	8	4	94	89	6	11
SH	62	82	38	18	65	71	35	29

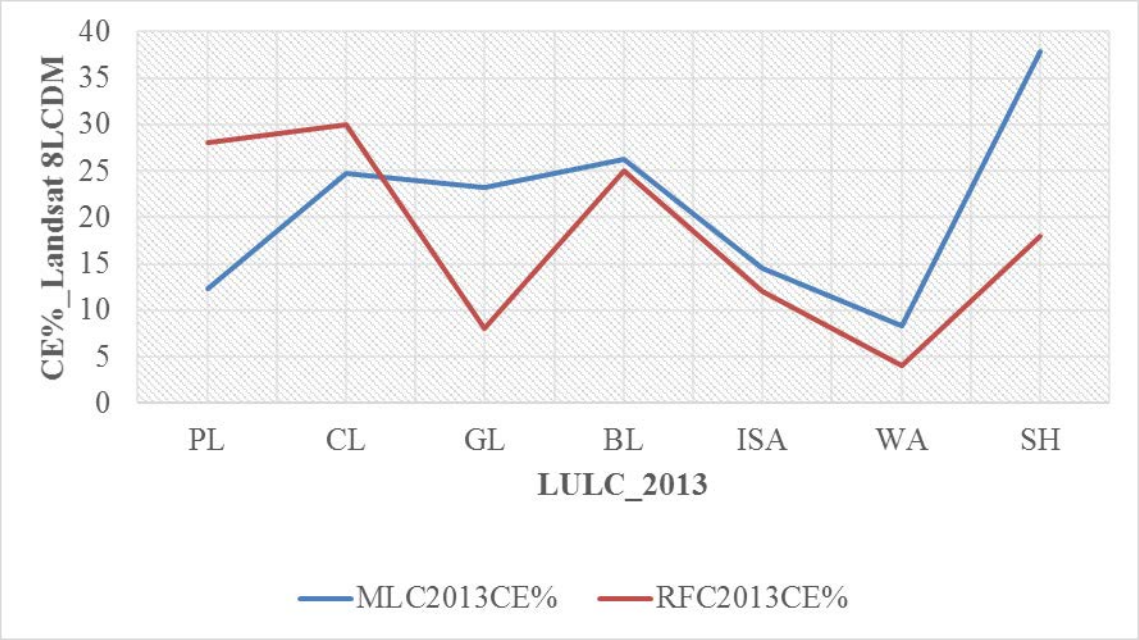

Figure 4.9: Comparison of CE in the MLC and RFC methods across the seven LULC classes derived for the 2013 Landsat 8LCDM data.

Further, for the 2013 Landsat-derived LULC classes, the CE by both methods was generally higher in contrast to the 2003 Landsat data classes (Table 4.6). In particular, the MLC algorithm had the highest CE of 26% and 38% corresponding to the BL and SH classes, followed by the RF method with CE of 28% and 30% corresponding to the PL and CL classes respectively (Figure 4.9). Nonetheless, the RF and ML algorithm had a better detection in the WA class with CE of 4% and 8% (i.e., CE <10%) and this is comparable to the RFC for the GL class and a slightly low CE of 12-15% in ISA class. In general, the results shown in Figure 4.9, demonstrates that both ML and RF classifiers produced minimal false classification in WA and ISA class in comparison to other classes. The disagreement between the two classifiers occurred in GL class with RF as the better classifier (CE <10%) than ML classifier.

4.6 Statistical significance of classification results

In this study, pairwise comparison of error matrix by use of the kappa coefficient was used to test for statistical significance and equality in the classification results of the two algorithms (Congalton and Green, 2009). The Landsat 7 ETM + 2003-March-31 image has an O.A. of 88.63% and kappa coefficient of 0.866 based on the MLC. The confident interval for MLC is 0.8471 - 0.8849 with the kappa coefficient falling within the interval. The RF classifier has an O.A of 88.82% and kappa coefficient of 0.87. The confident interval for the RF is 0.8513 - 0.8887 with the kappa coefficient falling within the interval. The 2-sample Z-test was used to compare the two errox matrices. The Z-value of 0.3 and p-value of 0.7682 were estimated for the two-tailed comparison at 5% significant level. Since Z-value is less than $Z_{\alpha/2}$ (i.e., z-value <1.96) and p-value >0.05, this implies that there is little evidence against the Null hypothesis H_o : (K_1-K_2 = 0) i.e., the H_o is not rejected. It can therefore be concluded that both classifiers produced similar classification errors across the CL,GL,BL,ISA, WA and SH classes. In contrast, the ML is a better classifier than RF classifier in the PL class.

For Landsat 8 LCDM, 2013 image, an O.A. of 80.13% and kappa coefficient of 0.76 was obtained based on the MLC. The confident interval for the MLC is 0.731 - 0.783 with kappa coefficient falling within the interval. On the other hand,the RF classifier produced an O.A of 82.03% and kappa coefficient of 0.79. The confidence interval for the RF classifier is 0.7681 - 0.8119 with the kappa coefficient falling within the confidence interval. The 2-sample Z-test was used to compare the two errox matrix. The z-value of 1.90 and p-value of 0.063 were estimated for the two-tailed comparisons at 5% significant level. The z-value is less than $Z_{\alpha/2}$ (i.e., z-vlaue <1.96) and p-value >0.05, suggesting that there is little evidence against the Null hypothesis Ho: (K_1-K_2 = 0) i.e., the Ho is not rejected. Therefore either of the classifiers can be selected to classify Landsat 8 LDCM, since they produce similar classification errors in PL, CL, BL, ISA, WA and SH except for the inherent difference of MLC and RFC results of the GL class.

4.7 Post-Classification Change Detection

The summary of the change between classes (i.e., conversion of land cover from one class to a completely different class) are given in Table 4.8 and Table 4.8. Results in Table 4.7 indicate that LULC changes (i.e., “from-to” information) have occurred between 2003 and 2013 when ML classifier is used. Almost half of PL (46%) was changed to BL class and one third (34%) of the pixel classified as PL in 2003 image do have the same class membership in

2013. For class CL, more than one fourth was assigned to PL, one third to BL and 11.58% of the pixels of CL did not change in 2013. About 13.04% of GL class was unchanged 2013 while half of the class change to BL class (53.3%). Likewise, more than half of the pixels for BL class (69.73%), ISA class (96.46%) and WA class (79.64%) remained were unchanged in 2013. For SH class, (30%) or one third of the pixel remained and almost half were attributed to PL class (42.7%).

Table 4.7:Change detection Statistics for MLC Landsat 7 ETM+ 2003 and Landsat 8 LCDM, 2013

Percentage change

		INITIAL STAGE 2003									
		Unclassified	**PL**	**CL**	**GL**	**BL**	**ISA**	**WA**	**SH**	**row total**	**Class total**
FINAL STAGE 2013	**Unclassified**	**0**	0	0	0	0	0	0	0	0	0
	PL	0	**34.04**	28.02	7.69	4.91	0.10	1.96	42.70	100	100
	CL	0	2.60	**11.58**	6.99	2.46	0.20	4.58	1.30	100	100
	GL	0	0.70	4.07	**13.035**	2.09	0.17	0.73	0.26	100	100
	BL	0	46.17	39.69	53.29	**69.73**	2.69	0.88	11.12	100	100
	ISA	0	7.40	5.43	12.25	16.25	**96.46**	1.78	8.77	100	100
	WA	0	0.13	0.29	0.03	0.02	0.01	**79.64**	5.70	100	100
	SH	0	8.96	10.92	6.71	4.55	0.36	10.43	**30.14**	100	100
	Class total	0	100	100	100	100	100	100	100		
	Class change	0	65.69	88.42	86.96	30.27	3.54	20.36	69.86		
	Image Difference	0	-26.50	72.34	-66.26	-10.41	9.83	12.25	967.35		

List: PL (Plantation), CL (Cultivated lands), GL (Grass land), BL (Bare land), ISA (impervious surface area), WA (water) and SH (Shadow).

Table 4.8:Change detection Statistics for RFC Landsat 7 ETM+ 2003 and Landsat 8 LCDM, 2013

Percentage change

		INITIAL STAGE 2003									
		Unclassified	**PL**	**CL**	**GL**	**BL**	**ISA**	**WA**	**SH**	**row total**	**Class total**
	Unclassified	**0**	0	0	0	0	0	0	0	0	0
FINAL STAGE 2013	**PL**	0	**26.95**	35.36	9.36	5.52	5.90	0.06	49.87	100	100
	CL	0	1.83	**13.95**	8.30	2.56	1.46	0.01	0.94	100	100
	GL	0	0.70	4.66	**21.35**	1.671	1.06	0.00	0.43	100	100
	BL	0	53.90	39.24	43.69	**73.11**	23.061	0.10	18.56	100	100
	ISA	0	16.03	6.39	17.08	16.85	**68.07**	0.09	7.00	100	100
	WA	0	0.09	0.08	0.05	0.02	0.07	**0.21**	4.55	100	100
	SH	0	0.50	0.31	0.17	0.28	0.37	99.54	**18.64**	100	100
	Class total	100	100	100	100	100	100	100	100		
	Class change	0	73.05	86.04	78.65	26.89	31.93	99.79	81.35		
	Image Difference	0	-53.06	245.21	-41.03	14.82	23.69	-99.70	18577.5		

List: PL (Plantation), CL (Cultivated lands), GL (Grass land), BL (Bare land), ISA (impervious surface area), WA (water) and SH (Shadow).

Table 4.8 summarises the LULC changes (i.e., “from-to” information) have occurred between 2003 and 2013 when random forest is used. Half of PL class (53.9%) were converted to BL while more than one fourth of PL class (26.95%) pixels remained in the same class membership in 2013. Even though 13.96% of CL class remained the same, more than one third of the class pixels were assigned to PL class (35.4%) and BL class (39.2%). Nearly half of GL class shifted to BL class (44%) with 21% of GL pixels remaining unchanged. For BL class, 73% of the pixels classified remained in the same class membership in 2013. Also, one fourth of ISA class transformed to BL class (23.1%) and 68.1% remained unchanged. The WA class (0.2%) had very minimal transformation while SH class experienced a large change with half of the (49.8%) pixels assigned to PL class and 18.8% remaining unchanged in 2013.

4.8 Maximum Likelihood and Random Forest Change Detection Comparison

The quantification of the LULC change between the two years in terms of percentage were based on the use of ML and RF classifier.

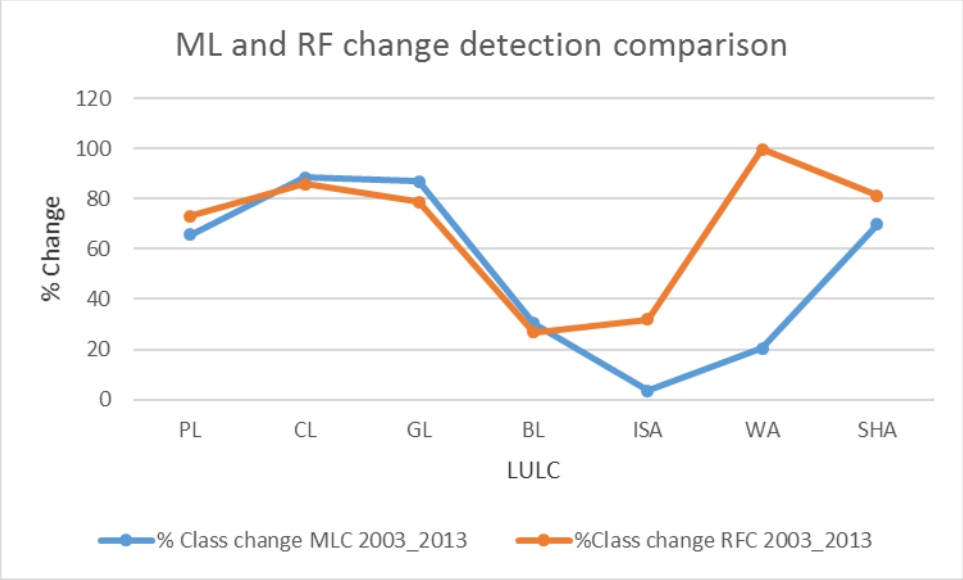

Figure 4.10: Land cover changes between 2003 - 2013 using MLC and RFC.

.

Based on results presented in Figure 4.10, it is clear that using the aforementioned classification methods, various LULC changes are observed. Figure 4.10 indicates an overall change of 66% (ML) and 73% (RF) in PL and 88% (ML) and 66% (RF) in CL. In addition, both the ML and RF classifications showed 87% and 79% for GL respectively. BL depicts an overall change of 30% (ML) and 26% (RF) which can be attributed to lots of open lands or soil. Due to urban sprawl (i.e., construction of more buildings and paved and asphaltic roads), ISA shows an overall change of 4% (ML) and 32% (RF). WA also experiences change of 20% (ML) and 99% (RF) mainly due to seasonal variations or climate change within the ten years period. Shadow (SH) has changed by 70% (ML) and 81% (RF) due to increase in the tall building in the Central Business District (CBD). From Figure 4.10 it could be concluded that using the two classifiers similar change detection results are observed in PL, CL, GL and BL. RF classifier indicates a better change detection in ISA and WA as compared to the ML

classifier. Such improvements maybe attributed to the fact that the RF classifier is almost insensitivity to noise (Watts and Lawrence, 2008), does not suffer from over-fitting or a long training time (Loosvelt et al., 2012), and it has the ability to handle unbalanced data sets (Watts et al., 2009).

4.9 Land surface temperature retrieval

The thermal band of Landsat images also provides not only a measure of the magnitude of land surface temperature, but also gives the spatial extent of the UHI effect of the entire study area. Based on LULC classification results derived from Landsat ETM+ 2003 and Landsat 8 LCDM 2013, corresponding emissivity images in Figure 4.11 were derived by assigning emissivity values to each LULC according to works of Mallick et al. (2008) using the reclassify algorithm in ArcGIS 10.1 (i.e., changing the values in the raster). The zonal statistics by table in ArcGIS 10.1 was used to derive the LULC – LST map. In Figure 4.11, the thermal variance across the study area (Tshwane metropolitan) are shown.

Both Landsat 7 ETM+ (2003) and Landsat 8 LCDM (2013) LST map Figure 4.12 had a surface temperature range of 21.21^{O}C – 40.81^{O}C and 22.98 – 40.92^{O}C. The histogram in Figure 4.13 showed the pixel estimated mean surface temperature values across the different land use or cover classes used for this study for 2003 and 2013 Landsat images. As observed from Figure 4.13, Plantation (i.e., tree plantation) mean LST range from 24.91^{O}C to 29.49^{O}C. Also cultivated lands and grasslands showed a mean LST range for both years from 23.42^{O}C to 30.31^{O} C and 25.89^{O} C to 30.42^{O} C respectively. Increase in LST as expected was found for bare land and impervious surface areas with LST pixels ranging from 26.88^{O}C to 30.87^{O}C and 27.77^{O}C to 31.91^{O}C respectively. Water bodies (e.g., rivers) and shadow also exhibited mean LST pixel values ranging from 23.57^{O}C to 24.25^{O}C and 20.82^{O}C to 21.98^{O}C which were lower values when compared with that of other land cover types.

Furthermore, the mean near surface temperature from the weather stations (South African Weather Stations, SAWS and Pretoria Botanical Institute) was used as a point of reference to verify the accuracy of the final retrieved LST images for 2003 and 2013. From Landsat 7 ETM+, the mean pixel temperature for Pretoria Eendracht and Irene Wo weather stations were 26.28^{O}C and 26.77^{O}C while the mean near surface air temperature from SAWS is 29.60^{O}C and 27.80^{O}C. Hence, the LST retrieval error was 3.3^{O}C and 1^{O}C respectively. Similarly, Landsat 8 LCDM data was also tested to know the accuracy of the retrieved LST.

In this case the mean pixel temperature for the Pretoria UNISA weather station and Pretoria National Botanical Institute of 27.218^{O} C and 28.63^{O} C was compared with the mean near surface temperature of 27.6^{O}C and 29.91^{O}C respectively. Thus, the LST retrieval error was 0.38^{O}C and 1.3^{O}C for the two stations. Therefore, the thermal bands of Landsat 7 ETM + and Landsat 8 LCDM data employed for this study provided a good result and can be used for further temperature variability analysis.

Figure 4.14 shows the LST anomaly between 2003 – 2013. Places that were warmer than average are red, near normal are yellow and those cooler than average are green. For the LST derived maps for 2003 and 2013 (see Equation 15), both bare lands and ISA which are hot spots showed a warmer LST anomaly of 1.07^{0}C to 1.08^{0}C and 1.11^{0} C to 1.12^{0} C respectively. Plantation (1.02^{0}C - 1.04^{0}C), cultivated lands (0.96 - 1.06^{0}C), grassland (1.06^{0}C - 1.07^{0}C), water (0.96^{0}C - 0.85^{0}C) and shadow (0.83^{0}C - 0.77^{0}C) indicated cooler anomaly. Based on the results from this study, it could be deduced that persistent warm anomaly over the years is due to ISA increase in area extent. Thus, increase in ISA influences surface energy exchange, micro to meso scale climate and other environmental processes which can be used to determine the strength of UHI and monitor the global climate.

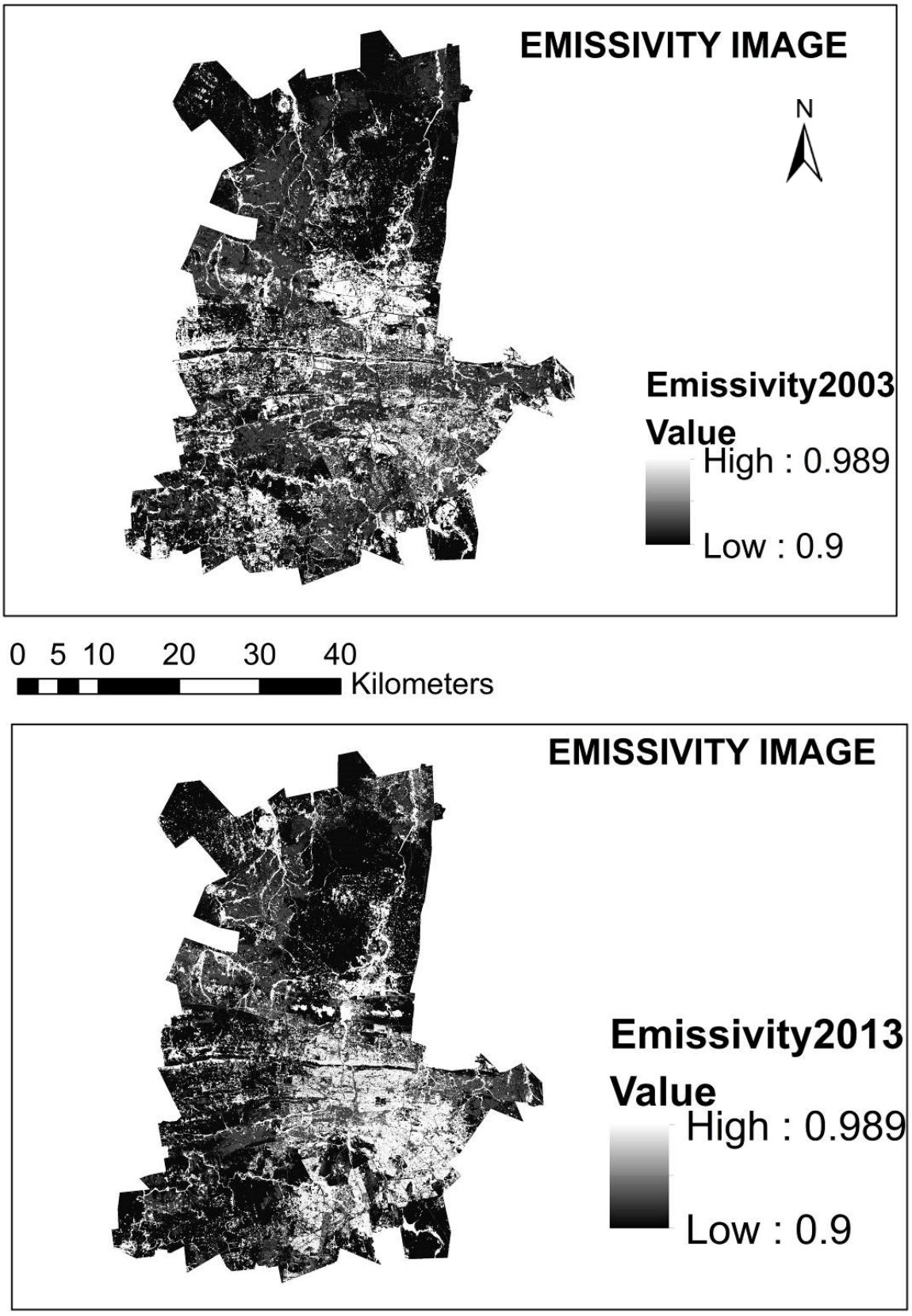

Figure 4.11: Land surface emissivity (LSE) image of the study area for Landsat 7 ETM+ 2003-Mar-31 and Landsat 8 2013-Nov-13.

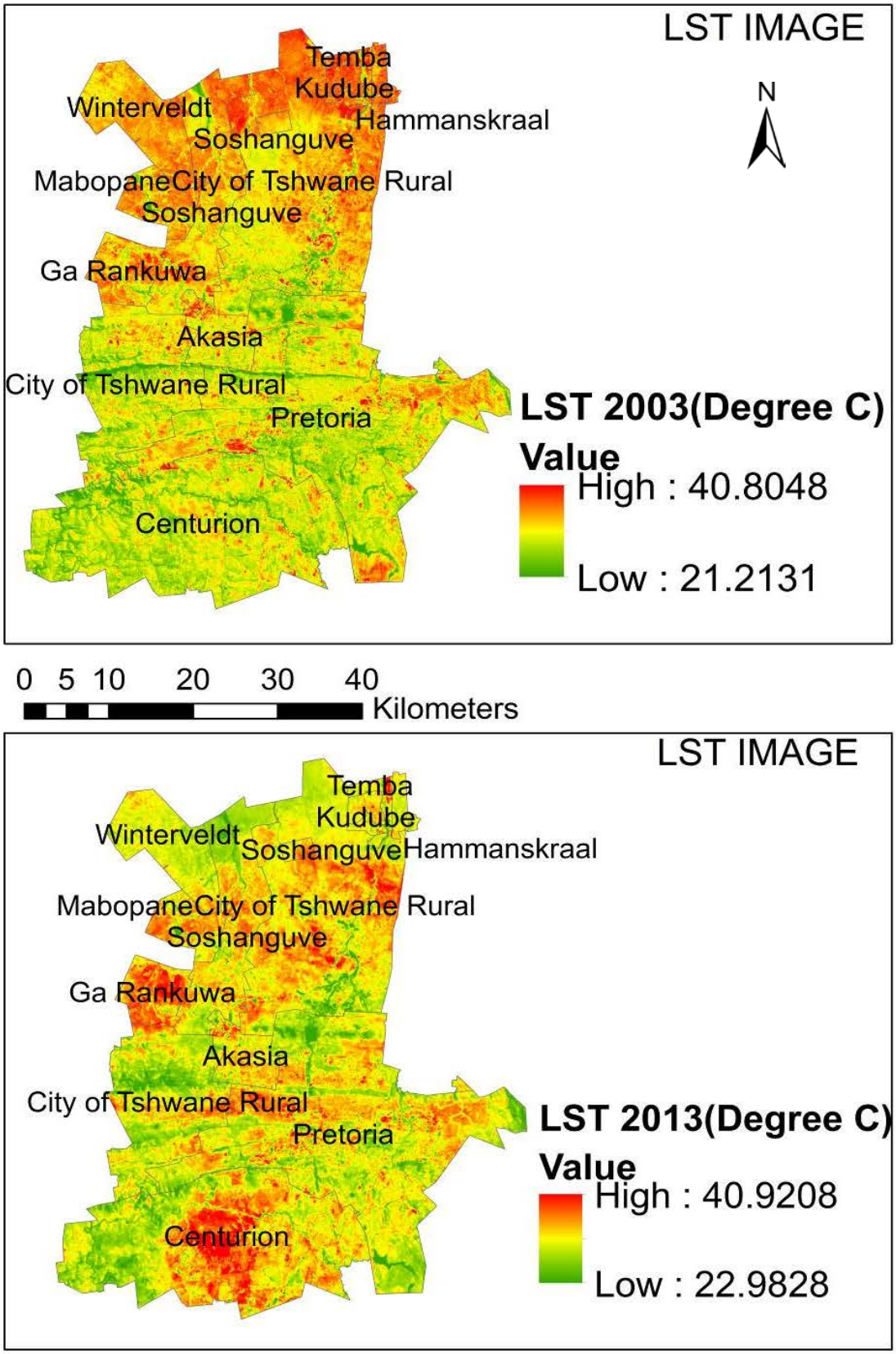

Figure 4.12: Land Surface Temperature map of the study area for Landsat 7 ETM+ 2003-Mar-31 and Landsat 8 2013-Nov-13.

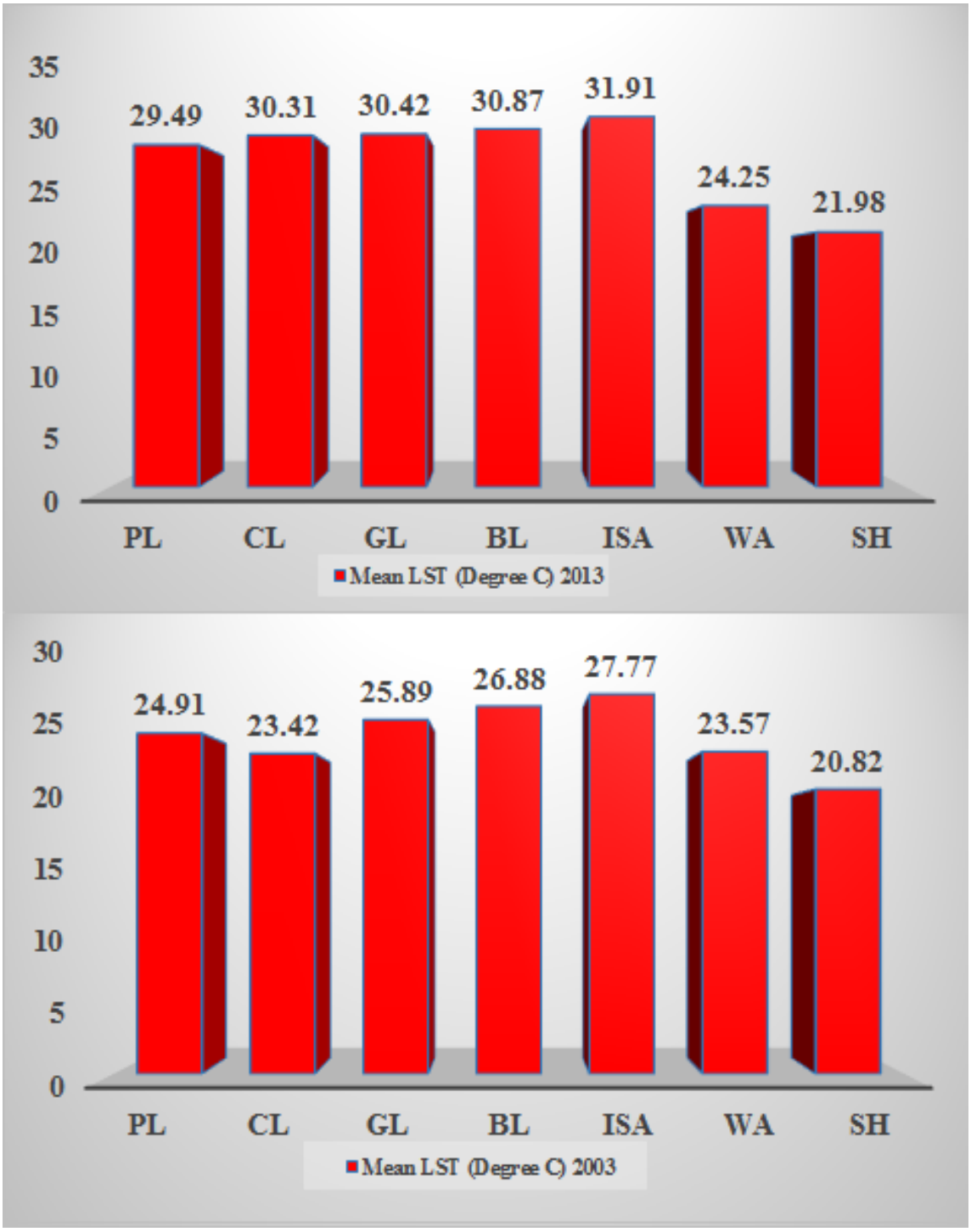

Figure 4.13: Histograms of mean LST for LULC classes for Landsat 7 ETM+ 2003-Mar-31 and Landsat 8 2013-Nov-13.

Figure 4.14: LST anomaly derived from the mean LST for LULC classes for Landsat 7 ETM+ 2003-Mar-31 and Landsat 8 2013-Nov-13.

5 CHAPTER FIVE: CONCLUSIONS AND FUTURE PROSPECTS

5.1 Conclusion

The main aim of this study is to investigate the relationship between ISA changes and LST using multispectral remote sensing data (Landsat) and other ancillary data (e.g., spectral signature from ASD, temperature data from weather stations) obtained across Tshwane metropolitan. Before the extraction of the various LULC from the Landsat images, ground observation was carried out with the use of analytical spectral device (ASD) and GPS. The acquired spectral signatures of some land cover types were used to aid image classification and validation thereof. Thereafter, the supervised classification using parametric and nonparametric classifiers was carried out to extract the seven LULC types within the study area. The moderate resolution Landsat 7 ETM+ and Landsat 8 LCDM indicated that LULC classes can be extracted using ML and RF algorithms. Pairwise comparison of error matrix by use of the kappa coefficient was then used to compare the error matrices. The goal of the comparison was to determine if the algorithms are significantly different or the same. For, Landsat 7 ETM + 2003-March-31 image, both ML and RF classifier produced an overall accuracy of 88.63% and 88.82% together with Kappa coefficient of 0.866 and 0.87 respectively. Also, Landsat 8 LCDM, 2013-November-13 image showed an overall accuracy of 80.13% and 82.03% and kappa coefficient of 0.76 and 0.79 respectively. The 2-sample Z-test was used to compare the two errox matrix generated from both images. At 5% significance level, the z-value estimated for the two-tailed comparisons for the two images is less than $Z_{\alpha/2}$ (i.e., z-value < 1.96) and p-value > 0.05. This implies that after applying the two classifiers on both Landsat images, there was little evidence against the Null hypothesis Ho: (K_1-K_2 = 0) i.e., the Ho is not rejected. A non – rejection of the Null hypothesis implies that both classifiers produced similar classification errors and either of the classifiers can be selected to classify Landsat 7 ETM+ and Landsat 8 LCDM.

Generally, the change pattern of the LULC classes observed in this study between the two years, revealed that there has been a high dynamic interchange of LULC that occurred (Table 4.7 and Table 4.8). Based on the result presented in Figure 4.10, it can be observed that the classifiers were capable of mapping the changes that occurred within the study area. Figure 4.10 illustrated an overall change of 66% (ML) and 73% (RF) in PL, 88% (ML) and 66% (RF) in CL and 87% (ML) and 79% (RF) for GL depending on the agricultural practises.

BL depicts an overall change of 30% (ML) and 26% (RF) while which can be attributed to lots of open lands or soil. Due to urban sprawl (i.e., newly or reconstructed tall buildings, cemented interlocking floors and roads within the central business district (CBD), commercial centres and residential areas),ISA shows an overall change of 4% (ML) and 32% (RF). WA also experiences change of 20% (ML) and 99% (RF) mainly due to seasonal variations or climate change within the ten years period. Shadow (SH) has changed by 70% (ML) and 81% (RF) due to increase in the tall building in the Central Business District (CBD).

Furthermore, the study showed that changes in plantation, grassland, bare land and ISA both in the central business district, CBD (e.g., Pretoria CBD) and outskirt area (e.g., Centurion, Mabopane, Gan Rankuwa, Soshanguve etc.) caused increase in their mean LST values. Areas occupied by agricultural or cultivated land had an increase in the mean LST due to the presence of open soil. Based on the results from this study, it could be deduced that persistent warm anomalies over the years could be associated to ISA increase in area which impact on surface energy exchange, micro to meso scale climate and other environmental processes.

5.2 Significance of the study

In recent years, Gauteng province has experienced tremendous increase both in population and land use or cover changes. This urban sprawl has resulted in temperature variation across the major municipalities within the province. Although several studies investigating the impact of ISA changes due to urbanization on land surface temperature using remote sensing data in different cities across the globe (e.g., Asia and America) have been reported in literature, few of these studies have been done in South Africa in spite of the availability of satellite imagery. This has been proved by a recent search for online scientific papers using various search engines like Google and Journal citations which showed that limited studies focused on cities in Africa.

The significance of study reported in this dissertation can be can be summaried as follows;

- Firstly the study presented information on the types of LULC classes (i.e., plantation, cultivated land, grassland, bareland, ISA, water and shadow) and their change pattern across Tshwane metropolitan between 2003 and 2013.

- From the result, ISA increase observed from the LULC change detection analysis was as a result of increase in buildings, new asphaltic roads and cemented interlocking floors. Most of the ISA increase were noticed in CBD , industrial areas and emerging residential areas.

- The mean LST results also show the distribution of UHI across the Tshwane Metropolis. Base on the ISA increase, the LST map presents the intensified urban heat island effect within the CBD, industrial and open land areas (e.g., bare soil, rocks, mines etc.). Place with dispersed UHI distribution or small scale UHI effects were residential and rural areas with fewer ISA.

- Decision makers can use the information presented in this study in various governmental and private sectors such as energy management, urban planning, environmental sustainability and other socio-economic applications.

5.3 Limitations

The research conducted involved field observations and various desktop analysis during which a number of shortcomings were noticed:

- Several spectral signatures could not be obtained during the field observation because many private farm lands or cultivated lands and mines were restricted areas and it would have taken months to sort out the necessary documentation to gain access into this premise. Hence, we could not develop a comprehensive spectral library that could have been used for land use classification.

- Similarly, only two satellite images were considered for the research.

- Few ground control points (GCPs) were taken.

- Surface temperature from few weather stations were used for accuracy assessment of the retrieved LST.

- Limited time was allocated to the use of the ASD spectroradiometer for the field observation.

5.4 Recommendations and future research

Some recommendations are highlighted below:

- Further research work towards achieving a better and accurate LULC classification result can be done by employing the use of multispectral sensors with high spectral and spatial resolution. This will minimize the problem of mixed pixel associated with the moderate resolution images (Landsat), thereby providing more potential for the extraction of detailed land use or cover information i.e.,offers an advantage of detecting and distinguishing land features that occupy a small portion on earth surfaces.

- Additional information can also be acquired by means of comprehensive field observations so as to address issues of mapping reliability of the various LULC classes. Direct measurement of thermal response and emissivity of different land cover types can also be of great advantage in understanding of UHI pattern and thermal properties of urban landscape.

- Also policy makers must focus on strategies to modify urban geometry, for example, use of vegetation as a replacement for unnecessary impervious surface area can help minimize UHI effects. Also, urban planners can improve air quality in urban landscapes by including vegetation (e.g. trees, grasses).

6 REFERENCES

ADEROJU, O. M., SAMAKINWA, E. K. & IBRAHIM, D. 2013. An Assessment of Urban Heat Island in Akure Using Geospatial Techniques. *Journal of Environmental Science, Toxicology and Food Technology,* 6**,** 24-34.

AL-GAADI, K. A., SAMDANI, M. S. & PATIL, V. C. 2011. Assessment of Temporal Land Cover Changes in Saudi Arabia Using Remotely Sensed Data. Middle-East *Journal of Scientific Research,* 9**,** 711-717.

ALIPOUR, T., SARAJIAN, M. R. & A., E. 2011. Land surface temperature estimation from thermal bands of Landsat Sensor, case Study: Alashtar City. *International Archives of the Photogrammetry, Remote sensing and Spatial Information Sciences,,* Vol.XXXVIII-4/C7.

ALVES, D. S. 2002. Space–time dynamics of deforestation in Brazilian Amazoˆ nia. *International Journal of Remote Sensing,* 23**,** 2903–2908.

AMIRI, R., WENG, Q., ALIMOHAMMADI, A. & ALAVIPANAH, S. K. 2009. The spatial–temporal dynamics of land surface temperatures in relation to fractional vegetation cover and Land use/cover in the Tabriz urban area, Iran. *Remote Sensing of Environment,* 113**,** 2606 – 2617.

ARMOUR, B., TANAKA, A., OHKURA, H. & SAITO, G. 1998. Radar interferometry for environmental change detection. *In:* ELVIDGE, R. S. L. A. C. D. (ed.) *Remote Sensing Change Detection: Environmental Monitoring Methods and Applications.* Chelsea, MI: Ann Arbor Press.

ARNOLD, J. C. L. & GIBBONS, C. J. 1996. Impervious surface coverage: the emergence of a key environmental indicator. *Journal of the American Planning Association,* 62**,,** 243–258.

ASIMAKOPOULOS, D. N., ASSIMAKOPOULOS, V. D., CHRISOMALLIDOU, N., KLITSIKAS, N., MANGOLD, D., MICHEL, P., SANTAMOURIS, M. & TSANGRASSOULIS, A. 2001. Energy and Climate in the Urban Built Environment,. *In:* SANTAMOURIS, M. (ed.). London: James and James Publication.

BAUER, M. E., LOEFFELHOLZ, B. & WILSON, B. Estimation, mapping and change analysis of impervious surface area by Landsat remote sensing. Proceedings Pecora, 16 Conference, ASPRS Annual Conference, 2005 Sioux Falls, SD, 23–27.

BAUER, M. E., LOFFELHOLZ, B. C. & WILSON, B. 2007. Estimating and mapping impervious surface area by regression analysis of Landsat imagery. *In:* WENG, Q. (ed.) *Remote Sensing of impervious surfaces.*

BERBEROGLU, S. & AKIN, A. 2009. Assessing different remote sensing techniques to detect land use/cover changes in the eastern Mediterranean. *International Journal of Applied Earth Observation and Geoinformation* 11**,** 46–53.

BINNS, J. A., MACONACHIE, R. A. & TANKO, A. I. 2003. Water, land and health in urban and peri-urban food production:The case of Kano, Nigeria. . *Land Degradation & Development,* 14**,** 431–444.

BOBRINSKAYA, M. 2012. *Remote Sensing for Analysis of Relationships between Land Cover and Land Surface Temperature in Ten Megacities.* Masters of Science Thesis in Geoinformatics, Royal Institute of Technology.

BOTTYÁN, Z. & UNGER, J. 2003. A multiple linear statistical model for estimating the mean maximum urban heat island. . *Theoretical and Applied Climatology,* 75**,** 233-243.

BRABEC, E., SCHULTE, S. & RICHARDS, P. L. 2002. Impervious surface and water quality: A review of current literature and its implications for watershed planning. . *Journal of Planning Literature,*16**,** 499–514.

BREIMAN, L. 1996. Bagging predictors. *Machine Learning,* 24**,** 123 - 140.

BREIMAN, L. 2001. Random Forests. *Machine Learning,* 45**,** 5-32.

BRIDGMAN, H., WARNER, R. & DODSON, J. 1995. Urban Biophysical Environments, Oxford, University Press.

BRUN, S. E. & BAND, L. E. 2000. Simulating runoff behavior in an urbanizing watershed. Computers, Environment and Urban Systems, 24, 5-22.

BRUNSELL 2006. Characterization of land-surface precipitation feedback regimes with remote sensing, . *Remote Sensing of Environment,* 100**,** 200-211.

CAPITAL PARK 2008. Rovos Rail.

CARLSON, T. N. & ARTHUR, S. T. 2000. The impact of land use–land cover changes due to urbanization on surface microclimate and hydrology: A satellite perspective. . *Global and Planetary Change,* 25**,** 49-65.

CARLSON, T. N. & RIPLEY, D. A. 1997. On the relation between NDVI, fractional vegetation cover, and leaf area index. *Remote Sensing of Environment,* 62**,** 241–252.

CASSMAN, K., WOOD, S., CHOO, P. S., DIXON, J., GASKELL, J., KHAN, S., LAL, R., KANBAR, N., PORTER, S. & THARME, R. 2005. Cultivated systems. *In:* SCHOLES, R., RASHID, H, ed. Millennium Ecosystem assessment: Working group on condition and trends,Washington D.C. Island Press.

CENDESE, A. & MONTI, P. 2003. Interaction between an inland urban heat island and a sea-breeze flow: A laboratory study. *Journal of Applied Meteorology*, 42**,** 1569–1583.

CHABAEVA, A. A., CIVCO, D. L. & PRISLOE, S. 2004. Development of a population density and land use based regression model to calculate the amount of imperviousness. ASPRS Annual Conference Proceedings, Denver, Colorado.

CHAN, J. C. W. & PAELINCKX, D. 2008. Evaluation of Random Forest and Adaboost tree-based ensemble classification and spectral band selection for ecotype mapping using airborne hyper spectral imagery. *Remote Sensing of Environment,* 112**,** 2999-3011.

CHANDER, G., COAN, M. J. & SCARAMUZZA, P. L. 2008. Evaluation and comparison of the IRS-P6 and the Landsat Sensors. *IEEE Transactions on Geoscience and Remote Sensing*, 46**,** 209−221.

CHANDER, G., MARKHAM, B. L. & H., D. L. 2009. Summary of current radiometric calibration coefficients for Landsat MSS, TM, ETM+, and EO-1 ALI sensors. *Remote Sensing of Environment* 113**,** 893-903.

CIVCO, D. L., CHABAEVA, A., ANGEL, A. & SHEPPARD, S. 2005. The urban growth management initiative: confronting the expected doubling of the size of cities in the developing countries in the next thirty years - methods and preliminary results,. *Geospatial Goes Global: From Your Neighborhood to the Whole Planet,* Baltimore, Maryland, USA.

CIVCO, D. L., HURD, J. D., ARNOLD, C. L. & PRISLOE, S. Characterization of suburban sprawl and forest fragmentation through remote sensing applications. Proceedings, Annual Conference of the American Society for Photogrametry and Remote Sensing (ASPRS), 2002 Washington, DC.

CONGALTON, R. G. 1991. A review of assessing the accuracy of classifications of remotely sensed data. Remote Sensing of Environment, 37, 35−46.

CONGALTON, R. G. & GREEN, K. 2009. *Assessing the accuracy of remote sensed data.*, London and New York, CRC Press.

COPPIN, P., JONKHEERE, I., NACKAERTS, K., MUYS, B. & LAMBIN, E. 2004. Digital change detection methods in ecosystem monitoring: A review. *International Journal of remote sensing,* 25**,** 1565–1596.

DASH, P., G¨OTTSCHE, F., OLESEN, F. & FISCHER, H. 2001. Retrieval of land surface temperature and emissivity from satellite data: physics, theoretical limitations and current methods. *Journal of the Indian Society of Remote Sensing,* 29**,** 23–30.

DASH, P., GOTTSCHE, F.-M., OLESEN, F.-S. & FISCHER, H. 2002. Land surface temperature and emissivity estimation from passive sensor data: Theory and practice-current trends. *International Journal of Remote Sensing,* 23**,** 2563–2594.

DE VOORDE, T. V., DE GENST, W. & CANTERS, F. 2007. Improving pixel-based VHR landcover classifications of urban areas with post-classification techniques. Photogrammetric Engineering and Remote Sensing, 73, 1017–1027.

DEER, P. J. 1995. Digital change detection techniques: civilian and military applications. Greenbelt, MD.

DENG, C. & WU, C. 2013. Examining the impacts of urban biophysical compositions on surface urban heat island: a spectral unmixing and thermal mixing approach. *Remote Sensing of Environment,* 131**,** 262–274.

DOMINGUEZ, A., KLEISSL, J., LUVALL, J. C. & RICKMAN, D. L. 2011. High resolution urban thermal sharpener (HUTS). *Remote Sensing of Environment,*, 115**,** 1772–1780.

DÖÖS, B. R. & SHAW, R. 1999. Can we predict the future food production? A sensitivity analysis. *Global Environmental Change,* 9**,** 261-283.

DOUSSET, B. & GOURMELON, F. 2003. Satellite multi-sensor data analysis of urban surface temperatures and land cover. Photogrammetry and Remote Sensing, 58,43–54

EL-KAWY, O. R. A., ROD, J. K., ISMAIL, H. A. & SULIMAN, A. S. 2011. Land use and land cover change detection in Western Nile Delta of Egypt using remote sensing data. Applied Geography, 31, 483 - 494.

ELVIDGE, C., TUTTLE , B., SUTTON, P., BAUGH, K., HOWARD, A., MILESI, C., BHADURI, B. & NEMANI, R. 2007. Global distribution and density of constructed impervious surfaces *Sensors,* 7 1962-1979.

ELVIDGE, C. D., BAUGH, K. E., KIHN, E. A., KROEHL, H. W., DAVIS, E. R. & DAVIS, C. W. 1997. Relation between satellites observed visible-near infrared emissions, population, economic activity and electric power consumption. . *International Journal of Remote Sensing,* 18**,** 1373-1379.

EMMANUEL, M. R. 2005. An urban Approach to climate - sensitive Design; strategies for the Tropic, London : Spon Press.

FAN, F., WENG, Q. & Y, W. 2007. Land use and land cover change in Guangzhou, China, from 1998 to 2003, based on Landsat TM/ETM+ imagery. *Sensors* 1323-1342.

FERREIRA, F., SEVENHUYSEN, P. & TREURNICH, J. 1999. Satellite earth observation to detect urban land use change. *In:* TOURISM, D. O. E. A. A. (ed.). Pretoria.

FOODY, G. & MATHUR, A. 2004. A relative evaluation of multiclass image classification by support vector machines. *IEEE Transactions on Geoscience and Remote Sensing,* 4**,** 1335-1343.

FOODY, G. M. 2010. Assessing the accuracy of land cover change with imperfect ground reference data. *Remote Sensing of Environment,* 114**,** 2271–2285.

FOODY, G. M., LUCAS, R. M., CURRAN, P. J. & HONZAK, M. 1997. Non-linear mixture modelling without end-members using an artificial neural network. *International Journal of Remote Sensing,* 18**,** 937–953.

FRANKE, J., ROBERTS, D. A., HALLIGAN, K. & MENZ, G. 2009. Hierarchical Multiple Endmember Spectral Mixture Analysis (MESMA) of hyperspectral imagery for urban environments. . *Remote Sensing of Environment,* 113**,** 1712–1723.

FRIEDL, M. A. 2002. Forward and inverse modeling of land surface energy balance using surface temperature measurements. *Remote Sensing of Environment,* 79**,** 344–354.

GEIGER, R. 1951. Microclimatology. Compendium of Meteorology,. Boston,: American society.

GIVONI, B. 1998. *Climate Considerations in Building and Urban Design,* Canada, John Wiley& Sons.

GOWARD, S. N., CRUICKSHANK, G. D. & HOPE, A. S. 1985. Observed relation between thermal emission and reflected spectral radiance of a complex vegetated landscape. *Remote Sensing of Environment,* 18**,** 137−146.

GRIFFITHS, P., HOSTERT, P., GRUEBNER, O. & VAN DER LINDEN, S. 2010. Mapping megacity growth with multi-sensor data. *Remote Sensing of Environment,*114**,** 426-439.

HAMMER, R. B., STEWART, S. I., WINKLER, R. L., RADELOFF, V. C. & VOSS, P. R. 2004. Characterizing dynamic spatial and temporal residential density patterns from 1940–1990 across the North Central United States. *Landscape and Urban Planning,,* 69**,** 183–199.

HANSEN, J., RUEDY, R., SATO, M. & LO, K. 2010. Global surface temperature change. *Reviews of Geophysics,* 48.

HARMON, C. F. 2011. *Automating Identification of Roads and Trails under canopy using Lidar*. MASTER OF SCIENCE IN SPACE SYSTEMS OPERATIONS and MASTER OF SCIENCE IN REMOTE SENSING INTELLIGENCE, University of North Carolina.

HEIDEN, U., ROESSNER, S., SEGL, K. & KAUFMANN, H. Analysis of spectral signatures of urban surfaces for their area-wide .identification using Hyperspectral HyMap data. Joint Workshop on Remote Sensing and Data Fusion in Urban Area, , 2001 Rome, Italy. IEEE/ISPRS, 173–177.

HEIDINGER, A. K., FOSTER, M. J., WALTHER, A. & ZHAO, X. T. 2014. The Pathfinder Atmospheres Extended (PATMOS-x) AVHRR climate data set. Bulletin of the American Meteorological Society, 95, 909–922.

HEROLD, M., D.A., R., M.E., G. & P.E., D. 2004. Spectrometry for urban area remote sensing-Development and analysis of a spectral library from 350 to 2400 nm. *Remote sensing of the Environment,* 91**,** 304–319.

HEROLD, M., LIU, X. H. & CLARKE, K. C. 2003. Spatial Metrics and Image Texture for Mapping Urban Land Use. *Photogrammetric Engineering & Remote Sensing,,* 69**,** 991–1001.

HIRATA, M., KOGAB, N., SHINJO, H. & GINTZIBURGER, G. 2001. Vegegtation classification by satatellite imaga processing in a dry areaof North - Eastern Syria. . *International Journal of Remote Sensing* 22**,** 507 - 516.

HODGSON, M. E., JENSEN, J. R., TULLIS, J. A., RIORDAN, K. D. & ARCHER, C. M. 2003. Synergistic use of Lidar and color aerial photography for mapping urban parcel imperviousness. Photogrammetric Engineering and Remote Sensing, 69, 973–980.

HU, X. & WENG, Q. 2009. Estimating impervious surfaces from medium spatial resolution imagery using the self-organizing map and multi-layer perceptron neural networks. Remote Sensing of Environment,113, 2089–2102.

IFATIMEHIN, O. O. & ADEYEMI, S. 2008. A satellite remote sensing based land surface temperature retreival from Landsat TM data. . Ethiopian Journal of Environmental Studies and Management 1, 63–70.

IFATIMEHIN, O. O., FANAN, U. & MAGAJI, J. Y. 2009. An evaluation of the effect of land use/cover change on the surface temperature of Lokoja town, Nigeria. . African Journal of Environmental Science and Technology, 3, 086-090.

IMHOFF, M. L., ZHANG, P., WOLFE, R. E. & BOUNOUA, L. 2010. Remote sensing of the urban heat island effect across biomes in the continental USA. *Remote Sensing of Environment* 114**,** 504-513.

IPCC 2001. Climate Change 2001: The Scientific Basis. *In:* AL., J. T. H. E. (ed.) *Contribution of Working Group I to the Third Assessment Report of the Intergovernmental Panel on Climate Change,*. New York.

JACQUIN, A., MISAKOVA, L. & GAY, M. 2008. A hybrid object-based classification approach for mapping urban sprawl in periurban environment. Landscape and Urban Planning, 84, 152–165.

JENNINGS, D. & JARNAGIN, S. T. 2000. Impervious surfaces and stream flow discharge: a historical remote sensing perspective in a northern Virginia sub watershed. ASPRS Annual Conference. Washington, D.C. USA: ASPRS.

JENSEN, J. 2005. *Introduction to digital image processing,* New York, Prentice Hall.

JENSEN, J. R. 2007. *Remorte sensing of the environment: an earth resource perspective – second edition.,* Upper Saddle River, USA, Person Prentice Hall,.

JEONG, J. J. U. 2012. Higher temperature effects of impervious surface due to urbanization in South Berkeley, California. *Impervious surface and Temperature, spring,* 1-15.

JIANYA, G., HAIGANG, S., GUORUI, M. & QIMING, Z. 2008. A review of multi-temporal remote sensing data change detection algorithms, The International Archives of the Photogrammetry. *Remote Sensing* 37**,** 757-762.

JIME´NEZ-MUNˇ OZ, J. C. & SOBRINO, J. A. 2003. A generalized single channel method for retrieving land surface temperature from remote sensing data. *Journal of Geophysical Research,* 108.

JIMÉNEZ-MUÑOZ, J. C., CRISTÓBAL, J., SOBRINO, J. A., SÒRIA, G., NINYEROLA, M. & PONS, X. 2009. Revision of the Single-Channel Algorithm for Land Surface Temperature Retrieval from Landsat Thermal-Infrared Data. . *IEEE transactions on Geoscience and remote sensing,* 47**,** 339 – 348.

KALNAY, E. & CAI, M. 2003. Impact of urbanization and land-use change on climate. *Letters to Nature* 423, 528-531.

KAVZOGLU, T. & COLKESEN, I. 2009. A kernel functions analysis for support vector machines for land cover classification. . *International Journal of Applied Earth Observation and Geoinformation,*11**,** 352-359.

KIMURA, H. & YAMAGUCHI, Y. 2000. Detection of landslide areas using satellite radar interferometry. *Photogrammetric Engineering and Remote Sensing,*66**,** 337–343.

LAMBIN, E. F. & GEIST, H. J. 2008. *Land use and land cover change: Local process and Global impacts.* , Berlin, Springer.

LAMBIN, E. F., GEIST, H. J. & LEPERS, E. 2003. Dynamics of land use and cover change in tropical and subtropical regions. *Annual Review of Environment and Resources.*

LANDSBERG, E. H. 1981. *The Urban Climate,* Maryland, Academic Press.

LEE, S. & LATHROP, R. G. 2006. Sub pixel analysis of Landsat 7 ETM+ using Self-Organizing Map (SOM) neural networks for urban land cover characterization. *IEEE Transactions on Geoscience and Remote Sensing,* 44**,** 1642–1654.

LEVERMAN, J. E. 2013. Assessing the impact of extreme rainfall on land cover changes in New Caledonia using remote sensing. University of Southampton.

LEVIN, N. (ed.) 2012. Fundamentals of Remote Sensing, Tel Aviv University, Israel: Remote Sensing Laboratory, Geography Department,.

LILLESAND, T. M. & KIEFER, R. W. 1999. Remote Sensing and Image Interpretation, John Wiley & Sons, Inc.

LILLESAND, T. M., KIEFER, R. W. & CHIPMAN, J. W. 2004. Remote sensing and image interpretation New York: John Wiley and Sons.

LILLESAND, T. M., KIEFER, R. W. & CHIPMAN, J. W. 2008. Remote sensing and image interpretation, New York, John Wiley and Sons.

LIU, Z., HUANG, F., LI, L. & WAN, E. 2002. Dynamic monitoring and damage evaluation of flood in north-west Jilin with remote sensing. *International Journal of Remote Sensing,* 23**,** 3669–3679.

LO, C. P., QUATTROCHI, D. A. & LUVALL, J. C. 1997. Application of high resolution thermal infrared remote sensing and GIS to assess the urban heat island effect,. *International Journal of Remote Sensing,* 18**,** 287–304.

LOHANI, V., KIBLER, D. F. & CHANAT, J. 2002. Constructing a problem solving environment tool for hydrologic assessment of land use change. *Journal of the American Water Resources Association,* 38**,** 439–452.

LOOSVELT, L., PETERS, J., SKRIVER, H., LIEVENS, H., VAN COILLIE, F., DE BAETS, B. & VERHOEST, N. E. C. 2012. Random Forests as a tool for estimating uncertainty at pixel-level in SAR image classification. *International Journal of Applied Earth Observation and Geoinformation,* 19, 173-184.

LU, D., MAUSEL, P., BRONDÍZIO, E. & MORANAC, E. 2004. Change detection techniques. *International Journal of Remote Sensing***,** 2365-2401.

LU, D., MORAN, E., HETRICK, S. & LI, G. 2011. Landuse and Land cover change detection. *In:* WENG, Q. E. T. F. (ed.) *Advances in Environmental Remote Sensing.* . Indiana University.

LU, D., TIAN, H., ZHOU, G. & GE, H. 2008. Regional mapping of human settlements in South-Eastern China with multi-sensor remotely sensed data. *Remote Sensing of Environment,* 112**,** 3668–3679.

LU, D. & WENG, Q. 2004. Spectral mixture analysis of the urban landscape in Indianapolis with Landsat ETM+ imagery. Photogrammetric Engineering and Remote Sensing, 70, 1053–1062.

LU, D. & WENG, Q. 2006. Use of impervious surface in urban land use classification. Remote Sensing of Environment, 102, 146–160.

LU, D. & WENG, Q. 2007. A survey of image classification methods and techniques for improving classification performance. *International Journal of Remote Sensing,* 28**,** 823-870.

LU, D. & WENG, Q. 2009. Extraction of urban impervious surfaces from IKONOS imagery. *International Journal of Remote Sensing,* 30**,** 1297–1311.

LUNETTA, R. S., KNIGHT, J. F., EDIRIWICKREMA, J., LYON, J. G. & WORTHY, L. D. 2006. Land cover change detection using multi temporal MODIS NDVI data. . *Remote sensing of environment,* 105**,** 142 – 154.

MAIMAITIYIMING, M., GHULAM, A., TIYIP, T., PLA, F., LATORRE-CARMONA, P., HALIK, Ü., SAWUT, M. & CAETANO, M. 2014. Effects of green space spatial pattern on land surface temperature: Implications for sustainable urban planning and climate change adaptation. *ISPRS Journal of Photogrammetry and Remote Sensing,* 89**,** 59-66.

MALLICK, J., KANT, Y. & BHARATH, B. D. 2008. Estimation of Land surface temperature over Delhi using Landsat 7 ETM+. *Journal of Indian Geophysical Union,* 12**,** 131-140.

MERTENS , B. & LAMBIN, E. F. 2000. Land-cover-change trajectories in southern cameroon. Annals of the Association of American Geographers, 90, 467–494.

MONTGOMERY, M. R. & HEWETT, P. C. 2005. Urban health in developing countries: Household and neighborhood effects. Demography, 42, 397- 425.

MUZEIN, B. S. 2006. Remote Sensing and GIS for Landcover/Landuse Change Detection and Analysis in the Semi-Natural Ecosystem and Agriculture Landscapes of the Central Ethiopian Rift Valley., A PhD Thesis Submitted to Technische Universität Dresden.

NASARUDIN, N. E. M. & SHAFRI, H. Z. M. 2011. Development and utilization of urban spectral library for remote sensing of urban environment. *Journal of Urban and Environmental Engineering,* 5**,** 44-56.

NDYAMBOTI, K. S. 2013. *Land cover classification in a heterogeneous environment: testing the performance of multispectral remote sensing data and the random forest ensemble algorithm.* University of KwaZulu-Natal.

NOIN, D. 1970. *La Population Rurale du Maroc,,* Paris, France., Presses Universitaires de France.

ODINDI, J., MHANGARA, P. & KAKEMBO, V. 2012. Remote sensing land-cover change in Port Elizabeth during South Africa's democratic transition. *South African Journal of Science,* 108**,** 1-7.

OKE, T. R. 1981. Canyon Geometry and the Nocturnal Urban Heat Island:. *International Journal of Climatology,* 1**,** 237-254.

OKE, T. R. 1982. The Energetic Basis of the Urban Heat Island. *Quarterly Journal of the Royal Meteorological Society,* 108**,** 1-24.

OKE, T. R. 1987. *Boundary Layer Climates,* New York, , Methuen and Co. Ltd.

OKE, T. R. & EMERY, W. J. 1989. Satellite-derived Urban Heat Islands from Three Coastal Cities and the Utilization of Such Data in Urban Climatology. *International Journal of Remote Sensing,* 10**,** 1699-1720.

OKE, T. R., SPRONKEN-SMITH, R. A., JAUREGUI, E. & GRIMMOND, C. S. B. 1999. The energy balance of central Mexico City during the dry season,. *Atmospheric Environment,* 33**,** 3919–3930.

OKEKE, F. I. Mapping Impervious Surface Changes in Watersheds in Part of South Eastern Region of Nigeria Using Landsat Data. 5th FIG Regional Conference on Promoting Land Administration and Good Governance, 2006.

PAOLA, J. D. & SCHOWENGERDT, R. A. 1995. A review and analysis of back propagation neural networks for classification of remotely sensed multispectral imagery. *International Journal of Remote Sensing,* 16**,** 3033–3058.

PARECE, T. E. & CAMPBELL, J. B. 2013. Comparing Urban Impervious Surface Identification Using Landsat and High Resolution Aerial Photography. *Remote Sensing of Environment,* 5**,** 4942-4960.

PETERS, A. J., WALTER-SHEA, E. A., LEI, J., VINA, A., HAYES, M. & SVOBODA, M. D. 2002. Drought monitoring with NDVI-based standardized vegetation index. *Photogrammetric Engineering and Remote Sensing,* 68**,** 71–76.

PETROPOULOS, G. P., KALAITZIDIS, C. & PRASAD, V. K. 2012. Support vector machines and object-based classification for obtaining land-use/cover cartography from Hyperion hyper spectral imagery. *Computers & Geosciences,*, 41**,** 99-107.

PHINN, S., STANFORD, M., SCARTH, P., MURRAY, A. T. & SHYY, P. T. 2002. Monitoring the composition of urban environments based on the vegetation-impervious surface–soil (VIS) model by subpixel analysis techniques. *International Journal of Remote Sensing,* 23**,** 4131–4153.

PINHEIRO, A. C. T., MAHONEY, R. PRIVETTE, J.L. AND TUCKER, C.J. 2006. Development of a daily long term record of NOAA-14 AVHRR land surface temperature over Africa. *Remote Sensing of Environment,* 103**,** 153–164.

POWELL, R. L., ROBERTS, D. A., DENNISON, P. E. & HESS, L. L. 2007. Sub-pixel mapping of urban land cover using multiple end member spectral mixture analysis: Manaus, Brazil. *Remote Sensing of Environment,* 106**,** 253–267.

POWELL, S. L., COHEN, W. B., YANG, Z., PIERCE, J. D. & ALBERTI, M. 2008. Quantification of impervious surface in the Snohomish Water Resources Inventory Area of Western Washington from 1972–2006. *Remote Sensing of Environment,* 112**,** 1895–1908.

QIN, Z., KARNIELI, A. & BERLINER, P. 2001. A mono-algorithm for retrieving land surface temperature from Landsat TM data and its application to the Israel–Egypt border region. *International Journal of Remote Sensing,* 22.

QUATTROCHI, D. A., LUVALL, J. C., RICKMAN, D. L., ESTES, J. M. G., C.A., L., SAHASHI, K., HIEDA, T. & YAMASHITA, E. 2004. Nitrogen-Oxide Layer over the Urban Heat Island in Okayama City. *Atmospheric Environment,* 30**,** 531-535.

RADELOFF, V. C., HAMMER, R. B. & STEWART, S. I. 2005. Rural and suburban sprawl in the US Midwest from 1940 to 2000 and its relation to forest fragmentation. Conservation biology, 19, 793–805.

RAJASEKAR, U. & WENG, Q. 2009. Application of association rule mining for exploring the relationship between urban land surface temperature and biophysical/social parameters. . Photogrammetric Engineering and Remote Sensing, 75, 385–396.

RAMOELO, A. 2007. An innovative method to map land cover changes at a country level utilising hyper-temporal satellite images. A case study of Portugal. Master of Science (Msc), University of Southampton (UK) Lund University (Sweden) University of Warsaw (Poland) International Institute for Geo-Information Science and Earth Observation (ITC) (The Netherlands).

RAO, P. K. 1972. Remote sensing of urban "heat islands" from an environmental satellite, . Bulletin of the American Meteorological Society, 53, 647–648.

RENEE, G., DALE, A. & QUATTROCHI, J. C. L. 2006. A multi-scale approach to urban thermal analysis, . *Remote Sensing of Environment,* 104**,** 123–132.

RIDD, M. K. 1995. Exploring a V-I-S (vegetation-impervious surface-soil) model for urban ecosystem analysis through remote sensing: comparative anatomy for cities. *International Journal of Remote Sensing,* 16**,** 2165-2185.

ROBERT, D. A. & HEROLD, M. 2004. Image spectrometry of urban materials. *Remote Sensing of Environment,* 121**,** 93-107.

ROBERTS, D. A., BATISTA, G. T., PEREIRA, J. L. G., WALLER, E. K. & NELSON, B. W. 1998. Change identification using multitemporal spectral mixture analysis: Applications in eastern Amazônia. *In:* R. S. LUNETTA, C. D. E. (ed.) *remote sensing change detection: Environmental monitoring methods and applications.* Ann Arbor, MI: Ann Arbor Press.

RODRIGUEZ-GALIANO, V. F., GHIMIRE, B., ROGAN, J., CHICA-OLMO, M. & RIGOL-SANCHEZ , J. P. 2012. An assessment of the effectiveness of a random forest classifier for land-cover classification. *Journal of Photogrammetry and Remote Sensing* 67**,** 93–104.

ROTH, M. Effects of Cities on Local Climates. Proceedings of Workshop of IGES/APN Mega-City Project, 2002 Kitakyushu Japan.

ROY, D., BORAK, J., DEVADIGA, S., WOLFE, R., ZHENG, M. & DESCLOITRES, J. 2002. The MODIS land product quality assessment approach. . *Remote Sensing of Environment,* 83**,** 62−76.

SAITOH, T. S., SHIMADA, T. & HOSHI, H. 1996. Modeling and simulation of the Tokyo urban heat island. *Atmospheric Environment,* 30**,** 3431–3442.

SANDHAM, L. A. & ZIETSMAN, H. L. 1997. Surface temperature measurement from space: A case study in the South Western Cape of South Africa,. *South African Journal for Enology and Viticulture,* 18**,** 25-30.

SAWS 2013. Climate data for Pretoria. South Africa: South African Weather Station.

SCHMID, H. P. & OKE, T. R. 1990. A model to estimate the source area contributing to turbulent exchange in the surface layer over Patchy Terrain. *Quarterly Journal of the Royal Meteorological Society,* 116**,** 965–988.

SETO, K. C., WOODCOCK, C. E., SONG, C., HUANG, X., LU, J. & KAUFMANN, R. K. 2002. Monitoring land-use change in the Pearl River Delta using Landsat TM. *International Journal of Remote Sensing,* 23**,** 1985–2004.

SHAHMOHAMADI, P., CHE-ANI, A. I., RAMLY, A., MAULUD, K. N. A. & M.F.I., M.-N. 2010. Reducing urban heat island effects: A systematic review to achieve energy consumption balance. *International Journal of Physical Sciences* 5**,** 626-636. .

SINGH, A. 1989. Digital change detection techniques using remotely-sensed data. *International Journal of Remote Sensing,* 10**,** 989-1003.

SINGH, S., SHARMA, K. D., SINGH, N. & BOHRA, D. N. 1990. Temporal change detection in uplands and gullied areas through satellite remote-sensing. *Annals of Arid Zone,,* 29**,** 171–177.

SLONECKER, E. T., JENNINGS, D. B. & GAROFALO, D. 2001. Remote sensing of impervious surfaces:A review. . *Remote Sensing Reviews,* 20**,** 227−255.

STATISTICSSOUTHAFRICA 2011. South African National Census of 2011- Main Place, "Pretoria". South Africa: Statistics South Africa.

STREUTKER, D. R. 2003. Satellite-measured growth of the urban heat island of Houston, Texas. *Remote Sensing of Environment,* 85,282–289.

SUN, Y. 2008. Term Paper –Retrieval and Application of Land Surface Temperature. Texas 78712, USA: Department of Geological Sciences, University of Texas.

SUTTON, P. C. 2003. A scale-adjusted measure of “Urban Sprawl” using nighttime satellite imagery. Remote Sensing of Environment, 86, 353–369.

TAHA, H. 1997. Urban Climates and Heat Islands: Albedo, Evapotranspiration and Anthropogenic Heat, Energy Buildings. Energy and Buildings, 25, 99-103.

TAYLOR, J. C., BREWER, T. R. & BIRD, A. C. 2000. Monitoring landscape change in the national parks of England and Wales using aerial photo interpretation and GIS. *International Journal of Remote Sensing,* 21**,** 2737–2752.

THOME, K. J., HELDER, D. L., AARON, D. A. & DEWALD, J. 2004. Landsat 5 TM and Landsat-7 ETM+ absolute radiometric calibration using reflectance based method. *IEEE Transactions on Geoscience and Remote Sensing,* 42**,** 2777−2785.

TOMLINSON, C. J., CHAPMAN, L., THORNES, J. E. & BAKER, C. J. 2011. The urban heat island in spatial heat health risk assessment strategies: a case study for Birmingham, UK. *International Journal of Health Geographics,* 10**,** 10-42.

TONG, H., WALTON, A., SANG, J. & CHAN, J. C. L. 2005. Numerical simulation of the urban boundary layer over the complex terrain of Hong Kong, . *Atmospheric Environment,* 39**,** 3549–3563.

TSELA, P. L., WESSELS, K., BOTAI, J., ARCHIBALD, S., SWANEPOEL , D., STEENKAMP, K. & FROST, P. 2014. Validation of the Two Standard MODIS Satellite Burned-Area Products and an Empirically-Derived Merged Product in South Africa. *Remote Sensing***,** 1275-1293.

TURNER, B. L. 2006. Land change as a forcing function in global environmental change. London, , Greenwood press, .

U.S. GEOLOGICAL SURVEY 2013. Landsat 8 Landsat Data Continuity Mission. *Fact Sheet 2013–3060.*

UN 2008. World urbanization prospects: . *The 2007 revision.* New York.

VANCUTSEM, C., CECCATO, P. & DINKU, T. 2010. Evaluation of MODIS land surface temperature data to estimate air temperature in different ecosystems over Africa. *Remote Sensing of Environment,* 114**,** 449–465.

VOOGT, J. A. & OKE, T. R. 2003. Thermal remote sensing of urban climates. *Remote Sensing of Environment,* 86**,** 370-384.

WALTON, J. T. 2008. Sub pixel urban land cover estimation: comparing cubist, random forests, and support vector regression. . *Photogrammetric Engineering & Remote Sensing,,* 74**,** 1213-1222.

WATTS, J. D. & LAWRENCE, R. L. 2008. Merging random forest classification with an object-oriented approach for analysis of agricultural lands. *The International Archives*

of the Photogrammetry, Remote Sensing and Spatial Information Sciences, 37**,** 579-582.

WATTS, J. D., LAWRENCE, R. L., MILLER, P. R. & MONTAGNE, C. 2009. Monitoring of cropland practices for carbon sequestration purposes in north central Montana by Landsat remote sensing. *Remote Sensing of Environment,* 113**,** 1843-1852.

WEATHERNETWORK 2012. Climate Statistics for Pretoria, . *Forecast and report.* South Africa.

WEDDERBURN – BISHOP, G., WALLS, J., SENERATH, U.G. AND STEWART, A.J. 2002. A methodology for mapping change in woody land cover in Queensland from 1999 to 2001 using Landsat ETM +. . Proceedings of the 11th Australasian Remote Sensing and Photogrammetry conference, Brisbane, Australia. 2 – 6.

WENG, Q. 2007. *Remote sensing of impervious surfaces,* Boca Raton, FL, CRC Press.

WENG, Q. 2009. Thermal infrared remote sensing for urban climate and environmental studies:Methods, applications, and trends. ISPRS *Journal of Photogrammetry and Remote Sensing,* 64, 335-344.

WENG, Q. 2012. Remote sensing of impervious surface in the urban area: Requirement, methods and trends. *Remote sensing of the Environment,* 117, 34-49.

WENG, Q., HU, X. & LIU, H. 2009. Estimating impervious surfaces using linear spectral mixture analysis with multi-temporal ASTER images. *International Journal of Remote Sensing,* 30**,** 4807–4830.

WENG, Q. & LU, D. 2009. Landscape as a continuum: An examination of the urban landscape structures and dynamics of Indianapolis city, 1991–2000. . *International Journal of Remote Sensing,* 30**,** 2547–2577.

WENG, Q., LU, D. & SCHUBRING, J. 2004. Estimation of land surface temperature–vegetation abundance relationship for urban heat island studies. *Remote Sensing of Environment,* 89**,** 467–483.

WHO 2004. Heat waves: Risks and Responses. *Health and Global Environmental Change Geneva.* London School of Hygiene and Tropical Medicine and WHO/Europe.

WU, C. 2004. Normalized spectral mixture analysis for monitoring urban composition using ETM+ imagery. . *Remote Sensing of Environment,* 93**,** 480–492.

XIAN, G. 2007 Mapping impervious surfaces using classification and regression tree algorithm. Remote Sensing of Impervious Surfaces .

XIAO, R., WENG, Q., OUYANG, Z., LI, W., SCHIENKE, E. W. & ZHANG, W. 2008. Land surface temperature variation and major factors in Beijing, China. *Photogrammetric Engineering & Remote Sensing* 74**,** 451- 461.

XU 2006. Modification of normalised difference water index (NDWI) to enhance open water features in remotely sensed imagery. *International Journal of Remote Sensing*, 27, 3025–3033.

YAN, H., ZHANG, J., HOU, Y. & Y., H. 2009. Estimation of air temperature from MODIS data in east China. *International Journal of Remote Sensing*, 30, 6261–6275.

YANG, F., MATSUSHITA, B. & FUKUSHIMA, T. 2010. A pre-screened and normalized multiple endmember spectral mixture analysis for mapping impervious surface area in Lake Kasumigaura Basin, Japan. *ISPRS Journal of Photogrammetry and Remote Sensing*, 65**,** 479–490.

YANG, L., HUANG, C., HOMER, C. G., WYLIE, B. K. & COAN, M. J. 2003. An approach for mapping large-scale impervious surfaces: Synergistic use of Landsat 7 ETM+ and high spatial resolution imagery. *Canadian Journal of Remote Sensing,* 29**,** 230–240.

YOOL, S. R., MAKAIO, M. J. & J.M., W. 1997. Techniques for computer-assisted mapping of rangeland change. *Journal of Range Management Archives*, 50, 307.

YU, Y., J.L., P. & PINHEIRO, A. C. 2008. Evaluation of split-window land surface temperature algorithms for generating climate data records. *IEEE Transactions on Geoscience and Remote Sensing*, 46, 179–192.

YUAN, F. & BAUER, M. E. 2007. Comparison of impervious surface area and normalized difference vegetation index as indicators of surface urban heat island effects in Landsat imagery. *Remote Sensing of Environment,*, 106**,** 375–386.

YUAN, F., SAWAYA, K. E., LOEFFELHOLZ, B. C. & BAUER, M. E. 2005. Land cover classification and change analysis of the Twin Cities (Minnesota) metropolitan area by multitemporal Landsat Remote sensing. *Remote Sensing of Environment,* 98**,** 317–328.

YUAN, F., WU, C. & BAUER, M. E. 2008. Comparison of spectral analysis techniques for impervious surface estimation using Landsat imagery. *Photogrammetric Engineering and Remote Sensing*, 74, 1045–1055.

ZHA, Y., NI, S. & YANG, S. 2003. An Effective Approach to Automatically Extract Urban Land-use from TM Imagery. *Journal of Remote Sensing*, 7, 37-40.

ZHANG, Y., ODEH, O. A. & HAN, C. 2009. Bi-temporal characterization of land surface temperature in relation to impervious surface area, NDVI and NDBI, using a sub-pixel image analysis. *International Journal of Remote Sensing,* 11**,** 256-264.

Apppendix 1: Land cover types in South Africa according to land-cover legend 2012 release Geoterraimage (GTI) land-cover data set.

1	Buildings	Permanent structures varying in height, but generally more than two storeys high.
2	Building (Schools)	Permanent structures associated with a pre-tertiary education facilities, and associated buildings within the school grounds.
3	Building (Campuses)	Permanent structures associated with a tertiary education campuses and associated infrastructure
4	Sport Stadiums (Buildings)	Large structures comprising both central sports field and surrounding viewing stand / seats used primarily or the hosting of large sporting events.
5	School Grounds	Open areas within the school boundary. Includes school sports fields and other associated open spaces.
6	Sports & Recreation	Areas, structures and spaces used exclusively for sport and recreational activities primarily outside of school boundaries, but excludes formal or informal urban parks.
7	Golf Courses	Irrigated planted grassland associated with golf courses.
8	Industrial	Medium-large buildings and structures associated with industrial activities such as manufacturing, production and storage.
9	Heavy Industrial	Large-extremely large buildings and facilities for large scale manufacturing and processing, includes all related and associated structures.
10	Residential - Cluster	Townhouses, clusters and multi-storey buildings and other high density residential dwellings.
11	Residential	Typical suburban residential dwellings and formal (planned) housing areas.
12	Township Formal	Some level of planning and formality exists in the settlement patterns of these areas of permanent and /or semi-permanent dwelling structures.
13	Township Informal	Areas where the majority of the housing structures is informal and the settlement patterns are often

		erratic / of an unplanned appearance.
14	Small Holdings	Areas of low residential concentrations in the outskirts of towns and cities, other activities in these areas include small-scale agriculture and industrial.
15	Village	Low density residential areas usually associated with cultural settlement patterns.
16	Roads	National, regional, and major roads, streets and secondary roads are included in urbanized areas. Note, that the road network should not be considered a definitive indication of all communication networks, since content is influenced by image detail.
17	Rail	Main surface rail networks.
18	Thicket, Bushland, Bush-Clumps	Bush and shrub dominated areas in a natural state, with 40% - 100% canopy closure (i.e. “bushveld”). This is a single cover of canopy density conditions from open to closed.
20	Tree (Non-Natural / Planted)	Tree dominated areas with 75 – 100 % canopy closure, composed primarily of non-indigenous species, in the form of planted forest plantations, woodlots, linear windbreaks and orchards.
21	Shrubland & Low Fynbos	Areas of near pristine, undisturbed low woody shrub cover, typically characteristic of low fynbos in the Cape regions.
22	Planted & Natural Grassland	Planted and natural grass dominated areas with little or no tree, bush or shrub cover.
23	Wetlands	Vegetated wetlands that may or may not be flooded (at the time of source image acquisition). Includes all wetland types in one category, i.e. pans and vleis.
24	Wetlands, Mangrove	Mangrove wetlands.
25	Degraded Natural Vegetation	Disturbed or transformed natural vegetation, represented by a reduction in local canopy cover (as visible on the imagery as a result of conditions at the time of image acquisition).
26	Cultivated, Commercial, Irrigated	Commercial, medium-large scale irrigated cultivation of annual crops.

27	Cultivated, Commercial, Dryland / rain-fed	Commercial, medium-large scale dryland cultivation of annual crops.
28	Cultivated, Commercial, Sugarcane	Commercial, large scale sugarcane cultivation, including both irrigated and dryland crops.
29	Mines & Quarries	Combination of extraction pits, waste and storage dumps associated with mining. Includes quarries.
30	Open	Open areas with little or no vegetation cover. Parking lots, bare sand, etc.
31	Water	Areas of permanent or near permanent water (natural or man-made), flowing or static. Includes rivers, dams, pans and lakes.
32	Sea	Very large body of coastal water.
33	Bare Rock & Soil (Natural Surfaces)	Naturally occurring, non-vegetated rock, sand and soil exposures.
34	New Development	Areas where the vegetation has been removed preparation of new urban developments.